VARIABLE SPEED PUMPED HYDRO BASED ON MODULAR MULTILEVEL CONVERTERS: MODELING, CONTROL AND ANALYSIS OF PUMPING-MODE OPERATION

Matheus Soares da Silva

Dissertação de Mestrado apresentada ao Programa de Pós-graduação em Engenharia Elétrica, COPPE, da Universidade Federal do Rio de Janeiro, como parte dos requisitos necessários à obtenção do título de Mestre em Engenharia Elétrica.

Orientador: Edson Hirokazu Watanabe

Rio de Janeiro
Dezembro de 2020

VARIABLE SPEED PUMPED HYDRO BASED ON MODULAR MULTILEVEL CONVERTERS: MODELING, CONTROL AND ANALYSIS OF PUMPING-MODE OPERATION

Matheus Soares da Silva

DISSERTAÇÃO SUBMETIDA AO CORPO DOCENTE DO INSTITUTO ALBERTO LUIZ COIMBRA DE PÓS-GRADUAÇÃO E PESQUISA DE ENGENHARIA DA UNIVERSIDADE FEDERAL DO RIO DE JANEIRO COMO PARTE DOS REQUISITOS NECESSÁRIOS PARA A OBTENÇÃO DO GRAU DE MESTRE EM CIÊNCIAS EM ENGENHARIA ELÉTRICA.

Orientador: Edson Hirokazu Watanabe

Aprovada por: Prof. Edson Hirokazu Watanabe
Prof. Luis Guilherme Barbosa Rolim
Prof. Pedro Gomes Barbosa

RIO DE JANEIRO, RJ – BRASIL
DEZEMBRO DE 2020

Silva, Matheus Soares da

Variable Speed Pumped Hydro based on Modular Multilevel Converters: Modeling, Control and Analysis of Pumping-Mode Operation/Matheus Soares da Silva. – Rio de Janeiro: UFRJ/COPPE, 2020.

XVII, 139 p.: il.; 29, 7cm.

Orientador: Edson Hirokazu Watanabe

Dissertação (mestrado) – UFRJ/COPPE/Programa de Engenharia Elétrica, 2020.

Referências Bibliográficas: p. 122 – 136.

1. Pumped Hydro Storage. 2. Modular Multilevel Converter. 3. Electrical Drives. 4. Synthetic Inertia. 5. Common-mode Voltage. I. Watanabe, Edson Hirokazu. II. Universidade Federal do Rio de Janeiro, COPPE, Programa de Engenharia Elétrica. III. Título.

Agradecimentos

Gostaria de agradecer ao meu orientador, Professor Edson H. Watanabe, por ter me aceito como aluno e por ter dado inúmeras contribuições para este trabalho. Seu grande conhecimento e interesse por assuntos técnicos são inspiradores e foram benéficos na realização desta dissertação.

Agradeço a Márcia Coelho, seu suporte logístico foi importante para este trabalho e tenho certeza de que o é para toda a produção científica realizada no laboratório Elepot, obrigado. Também envio meus agradecimentos aos membros da banca pelos comentários e pelo tempo utilizado na avaliação deste trabalho.

Este trabalho não teria sido possível na sua forma atual sem o suporte do Operador Nacional do Sistema (ONS). Agradeço a Leandro Dehon Penna, pelo apoio. Ainda no âmbito do ONS, agradeço a Alexandre Nohara, pelos diversos ensinamentos e pelas conversas sobre máquinas elétricas e usinas hidrelétricas. Também envio agradecimentos a Daniele Motta, Ricardo Tenório, Guilherme Sarcinelli, Arjan Vinhães, Raquel Alves, Guilherme Bernardes Cunha, Emilly Bizon, Lúcia Mariana e Gustavo Francisco pelas conversas e ensinamentos diversos, vocês foram parte importante dos meus dias ao longo deste período. O conhecimento técnico obtido com vocês no cotidiano ajudou na produção deste trabalho.

Envio ainda agradecimentos aos diversos colegas de mestrado que me ajudaram ao longo do curso. Particularmente sou grato a Gustavo Gontijo, Thiago Tricarico, Marcello Neves e Felipe Dicler, desejo sucesso a vocês.

Envio ainda meu obrigado a Sarah Alves pelo suporte durante este período desafiador e a Frederico Guimarães por conselhos acadêmicos diversos e sobre o processo de se escrever uma dissertação de mestrado.

Agradeço também a minha mãe, Teresa Cristina, pelo suporte ao longo dos anos. Você foi fundamental para qualquer contribuição que eu tenha feito ou venha a fazer, não só este trabalho. Obrigado.

Resumo da Dissertação apresentada à COPPE/UFRJ como parte dos requisitos necessários para a obtenção do grau de Mestre em Ciências (M.Sc.)

USINAS HIDRELÉTRICAS REVERSÍVEIS DE VELOCIDADE VARIÁVEL BASEADAS EM CONVERSORES MODULARES MULTINÍVEL: MODELAGEM, CONTROLE E ANÁLISE DA OPERAÇÃO EM MODO DE BOMBEAMENTO

Matheus Soares da Silva

Dezembro/2020

Orientador: Edson Hirokazu Watanabe

Programa: Engenharia Elétrica

Este trabalho estuda o comportamento de Conversores Modulares Multinível (MMC) controlando máquinas síncronas em usinas hidrelétricas reversíveis de velocidade variável. Esta topologia baseada em MMC foi proposta na literatura como uma possível tecnologia de armazenamento de energia em larga escala capaz de prover serviços ancilares ao sistema elétrico de potência, ao mesmo tempo que pode ser implementada através da renovação de usinas reversíveis de velocidade fixa já existentes. O modo de bombeamento deste tipo de usina apresenta importantes diferenças em relação a outras aplicações já maduras tecnologicamente para o MMC, tais como elos de corrente contínua. A operação em baixa frequência durante a partida da usina e o controle de máquinas síncronas de centenas de MW são, por exemplo, exclusividade das usinas reversíveis de velocidade variável. Esta dissertação apresenta resultados de simulações utilizando um modelo detalhado, construído em PSCAD/EMTDC, deste tipo de aplicação do conversor MMC. Contribuições referentes à técnica de controle aplicada durante a operação em baixa frequência, baseada na injeção de tensão de modo comum, são apresentadas. Considerações relativas ao projeto do conversor e uma descrição detalhada do sistema de controle também o são. Além disso, os resultados da implementação do conceito de inércia sintética durante o modo de bombeamento também são apresentados.

Abstract of Dissertation presented to COPPE/UFRJ as a partial fulfillment of the requirements for the degree of Master of Science (M.Sc.)

VARIABLE SPEED PUMPED HYDRO BASED ON MODULAR MULTILEVEL CONVERTERS: MODELING, CONTROL AND ANALYSIS OF PUMPING-MODE OPERATION

Matheus Soares da Silva

December/2020

Advisor: Edson Hirokazu Watanabe

Department: Electrical Engineering

This work deals with the behavior of a Modular Multilevel Converter (MMC) driving synchronous machines in variable-speed pumped hydro storage plants. This MMC-based topology has been proposed as one capable of implementing large-scale energy storage with fast dynamics and ancillary services while being possibly realized via retrofitting of existing fixed-speed pumped hydro storage units. The pumping mode of this application presents important differences in comparison to mature MMC applications, such as High-Voltage Direct Current links. For example, the low-speed operation of pumped hydro storage units during start-up and the control of an electrically excited salient pole machine. This dissertation presents a detailed PSCAD/EMTDC model and the results of time-domain simulations of this relatively new application. Some contributions are made to the start-up procedure technique based on common-mode voltage injection. Considerations on the main circuit design and a detailed description of the control system design are presented. Furthermore, the implementation of synthetic inertia into the pumping mode operation of this large-scale energy storage technology is studied.

Contents

List of Figures

List of Tables

List of Abbreviations

2-DOF PI	Two-degree-of-freedom PI, p. 96
2L-VSC	Two-Level Voltage-Sourced Converter, p. 41
ANPC	Active-Neutral Point Clamped Converter, p. 7
CCSC	Circulating Current Supression Control, p. 52
CMV	Common-Mode Voltage, p. 44
CSC	Current Sourced Converter, p. 41
DFIM	Doubly-Fed Induction Machine, p. 6
EMI	Electromagnetic Interference, p. 42
FACTS	Flexible-ac Transmission System, p. 54
FFR	Fast Frequency Response, p. 101
FOC	Field-Oriented Control, p. 35
FS-PHS	Fixed-Speed Pumped Hydro Storage, p. 5
FSC	Full-size Converter, p. 6
HVdc	High-Voltage direct-current, p. 2
IGBT	Insulated-Gate Bipolar Transistor, p. 72
IGCT	Insulated-Gate Commutated Thyristor, p. 14
IHA	International Hydropower Association, p. 4
KVL	Kirchhoff's Voltage Law, p. 46
LVRT	Low-Voltage Ride-Through, p. 6
MMC	Modular Multilevel Converter, p. 7

MTPA	Maximum Torque per Ampere, p. 36
MVdc	Medium-Voltage direct current, p. 54
NLC	Nearest Level Control, p. 50
PCC	Point of Common-Coupling, p. 79
PHS	Pumped Hydro Storage, p. 3
PLL	Phase-Locked Loop, p. 83
PSC-PWM	Phase-Shifted Carrier PWM, p. 50
PSS	Power System Stabilizer, p. 2
PV	Photovoltaic, p. 4
PWM	Pulse-Width Modulation, p. 49
ROCOF	Rate of change of frequency, p. 2
RPT	Reversible Pump-Turbine, p. 12
SHE-PWM	Selective Harmonic Elimination PWM, p. 50
SM	Submodule, p. 41
SPHS	Seasonal PHS, p. 5
THD	Total Harmonic Distortion, p. 79
TSO	Transmission System Operator, p. 3
U.S DOE	United States Department of Energy, p. 3
VRE	Variable Renewable Energy, p. 1
VS-PHS	Variable-Speed Pumped Hydro Storage, p. 3
VSC	Voltage Sourced Converter, p. 13
ZDC	Zero Direct-Current Control, p. 36

Chapter 1

Introduction

1.1 Challenges in the Operation of Future Power Systems

The operation of electric power systems has, throughout most of the 20th Century, been fundamentally based on the properties of synchronous machines and dispatchable power generation in the form of thermal power (mainly fossil fuel based plants) and hydro power plants. For multiple economical and environmental reasons, this paradigm has been changing in a growing pace throughout the last decades. The current trend is that of renewable power generation based on non-dispatchable sources such as solar radiation and wind. These sources are also characterized by the reliance in power electronics converters in order to interface the traditional ac grid with the technologies used in the immediate primary energy source conversion into the electrical form (e.g. photovoltaic panels and, in the case of wind, asynchronous generation). In Brazil, there is also the trend of hydro power plants based on the run-of-the-river technology [1], which present a limited capability of being dispatched, specially during the dry season.

It is expected that, in this context of widespread adoption of Variable Renewable Energy (VRE), challenges to the stable operation of power systems will arise. A first class of problems is related to the fact that traditional power systems operate based on load forecasting and adjustment of the necessary power generation. As wind and solar power outputs are variable, the system may experience mismatch between energy demand and generation regardless of precise load forecasting. These operational issues may cause renewable energy generation curtailment, lead to unattended loads, and require larger spinning reserves [2]. Another point is related to the stability of power systems. On the face of contingencies, i.e. the disconnection of elements such as interconnections between subsystems, generators or large loads, the frequency of power systems can suffer large deviations and leave what is considered

to be the normal operating range. This might lead to disconnection of power plants by their respective protection schemes, activation of load shedding schemes and even blackouts. This class of stability, known as frequency stability, benefits from characteristics of synchronous generators, such as synchronizing torque, the kinetic energy stored in rotating masses of synchronous machines, and primary frequency regulation capabilities.

The considerably large masses present in synchronous machines rotors are synchronized to the power system frequency before an eventual contingency and, due to their inertia, will oppose fast frequency variation [3]. As a result, the immediate rate of change of frequency (ROCOF) following the contingency is lower for systems with higher inertial levels [4]. It is important to notice that this discussion deals with the rate of change of average frequency, as in the immediate follow-up from a large-scale disturbance the system may present oscillation modes and, therefore, the machines will not be perfectly synchronized, but oscillate against each other [5]. If the system possesses small-signal stability, these oscillations will be dampened out by damper circuits of the synchronous machines and controls such as Power System Stabilizers (PSS). The explanation presented here assumes small-signal stability. Figure 1.1 depicts a simplified representation of the behavior of an electrical subsystem average frequency after a contingency-related interconnection loss. In the shown time range (seconds), the main factors are the system's inertia and its primary frequency response. As expected, after the contingency the system will stabilize in a different frequency, which differs from the initial one by the quantity Δ_{fss}. The system will subsequently move into a new frequency state using secondary frequency regulation, which is not captured in the behavior shown in Figure 1.1

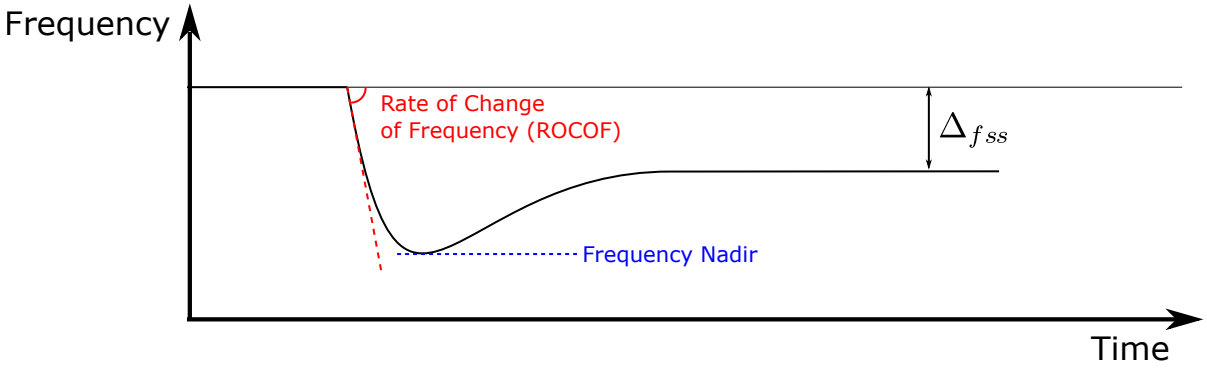

Figure 1.1: A possible shape of a frequency curve related to contingencies in interconnected electrical power systems.

As power electronics based generation and power imports via High-Voltage direct-current (HVdc) links start to take up a larger share of the total power available, the system may lose inertia and become more susceptible to larger frequency variations [6] [7]. Some countermeasures have been added to the control of power

electronics converters in order to mitigate this condition. For example, commercially available wind energy plants have adopted the virtual, or synthetic, inertia concept, which allows for the converter to quickly remove energy from the rotating wind turbine and inject it into the grid, emulating the natural inertial response of synchronous machines [8]. However, VRE such as wind and solar operate in the Maximum Power-Point Tracking (MPPT) strategy and have no associated large energy storage. Therefore, supply of primary frequency control from usual power-electronics based generation is rarely available [9] [10] [11] [12] [13]. Some Transmission System Operators (TSO) around the world see a lack of inertia as a possible hindrance to the continuous stable increase of VRE penetration [6] [14].

Modern power systems with great penetration of non-dispatchable power sources with power-electronics interface have, therefore, two main challenges. The first one, is related fundamentally to the non-dispatchable nature of the VRE. This specific operation aspect could be greatly improved with technologies capable of reducing the generation-demand mismatch. Large scale energy storage is a possible solution and research in its multiple implementation methods have been gaining traction in the last years [15] [16] [17]. Throughout the 20th Century, countries such as Japan and France have dealt with this specific condition and installed large-scale energy storage in the form of Pumped Hydro Storage (PHS) to operate systems with large share of nuclear power plants, which are operated in a non-dispatchable manner [18] [19]. On the other hand, when the also stochastic nature of VRE, with possibly fast variations is taken into account, large-scale energy storage with the possibility of providing dynamic grid support in the form of frequency regulation, synthetic inertia and other ancillary services becomes desirable [20].

This dissertation focuses on the large scale energy storage technology known as Variable-Speed Pumped Hydro Storage (VS-PHS). This is a relatively new and mostly power-electronics based enhancement of the original, fixed-speed, PHS variant. It has been proposed with the objective of contributing to the operation of modern power systems by presenting multiple ancillary services capabilities.

1.2 Perspectives for Pumped Hydro Storage

Pumped Hydro Storage technology is based, fundamentally, on the conversion of energy in the electrical form to energy in gravitational potential form, and vice-versa. The energy storing process is done by pumping water to an elevated reservoir. This energy is recovered in the same process that occurs in a regular hydro plant, letting the water flow towards the lower reservoir, acting upon a turbine coupled to an electric generator. The United States Department of Energy (U.S DOE) reports that, as of 2019, approximately 96% of the world's large-scale energy storage is imple-

mented using PHS technology [21]. This is the only technologically mature option for utility scale (GWh) energy storage [22] and the most efficient one [23], being capable of reaching the 80% mark in terms of efficiency [24] [25]. Pumped hydro has lower environmental impact if compared to batteries-based storage and its related industry [26]. This happens partially because PHS also presents larger lifetime and therefore does not require replacement costs [27]. According to Katsaprakakis et al. [28], the pumped-hydro technology is the optimum large-scale energy storage for medium and large power systems, both in technical and economical terms. The association of PHS and batteries for isolated power systems relying solely on VRE has been also recently proposed [29].

A detailed report of how PHS enterprises fare in different electricity markets is beyond the scope of this work. The USA's Argonne National Laboratory presents an extensive report on the potential advantages of PHS in the United States power system, in operational and economical terms [30]. Kelman et al. [31] investigate the feasibility of a PHS in the Sobradinho reservoir, in the Brazilian northeast region. They also explore another possible application of pumped hydro's reservoirs: floating photovoltaic (PV) farms. The justification for floating PV is based on the fact that solar panels render useless land that could be used otherwise and, at the same time, operate more favorably when cooled down, what would happen near a large body of water.

The International Hydropower Association (IHA) reports that until 2019 the PHS installed capacity was of approximately 160 GW [32] and is expected to grow approximately 78 GW until 2030, most of it taking place in China as a way of reducing VRE curtailment [27]. In Europe, the installed capacity has grown 2.1 GW in Portugal since 2001, contributing to the considerable increase of VRE in the Portuguese electrical grid [33]. Norway has a great hydro potential and the implementation of pumped-hydro to counteract variations due to offshore wind power has been proposed [34].

Brazilian planning authorities have recently published a report listing possible sites for PHS units in the state of Rio de Janeiro. A set of 15 feasible locations has been chosen, totaling 63 GWh of stored energy with an estimated global efficiency of 75% [35]. A similar screening of feasible PHS locations has been done in Australia, identifying hundreds of locations and considering the exportation of renewable energy to Southeast Asia through HVdc links [36]. In recent years there have been research initiatives regarding PHS including universities and industries in both Europe [2] [37] and Brazil [38]. Table 1.1 shows some of the Pumped-Hydro Storage Units currently operational, and their respective energy storage potential.

Table 1.1: Some examples of currently operational pumped-hydro storage units. Data based on the International Hydropower Association map [39]

PHS plant	Location	Energy Storage Capacity	Power Rating (Pumping Mode)
Goldhistal	Germany	8.48 GWh	1060 MW
Baixo Sabor	Portugal	3.4 GWh	189 MW
Grand Maison	France	34.8 GWh	1200 MW
Nygard	Norway	65.82 GWh	56 MW
Zhanghewan	China	5.98 GWh	1000 MW
Omarugawa	Japan	10.25 GWh	1200 MW
San Luis	USA	509.71 GWh	424 MW

Pumped-hydro units are capable of energy storage in multiple time-frames, a high-head PHS built using a major river as the lower reservoir and capable to long-term (up to pluriannual) regularization capacity is known as a Seasonal PHS (SPHS), and is capable of making contributions to the whole river cascade, it has been proposed as an option for the Brazilian Power System [40]. Hunt et al. [41] identified a worldwide energy storage capacity for SPHS of 17.3 PWh, with estimated cost under 50 US$/MWh. Also according to this paper, the average land requirement for this kind of high-head PHS is within the 1.2 and 20 km^2/TWh. Long-term pumped-storage can also contribute to water management in countries which are prone to water shortage in some periods of the year.

Even though the world's first PHS unit is almost 100 years old and the concept is well established, there are still new proposals being made in terms of mechanical parts [42] and reservoirs choices. For example, the idea of underground reservoirs, possibly using abandoned mines has been proposed as a way of minimizing costs and possible environmental impacts [40] [43].

With the ongoing advances in high-power electronics and the falling prices of the associated high-power semiconductor devices [44], there is growing interest in the Variable Speed Pumped Hydro Storage (VS-PHS) units. This variant of the conventional Fixed Speed Pumped Hydro Storage (FS-PHS) allows this kind of unit to quickly and precisely modulate its power flow, leading to an electrical behavior better suited to modern power systems [44] [45], where large sudden energy mismatches can occur due to the behavior of primary sources such as solar radiation and wind speed [7]. The possible offer of ancillary services from power-electronics interfaces PHS is also beneficial to the grid and a source of income to the plant unit. For example, the Frades II plant, in Portugal, has 13% of its income from ancillary services [33]. Vargas et al. [46] evaluate the economics of retrofitting fixed speed units to variable speed units, reaching profitable results when participation on ancillary service markets are taken into account. Another promising application concerning high-power converters is the connection of pumped hydro storage

to Multi-Terminal HVdc grids, this is the case for the Fengning PHS, part of the Zhangbei four-terminal dc grid project, currently under development in China [47] [48].

The IHA pumped-hydro storage map [39] indicates that, globally, there are 15 units now operating or under construction with variable speed capabilities. From that number, almost all of them are built using the DFIM (Doubly Fed-Induction Machine) topology [24]. As in the wind power production market, the fact that the DFIM topology allows for the use of a smaller converter is beneficial. However, for PHS units, there are specific advantages related to full-size converters (FSC) in contrast with DFIM:

- Start-up of the pumping mode of DFIM based PHS units requires extra electrical equipment [49]. According to some authors, the zero-frequency torque of the DFIM solution is not enough to start the pump while it is submerged, and this requires a time-consuming procedure known as de-watering, or blow-down [24] [44] [50]. If compared to FSC based PHS, the start-up time is considerably longer [51];

- FSC units can operate as STATCOM even if the machine is out of operation [18] [44];

- FSC units can be built from retrofitting of existing fixed-speed PHS [24] [52], that is the case of Grimsel 2 [53];

- Low-voltage Ride-Through (LVRT) is a challenging requirement for DFIM units, requiring special protection schemes or the oversizing of the converter [24] [54]. The converter oversizing factor can reach values higher than 3 [20];

- The rotor of induction machines employed in DFIM configurations are more complex, requiring voltages in the kV range; approximately five times the number of brushes required for the FSC based on electrically excited synchronous machines; losses approximately eight times higher, and an overall higher failure probability than the rotors of electrically excited synchronous machines [20] [54];

- If the variable-speed operation happens during both the pumping and generating mode, an optimized synchronous machine design can be made for the operation with FSC, leading to smaller costs that might even offset the converter costs [55].

Despite the possible advantages, there is only a single, as of 2020, operational unit using the FSC configuration. The higher power levels related to this kind of unit, if

compared to wind power generation, brings up the requirement for the application of multilevel inverters. The Grimsel 2 unit employs Active Neutral Point Clamped (ANPC) converters, built by ABB. To illustrate the power level requirements, Table 1.2 shows the power levels of some PHS of the variable-speed type, the power levels are at least ten times higher than that of commercially available wind turbines, and in most cases a hundred times higher.

Table 1.2: Some examples of variable-speed pumped-hydro storage units [56]

PHS plant	Location	Power Rating per Machine (Pumping Mode)
Goldhistal	Germany	265 MW
Frades II	Portugal	372 MW
Nant de Drance	France	172 MW
Tehri	India	255 MW

To build VS-PHS based on full-size converters, Steimer et al. [44] have proposed in 2013 the application of the Modular Multilevel Converter (MMC), a topology flexible in terms of voltage and power capabilities proposed by Rainer Marquardt in 2002 [57]. The application of the MMC to VS-PHS has, conceptually, many advantages both over the DFIM configuration and over the FSC configuration based on monolithic converters such as the ANPC. Many of those advantages are also true for the HVdc market, which has seen an intense growth of the MMC-based solution. Some advantages are:

- MMC-based FSC requires only very reduced filters, or none at all, if compared with monolithic solutions [57];
- MMC-based FSC is related to smaller common-mode voltage levels [58];
- MMC-based FSC, owing to its converters modularity, is easier to maintain and to repair [44];
- Also owing to its modularity, the converter can be built in different spatial configurations, molding itself to room constraints that might be present inside dams [44];
- The drive configuration can be built without transformers, while monolithic converters may require several parallel or series connections in order to attain the necessary multi-pulse behavior (see, for example, [49] and [59]).

One important possible drawback of the MMC, though, is the fact that this topology is prone to problematic voltage ripples when under low-frequency operation [60] [61]. Many control techniques have been proposed to circumvent this problem. This dissertation has the objective of, among other things observe the behavior of the

MMC during start-up of the pumping system, when it will have to deal with low frequencies.

1.3 Objectives

This work has the objective of investigating the VS-PHS based on the Modular Multilevel Converter (MMC) acting as a drive for an electrically excited synchronous machine. This implementation of VS-PHS has been conceptually proposed by Steimer et al. [44] but is yet to be built and operated commercially. While there is at least one prototype [54], works analyzing the behavior of such a plant taking into account detailed vector control dynamics and MMC internal variables are yet to be published. The present dissertation aims to partially fill this gap, focusing on the pumping mode operation and attempting to follow the operational procedures of Grimsel 2, the only currently operational VS-PHS based on a full-size converter.

More specifically, the control system of the MMC-based back-to-back configuration is designed and its correct functioning is verified via time-domain simulation using PSCAD/EMTDC. This simulation presents some level of detail that has not been implemented in a single simulation in previous literature work:

- The hydraulic system is represented in detail for the pump-mode operation by its non-linear equations, as developed by Liang et al. [62];
- The Modular Multilevel Converter is represented by a detailed model up to the submodule level [63]. The MMC internal variables, such as circulating currents and submodule voltages, are observed. Some previous works represent the converter as a regular Voltage Sourced Converter [25], or using averaged models [64] [65];
- MMC main-circuit design for this specific application without transformers on the machine-side of the back-to-back is done and possible limitations of the current technology are addressed;
- MMC control system is designed not only in terms of external variables but also in terms of circulating current control and low-frequency operation control strategy;
- A detailed field-oriented control is designed for the operation of a synchronous machine with detailed parameters, including non-linearities of the magnetizing branch and damper winding currents contributions;
- The start-up procedure is explored, specially in terms of the behavior of the converter. The procedure is similar to the one applied in the commercial

operation of Grimsel 2, the world's only variable-speed pumped-hydro storage plant based on full-size converter technology, as reported in [53];

- The impacts of synthetic inertia applied during pumping mode operation are investigated, both in terms of contribution to the frequency stability of the power system and in terms of the repercussions to the VS-PHS unit internal variables.

While the objective is to advance, both in scope and level of detail, the work presented by some previous literature on the subject, this is a complex and multidisciplinary subject and, therefore, some important topics on Pumped Hydro Storage units are not included:

- No investigations on possible instabilities of hydraulic nature are performed, even though this kind of phenomena is reported [66], operation under conditions prone to cavitation and other hydraulic problems is simply avoided;
- No considerations about electrical power losses are done;
- Based on the current operation of Grimsel 2, where the converter is bypassed in the generating mode, only the pumping mode operation is investigated;
- During the electrical drive control design, it is considered that the machine's rotor position is known. That is, a rotor decoder is considered to exist. The author acknowledges that, for such an application, sensorless control would probably be very advantageous. However, for the main topics of this dissertation, regarding power system interactions and start-up procedures, there is no sensible advantage in implementing sensorless control. Implementing regular vector control was considered to be an important first step in this field of research and the implementation of sensorless control is considered to be a source of interesting future work;
- No economical feasibility studies are presented.

1.4 Contributions of this Dissertation

As a result of the investigations, this dissertation brings the following contributions to this research field:

- A transfer function to describe the relationship between power and speed for the model of a PHS operating on pump mode, presented by Liang [62], is developed and used to design a control system with nested speed and power control loops;

- It is proposed to slightly modify the already proposed MMC low-frequency operation techniques by employing a differentiable approximation of a square wave as common-mode voltage. This contribution resulted in a conference paper [67].

1.5 Organization of this Dissertation

Besides the present Chapter, which contains the introduction, this dissertation is organized in the following manner:

- Chapter 2 presents, in further detail, the VS-PHS technology and the mathematical modeling applied throughout this work;
- Chapter 3 presents the mathematical modeling of the electrical equipment related to a MMC-based FSC VS-PHS. The vector-control scheme and the start-up procedure technique are also explained;
- Chapter 4 presents the methodology applied to the simulations, control, and main circuit design, describing and justifying the different criteria chosen throughout the dissertation;
- Chapter 5 presents the main-circuit design of the simulated Modular Multilevel Converters;
- Chapter 6 presents the design of control systems;
- Chapter 7 presents the simulation results and discusses the findings;
- Chapter 8 contains the conclusions of this work.

Chapter 2

Pumped Hydro Storage: Technology and Mathematical Modeling

This chapter aims to present a bibliographical review of Pumped Hydro Storage (PHS) technology, basic concepts, and hydraulic models useful for power systems dynamic performance studies.

2.1 Pumped Hydro Storage Technology and Operational Experience

Pumped Hydro Storage has been largely deployed throughout the 20th Century in, for example, Japan and USA, as a way to guarantee maximum efficiency in the operation of nuclear and thermal power plants [24] [68]. Historically, most PHS units have been of the fixed speed type. In this type of unit, the dynamics of the PHS plant are relatively slow and, because there is no power-modulation capability during pump operation, there are start-stop cycles spread throughout the day, happening once per a couple of hours. The immediate advantage in this historical context is the fact that, with fixed speed Pumped Hydro Storage, thermal units can operate with relatively constant power output, leaving the load-generation coupling role to the stored energy. Figure 2.1 shows the general idea of this load-generation dynamics.

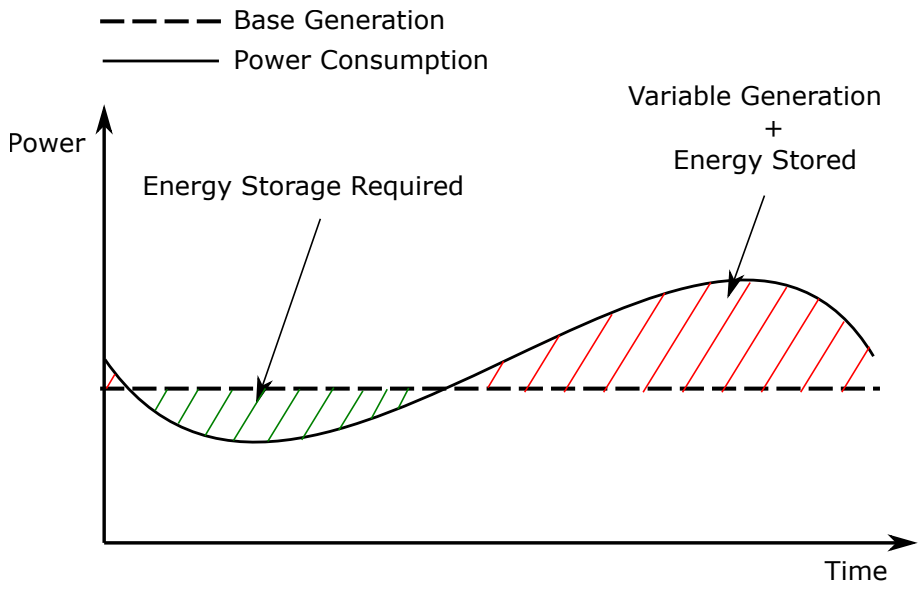

Figure 2.1: Energy storage role in coupling power generation and demand.

It is possible to categorize PHS units in multiple ways. First, depending on the hydraulic system two configurations are possible:

- Reversible Pump-turbine and
- Ternary System.

In the Reversible Pump-Turbine (RPT) configuration, a reversible turbine is employed, operating both pumping water upwards and generating electrical energy from falling water. Every reaction turbine is theoretically of this kind and can be used to build this kind of PHS [69]. Usually the Francis Reversible Pump-Turbine is employed [24]. Most PHS units currently in operation are of this type, owing to their much simpler construction and therefore, lower initial costs [24]. The present work focuses exclusively on units employing the RPT configuration. Ternary systems, on the other hand, have two machines, each one exclusively dedicated to an operation mode. This kind of PHS has advantages such as less start-stop cycles and faster transition between operation modes. The main disadvantage is the more expensive and complex construction, requiring twice the number of penstocks, machines and every related equipment [52].

PHS can also be categorized in regard to the operation of the electrical machine coupled to the turbine. There are two configurations:

- Fixed Speed Pumped Hydro Storage (FS-PHS) and
- Variable Speed Pumped Hydro Storage (VS-PHS).

Commercially available VS-PHS units are based on power electronics converter technology. Their implementation began in 1990 with the Yagisawa plant [23].

This sort of unit presents a faster and more delicate power control, allowing the system operator to better match generation and demand [52]. Figure 2.2 shows a modified version of the pumping region shown in Figure 2.1, with a comparison between the behavior of fixed speed and variable speed units, both with four sub-units. It is shown that the VS-PHS variant can track the energy mismatch more precisely. It also leads to less start-stop cycles. VS-PHS presents such a behavior even while on pumping mode and is also capable of continuous and bidirectional pump-turbine mode transition [51]. These advantages lead to a smaller need for fossil-fuel based reserve generation and to a longer life-span for the PHS turbine [52], which is negatively affected by start-stop procedures [70] [71]. It is also important to notice that Figure 2.2 presents a load-generation mismatch with more spikes and variations, if compared with Figure 2.1, this is expected in a modern scenario with larger penetration of VRE, where increased system flexibility is deemed necessary.

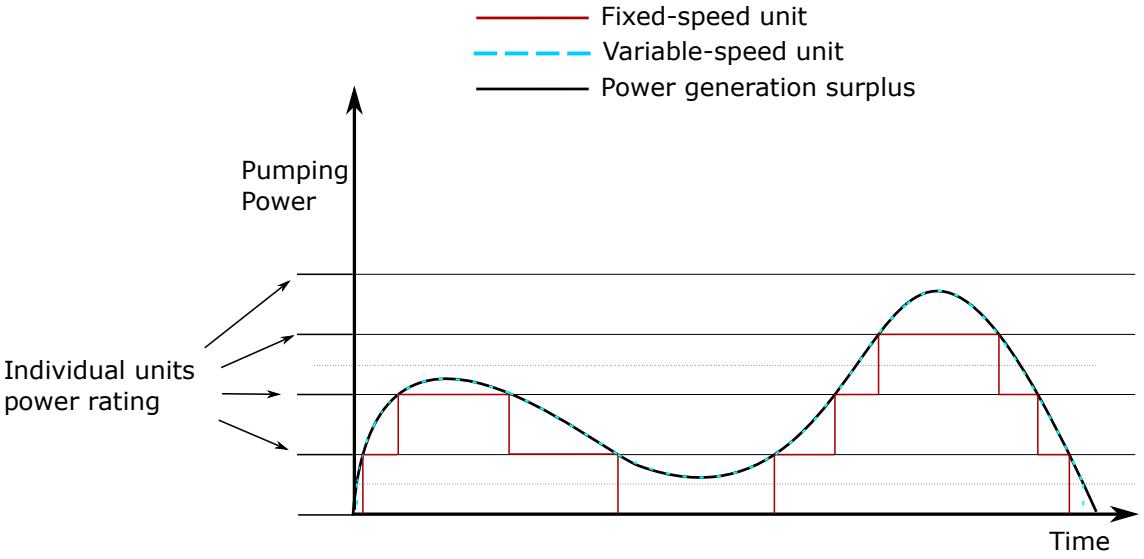

Figure 2.2: Comparison between Variable Speed and Fixed Speed Pumped Hydro Storage in the coupling energy generation and demand.

VS-PHS is advantageous to the power plant not only to extend the lifespan of the equipment, but also because, as the hydraulic system can now operate in multiple speeds, it can constantly attempt optimal speed operation. Optimal speed is a function of water flow and is usually outside of the FS-PHS operating range [72]. This relationship is represented by turbine manufacturers by an experimentally obtained contour line known as the turbine's hill chart [25] [73].

The first VS-PHS units (e.g. Yagisawa and Ohkawachi, both in Japan) were based on the Thyristor technology, more specifically on cycloconverters [74]. Their modern counterparts, on the other hand, are based on Voltage-Sourced Converters (VSC) and are, just like modern wind generation, mainly based on two topologies: doubly-fed induction machines and full-size back-to-back converter-fed synchronous

machines [24] [59]. Examples of both topologies are shown in Figure 2.3.

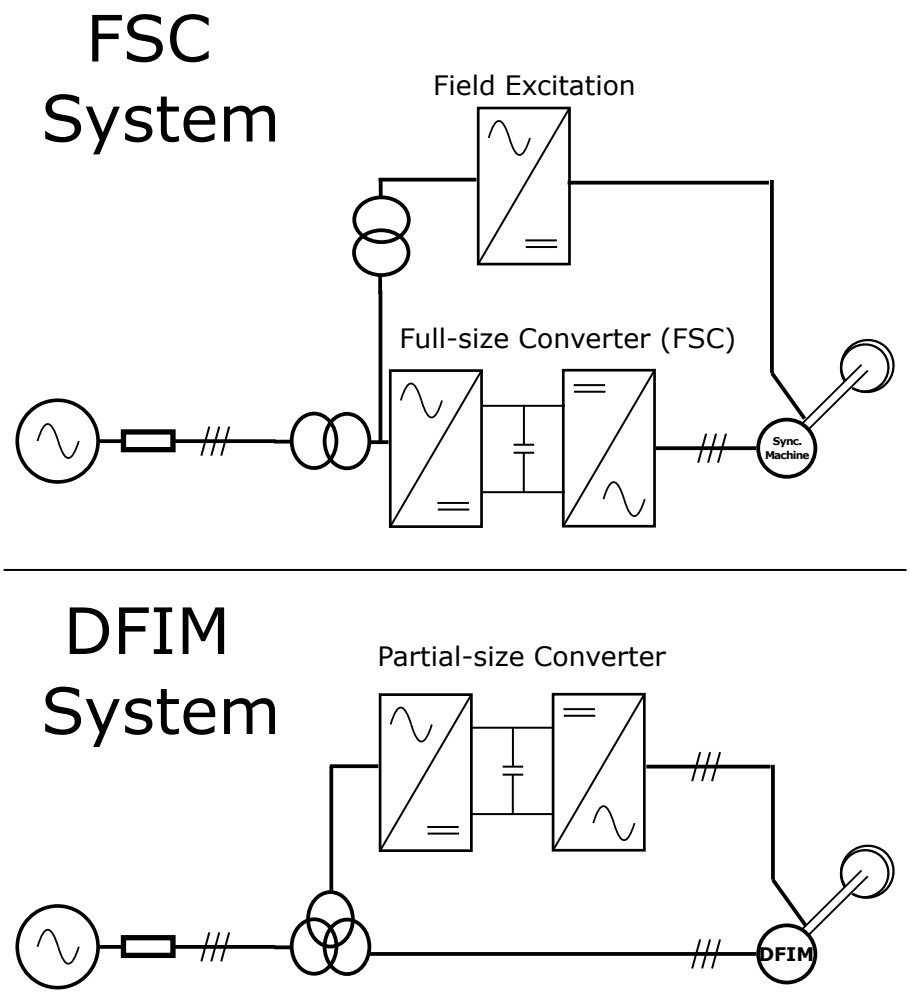

Figure 2.3: The Full-Size Converter and Doubly-Fed Induction Machine topologies.

The current market dominance of DFIM technology has, according to some authors, a decreasing trend. The downsides of full-size converters are expected to become less significant because they are fundamentally related to the still advancing high-power electronics technology. That is, with currently advancing high-power converter technologies, such as IGCT (Insulated-Gate Commutated Thyristor) switches and advanced topologies such as the MMC, it is expected that the FSC technology will push the current 100 MW feasible power to higher levels [20] [24] [44] [51] [54] [59]. The downsides of DFIM, on the other hand, are expected to remain relatively stable, for most of them are related to the fundamental characteristics of the construction of induction machines.

While variable speed units allow for wider range of operation, specially when using the full-converter topology, hydraulic limitations related to stability and cav-

itation must still be respected [66].

2.1.1 Grimsel 2 Operational Experience

Grimsel 2 is a pumped-hydro storage unit located in the Swiss Alps. The unit has three turbines operating with fixed-speed and one of them with variable-speed. This variable-speed turbine is of special interest because it is the only, as of 2020, operational VS-PHS based on a FSC. Table 2.1 shows some of the characteristics of Grimsel 2 variable-speed operation.

Table 2.1: Some characteristics of the Grimsel 2 VS-PHS [59] [53] [70].

Characteristic	**Value**
Converter Nominal Power	100 MVA
Nominal Voltage	13.5 kV
Frequency-range	46-51 Hz
Nominal Hydraulic Head	400 m
Converter Topology	Active Neutral-Point Clamped Converters (ANPC)

The unit commenced operation in 2011. Throughout the first 11 months of operation it operated 43% of the time in the controlled pumping mode without presenting specific problems [59]. This unit pumping-mode start-up happens against a closed spherical valve until it reaches 600 rpm. After that, the spherical valve is opened and the speed is set according to the desired pumping power, as function of the hydraulic head. The start-up procedure takes, approximately, 60 seconds [59]. The control scheme of the converter seems to consist of a nested power-speed loop, containing also primary frequency response and head adaptation [53]. In this work the same nested power-speed loop will be designed and implemented, disregarding head adaptation.

2.2 Modeling of Hydraulic Components of PHS Units Operating on the Pumping Mode

Hydro power generation is based on the conversion of water gravitational potential energy to its electrical counterpart. In fundamental terms, a hydro unit consists in two bodies of water (usually reservoirs, but not always) connected through a water conduit (here called the penstock). The water flow (Q), given in m^3/s, passing through this conduit propels a turbine, which is coupled to an electric generator. Figure 2.4 shows a fundamental schematic of a PHS unit. The height difference between the bodies of water is known as the head (H), given in meters.

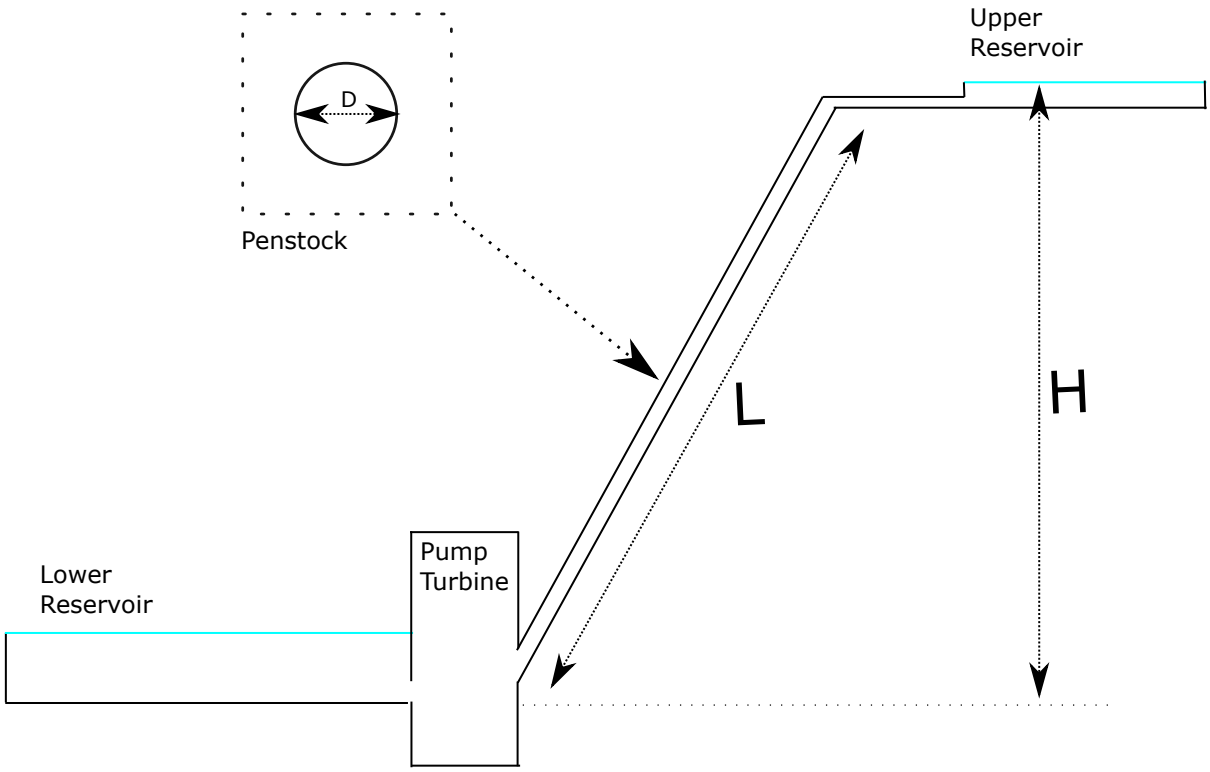

Figure 2.4: Conceptual drawing of a pumped-hydro storage unit.

The amount of power for a certain PHS configuration is given by [19] [75]:

$$P = \rho\, g\, H\, Q\, \eta \tag{2.1}$$

where ρ is the water density; g is the gravitational acceleration in the unit location, given in m/s^2; and η is the pump efficiency. For the design of control systems and development of linear models, (2.1) is usually per-unitized and linearized around the nominal values of P, H and Q (which are all equal to one). As the discussion presented here regards pumps, a subscript p is added. This process results in (2.2) [75] [76]:

$$\Delta P_p = \Delta H_p + \Delta Q_p. \tag{2.2}$$

The hydraulic modeling of hydro plants can be made in different levels of detail depending on the kind of study and the plant characteristics. For example, some installations have a surge tank with the objective of reducing pressure related to rapid closure of the turbine wicket gates [19]. This work will disregard this kind of element, specially taking into account the fact that no studies related to fast gate closure will be performed.

Following the approach shown throughout the literature [19] [62] [76], the modeling developed here is divided in two sections, the first one for the penstock, the

second one for the pump-turbine. In some plants, multiple pump-turbines share a single tunnel before it is divided in multiple penstocks, this will not be the case studied here and, therefore, analysis for this kind of structure is not covered.

The water column in the penstock presents some dynamical characteristics, namely: water inertia and water compressibility (also known as water hammer effect). It is not always necessary to add these dynamical effects in the model for power system studies [76]. Water compressibility effects are specially important in long penstocks [19]. PHS units are usually only considered to be feasible with a rate between length of penstock and head of 10 or less [69], many have a ratio of 5 or less [68]. Therefore, water compressibility is disregarded and an inelastic water column model is studied.

Due to the different modes of operation of PHS units, an approach reported in literature is to use two hydraulic models for the Reversible Pump Turbine. By using this approach, electrical studies involving pumping mode (for example, for analysis of the start-up procedure) would use a pumping-mode model and studies for the investigation of the generating mode would use another model [62] [77]. However, the practical operation of VS-PHS based on full-size converters presently bypasses the converter during generating mode [53], making the unit operate as a regular hydro power plant. Therefore, this dissertation focuses only on the pumping mode model.

2.2.1 Penstock Model

The dynamics of the water column within the penstock are given by the differential equation [76]:

$$\frac{d\Delta Q}{dt} = -\frac{\Delta H}{T_w}, \tag{2.3}$$

where T_w represents the quantity known as the water starting time, related to the amount of time it takes for the water column of a given penstock to start moving. It is function of the geometrical properties of the penstock [19] [62] :

$$T_w = \frac{LQ}{A\,Hg}. \tag{2.4}$$

where A is the penstock transversal area.

The head H in this case is not the same as the pump head H_p. H is given by the composition of the nominal head H_n, the penstock and gate-related head losses H_l, and the head developed by the pump H_p. If a unitary H_n, in per-unit, is considered, the pump must develop $|H_p| \geq 1.0 + |H_l|$ to guarantee upwards water flow:

$$H = H_n - H_p - H_l \tag{2.5}$$

the relationship between flow and the variable head losses H_l is given by:

$$\begin{aligned} H_l &= f_e(|Q|.Q) \\ f_e &= f_c + f_{gate} \end{aligned} \tag{2.6}$$

differently from penstock models employed in traditional hydro modeling [19], the friction constant related to the head loss in the penstock, f_e, is a sum between a stationary friction f_c and a variable one, f_{gate}, [62] related to the gate position G by:

$$f_{gate} = \frac{G_{max} - G}{G} \tag{2.7}$$

2.2.2 Pump-Turbine Model for the Pumping Mode Operation

The head generated by a centrifugal pump as function of speed ω and flow can be described as [62]:

$$H_p = a_o\omega^2 + a_1\omega|Q_p| + a_2Q_p^2. \tag{2.8}$$

Throughout this work a set of constants $a_{0,1,2} = (1.7, -0.2, -0.3)$ is employed. These values are similar to the ones applied by Liang et al. [62] and present a behavior similar to the reported for Grimsel 2 [53]. Figure 2.5 shows the pump behavior for these constants and different speed values. As previously written, the pump must be able to develop a head larger than 1.0 in order to actually propel water. Therefore, Figure 2.5 shows that the pump can not operate, for example, with $\omega \leq 0.7$. In the next subsection the possible operating points of the pump as function of both speed and gate is shown.

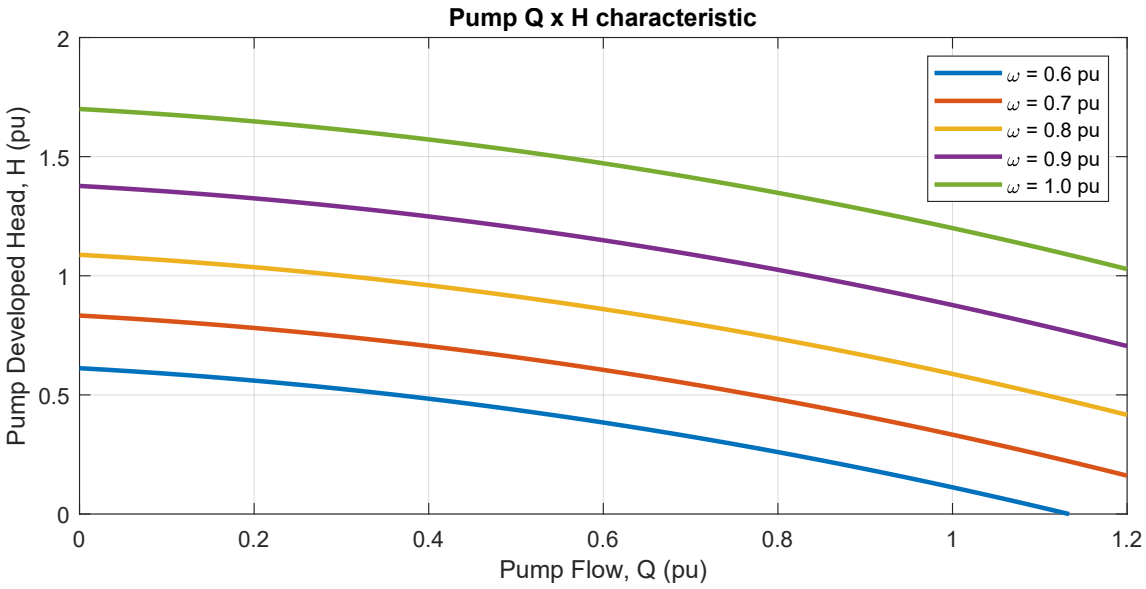

Figure 2.5: Relationship between speed, developed head and water flow in the centrifugal pump used in this work.

2.2.3 Complete Hydraulic Model of Pumping Mode Operation

The complete hydraulic model of the plant is obtained by combining the models described in the previous subsections and can be represented as shown in Figure 2.6.

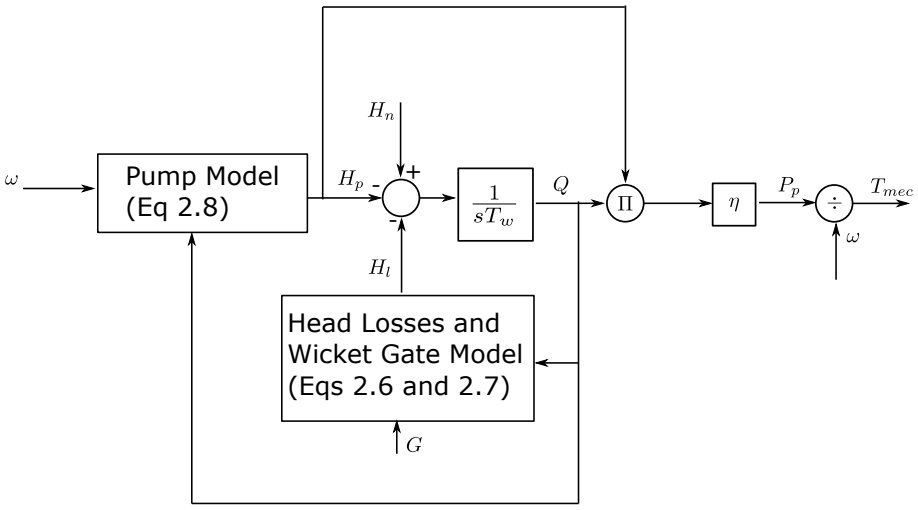

Figure 2.6: Complete hydraulic model of the pumping-mode.

Figure 2.5 is now modified and only the pump characteristic curve for $\omega = 1.0$ pu is kept. The steady-state head requirements both from nominal head and head losses in the penstock and gate are added for different gate values and, for steady-state, of course, both values must be equal, otherwise flow would keep increasing or decreasing. Figure 2.7 shows that, for $\omega = 1.0$ pu, there are multiple possible

operating points, depending upon the wicket gate position. As the developed head for this speed is relatively high, the model presents no limitations, from the point of view of keeping an upwards flow.

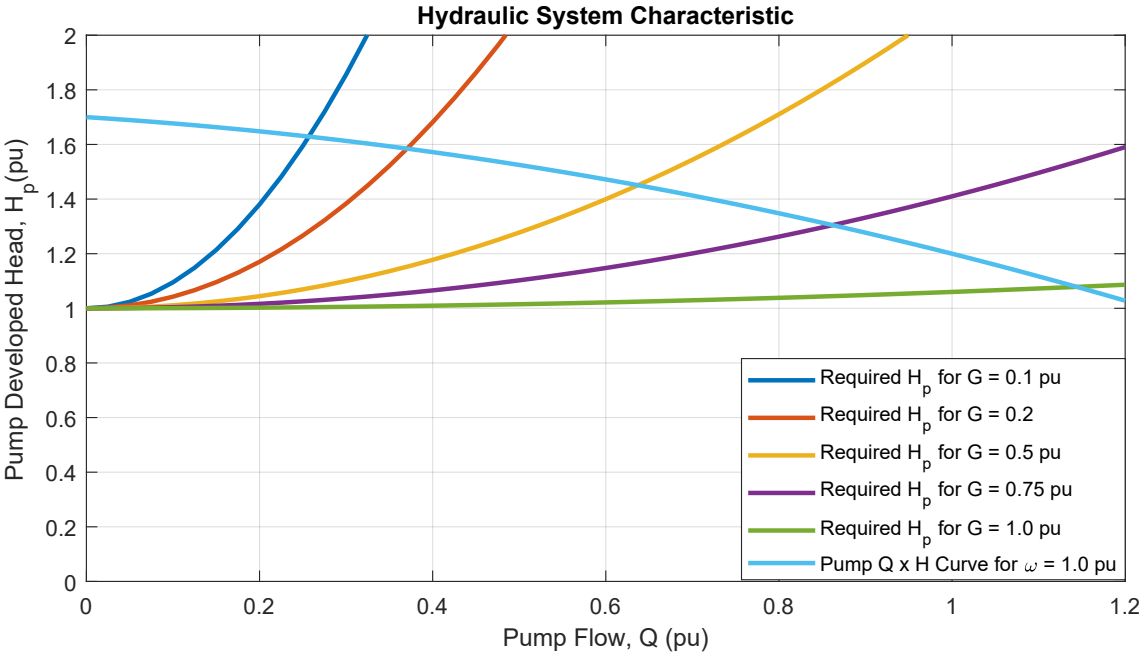

Figure 2.7: Complete hydraulic system characteristic for different gate positions.

Avoiding flux reversal is not the only limitation, there is also the maximum rated power of the pump, Figure 2.8 shows that, for $\omega = 1.0$ pu, the intersection between both characteristics (penstock and pump) would only happen for power levels of almost 1.2 pu. It can be seen that for $\omega = 0.95$ pu the pump power is very close to 1.0 pu. So that value is chosen to be the maximum operating speed. The minimum operating speed is set to $\omega = 0.8$, pu leading to a range of 0.15 pu, not very distant from the 0.1 pu range of Grimsel 2 [53].

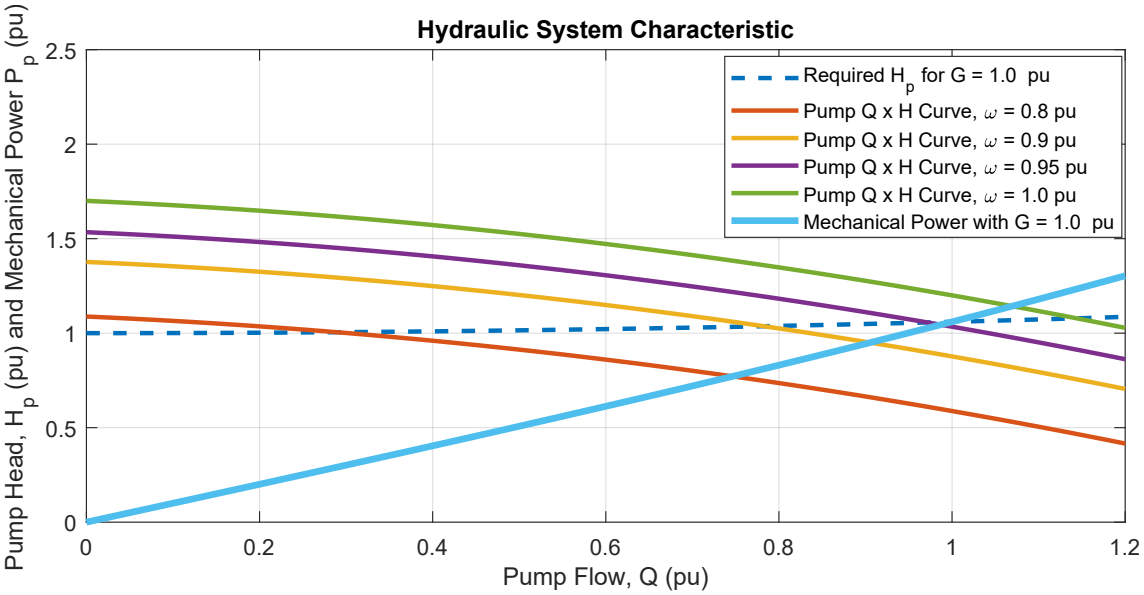

Figure 2.8: Complete hydraulic system characteristic. ©2020 IEEE. Reproduced from [67].

2.2.4 Developed Transfer Function Between Mechanical Power and Pump Speed

Now that the complete hydraulic model has been presented, a transfer function that is not explicitly presented in the literature must be developed. As will be seen later, the electrical drive controlling the machine will have control loops for both speed and power. It becomes necessary, for a correct control design, to know the transfer function relating both variables.

The development begins with the linearization of (2.8) around a given operating point $\omega = \omega_0, Q_p = Q_{p0}$:

$$\Delta H_p = \frac{2\omega_0\, a_0 + a_1 Q_{p0}}{a_0\omega_0^2 + a_1\omega_0 + a_2 Q_{p0}^2}\Delta\omega + \frac{a_1\omega_0 + 2a_0 Q_{p0}}{a_0\omega_0^2 + a_1\omega_0 + a_2 Q_{p0}^2}\Delta_{Q_p}. \tag{2.9}$$

For brevity, two constants are defined, $A = \frac{2\omega_0\, a_0 + a_1 Q_{p0}}{a_0\omega_0^2 + a_1\omega_0 + a_2 Q_{p0}^2}$ and $B = \frac{a_1\omega_0 + 2a_2 Q_{p0}}{a_0\omega_0^2 + a_1\omega_0 + a_2 Q_{p0}^2}$, (2.9) is rewritten accordingly:

$$\Delta H_p = A\Delta\omega + B\Delta_{Q_p}. \tag{2.10}$$

As a second step, the linearized differential (2.3) is rewritten and the Laplace Transform is applied to it, resulting in:

$$T_w \Delta Q s = -\Delta H, \tag{2.11}$$

substitution of (2.10) into (2.11) leads to the transfer function:

$$\Delta Q = \frac{A\Delta\omega}{(s\,T_w - B)} \tag{2.12}$$

which relates variations of water flow and pump speed, as the pump will operate with constant and fully opened wicket gates, the head losses related to the gate H_l are disregarded. From now on the p subscripts are dropped. As the objective is to relate mechanical power and pump speed, the linearized mechanical power (2.2) is substituted into (2.12). This yields:

$$\Delta P_m = \frac{A}{(s\,T_w - B)}\Delta\omega + \Delta H. \tag{2.13}$$

Revisiting (2.10) and substituting it in (2.13) leads to:

$$\Delta P_m = \frac{s\,AT_w - AB + A}{(s\,T_w - B)}\Delta\omega + \frac{B(s\,T_w - B)}{s\,T_w - B}\Delta Q. \tag{2.14}$$

The second right-hand term can be further modified by using (2.12):

$$\Delta P_m = \frac{s\,AT_w - AB + A}{(s\,T_w - B)}\Delta\omega + \frac{B(s\,T_w - B)}{s\,T_w - B}\frac{A\Delta\omega}{(s\,T_W - B)}. \tag{2.15}$$

with further algebraic manipulation a transfer function relating speed and mechanical power is obtained:

$$\Delta P_m = \frac{A(s\,T_w + 1)}{(s\,T_w - B)^2}\Delta\omega. \tag{2.16}$$

This process results in a description for the relationship between mechanical power being employed on the pumping process and the pump speed. It is important to observe that the constant B has only negative terms on the numerator, and a positive denominator. Therefore, (2.16) has only left-half-plane poles. The transfer function derived here will be revisited in Chapter 6 during the design of the active power control loop present in the machine-side converter.

2.3 Chapter Conclusions

The literature presents a model for the pumping-mode operation of a VS-PHS, including the effects of wicket gates position. Using this model, a frequency range for the operation of the converter studied in this dissertation has been defined. Besides, in this chapter a transfer function relating variations of mechanical power and pump speed has been developed. This development will be useful during the control design process.

Chapter 3

Modeling and Control of Electrical Components

3.1 Introduction

Figure 3.1 shows a diagram representing the drive configuration studied in this work. This chapter deals with the modeling of the electrical components of this high-power electrical drive. The driven load in our specific case is, of course, a Reversible Pump-Turbine and its modeling has been presented in Chapter 2.

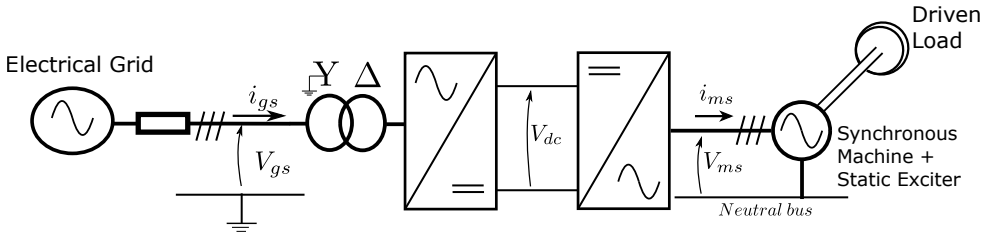

Figure 3.1: Simplified view of the electrical drive being studied.

3.2 Synchronous Machine Modeling

This work will deal exclusively with three-phase, wound rotor, salient pole synchronous machines. A set of assumptions are necessary for the mathematical modeling presented in this section [78] [79] [80].

- The rotor windings can be represented by a set of three equivalent windings distributed amongst two perpendicular axis. In the direct axis (d) there is the field winding (F) and the d-axis damper winding (D). In the quadrature axis (q-axis), there is the q-axis damper winding (Q). This model can be found in the literature as the 2.1 model [81] and fits with the generator data which is

employed on the remaining of this work. More detailed representations of the rotor also exist and are usually employed in turbomachinery [76] [82];

- The stator windings are distributed equally throughout the stator circumference and can be represented by three windings, one for each phase;
- Magnetic non-linearities such as hysteresis and saturation are neglected;
- Capacitances are neglected;
- Resistances have constant values;
- There is no mutual linkage inductance between field and d-axis damper windings. That is, Canay inductance is null [83].

These assumptions alone will still generate a relatively complex model with time-varying inductances. As will be seen later, it is possible to make this model time-invariant by using a reference frame fixed to the rotor. From now on the modeling done using the initial assumptions will be called the "modeling in terms of machine variables", as done in [82]. Later the same equations in the "rotor reference frame" will be explored.

Electrical rotating machines can be modeled by three sets of equations. One of them describes the relationship between the magnetic fluxes in the machine and its electrical currents, this set will be referred to, from now on, as the flux equations.

3.2.1 Flux Equations in Terms of Machine Variables

The stator-referred flux equations for a salient pole synchronous machine are:

$$\begin{bmatrix} \lambda_a \\ \lambda_b \\ \lambda_c \\ \lambda_Q \\ \lambda_F \\ \lambda_D \end{bmatrix} = \begin{bmatrix} L_S & L_{SR} \\ \frac{2}{3}L_{SR}^T & L_R \end{bmatrix} \begin{bmatrix} i_a \\ i_b \\ i_c \\ i_Q \\ i_F \\ i_D \end{bmatrix}. \tag{3.1}$$

where $\lambda_{k\,=\,a,b,c,Q,F,D}$ is the flux linkage of each of the windings described previously and i_k is the current passing through these same windings, L_S is the submatrix with self and mutual inductances of the stator, L_{SR} is the submatrix of the rotor to stator mutual inductances and L_R is the submatrix of self and mutual inductances of the rotor. As (3.1) is a set of linear equations, it is natural to have a matrix of self and mutual inductances. This matrix is henceforth expanded:

$$\begin{bmatrix} L_S & \vdots & L_{SR} \\ \cdots & \cdots & \cdots \\ \frac{2}{3}L_{SR}^T & \vdots & L_R \end{bmatrix} = \begin{bmatrix} L_{aa} & L_{ab} & L_{ac} & \vdots & L_{aQ} & L_{aF} & L_{aD} \\ L_{ba} & L_{bb} & L_{bc} & \vdots & L_{bQ} & L_{bF} & L_{bD} \\ L_{ca} & L_{cb} & L_{cc} & \vdots & L_{cQ} & L_{cF} & L_{cD} \\ \cdots & \cdots & \cdots & \cdots & \cdots & \cdots & \cdots \\ \frac{2}{3}L_{Qa} & \frac{2}{3}L_{Qb} & \frac{2}{3}L_{Qc} & \vdots & L_{QQ} & L_{QF} & L_{QD} \\ \frac{2}{3}L_{Fa} & \frac{2}{3}L_{Fb} & \frac{2}{3}L_{Fc} & \vdots & L_{FQ} & L_{FF} & L_{FD} \\ \frac{2}{3}L_{Da} & \frac{2}{3}L_{Db} & \frac{2}{3}L_{Dc} & \vdots & L_{DQ} & L_{DF} & L_{DD} \end{bmatrix}. \tag{3.2}$$

The formulation of the inductance matrix elements varies for different kinds of rotating electric machinery. We begin by defining the elements of submatrix L_S. For synchronous machines with salient poles the stator self inductances become [82]:

$$\begin{aligned} L_S &= \begin{bmatrix} L_{aa} & L_{ab} & L_{ac} \\ L_{ba} & L_{bb} & L_{bc} \\ L_{ca} & L_{cb} & L_{cc} \end{bmatrix}, \\ L_{aa} &= L_l + L_A + L_B \cos(2\theta_r), \\ L_{bb} &= L_l + L_A + L_B \cos\left(2(\theta_r - \frac{2\pi}{3})\right), \\ L_{cc} &= L_l + L_A + L_B \cos\left(2(\theta_r + \frac{2\pi}{3})\right), \end{aligned} \tag{3.3}$$

where L_l is the stator leakage inductance; L_A and L_B are both constants for a same machine, and $L_A > L_B$. L_B is function of the rotor-saliency and becomes zero for uniform air-gaps [82]. The angle θ_r is defined as the angular displacement of the rotor in relation to some arbitrary direction. The stator mutual inductances become:

$$\begin{aligned} L_{ab} = L_{ba} &= -\frac{1}{2}L_A - L_B \cos\left(2(\theta_r - \frac{\pi}{3})\right), \\ L_{bc} = L_{cb} &= -\frac{1}{2}L_A - L_B \cos\Big(2(\theta_r + \pi)\Big), \\ L_{ca} = L_{ac} &= -\frac{1}{2}L_A - L_B \cos\left(2(\theta_r + \frac{\pi}{3})\right). \end{aligned} \tag{3.4}$$

Now the mutual inductances between stator and rotor windings (submatrix L_{SR}) are defined, the equations presented are already referred to the stator, as shown in

[82]:

$$L_{SR} = \begin{bmatrix} L_{aq}\cos(\theta_r) & L_{ad}\sin(\theta_r) & L_{ad}\sin(\theta_r) \\ L_{aq}\cos(\theta_r - \frac{2\pi}{3}) & L_{ad}\sin(\theta_r - \frac{2\pi}{3}) & L_{ad}\sin(\theta_r - \frac{2\pi}{3}) \\ L_{aq}\cos(\theta_r + \frac{2\pi}{3}) & L_{ad}\sin(\theta_r + \frac{2\pi}{3}) & L_{ad}\sin(\theta_r + \frac{2\pi}{3}) \end{bmatrix}, \quad L_{aq} = \frac{3}{2}(L_A - L_B), \quad L_{ad} = \frac{3}{2}(L_A + L_B). \tag{3.5}$$

where L_{aq} and L_{ad} are the magnetizing inductances in the quadrature and direct axes, respectively. As previously stated, for machines without rotor-saliency, $L_B = 0$. Therefore, in that specific case, $L_{aq} = L_{ad}$.

Finally, L_R can be presented as:

$$L_R = \begin{bmatrix} L_{lQ} + L_{aq} & 0 & 0 \\ 0 & L_{lF} + L_{ad} & L_{ad} \\ 0 & L_{ad} & L_{lD} + L_{ad} \end{bmatrix}, \tag{3.6}$$

where L_{lF}, L_{lD} and L_{lQ} are the leakage inductances of, respectively, the field winding, the d-axis damper winding and q-axis damper winding.

3.2.2 Voltage Equations in Terms of Machine Variables

The second descriptive set contains the voltage equations, relating voltage in each winding with its respective linked flux and electrical current. These relations will exist for stator (3.7) and rotor circuits (3.8) [79]. Positive currents are defined as those leaving the machine's stator:

$$\begin{bmatrix} V_a \\ V_b \\ V_c \end{bmatrix} = -\begin{bmatrix} r_s & 0 & 0 \\ 0 & r_s & 0 \\ 0 & 0 & r_s \end{bmatrix} \begin{bmatrix} i_a \\ i_b \\ i_c \end{bmatrix} + p \begin{bmatrix} \lambda_a \\ \lambda_b \\ \lambda_c \end{bmatrix}, \tag{3.7}$$

$$\begin{bmatrix} V_Q \\ V_F \\ V_D \end{bmatrix} = \begin{bmatrix} r_r & 0 & 0 \\ 0 & r_r & 0 \\ 0 & 0 & r_r \end{bmatrix} \begin{bmatrix} i_Q \\ i_F \\ i_D \end{bmatrix} + p \begin{bmatrix} \lambda_Q \\ \lambda_F \\ \lambda_D \end{bmatrix}, \tag{3.8}$$

where r_s and r_r are, respectively, the electrical resistances of rotor and stator windings and p represents the time-derivative operator. These equations can also be written in the following shorter notation, which will be employed henceforth:

$$[v_{abc}]^T = -r_s[\mathbf{I}]\,[i_{abc}]^T + p[\lambda_{abc}]^T \tag{3.9}$$

$$[v_{QFD}]^T = r_r[\mathbf{I}][i_{QFD}]^T + p[\lambda_{QFD}]^T \tag{3.10}$$

where [**I**] is the identity matrix.

3.2.3 Mechanical Equations in Terms of Machine Variables

The synchronous machine's mechanical variables can be represented by two equations. Equation (3.11) describes the relationship between torques and rotational speed and (3.12) describes the electrical torque production as function of currents passing through the machine windings [82]. As the machine resistances are usually much smaller than its reactances, for this set of equations the resistance values are disregarded. In the PSCAD/EMTDC synchronous machine model, it is not necessary to inform the number of poles of the machine, as the mechanical and electrical speeds are the same in their respective per-unit bases [84]. The development shown here considers that the equations are per-unitized accordingly:

$$T_m - T_e = -J\, p\, \omega_r \tag{3.11}$$

$$T_e = \left(-\frac{1}{2}[i_{abc}]^T \frac{\partial}{\partial \theta_r}(L_s - L_{ls}[\mathrm{I}])[i_{abc}] + ([i_{abc}]^T \frac{\partial}{\partial \theta_r}(L_{SR}\,[i_{QD}]) \right) \tag{3.12}$$

3.2.4 The Rotor-Oriented Reference Frame

The differential equations which relate voltages, currents and flux in synchronous machines (here called the voltage equations) contain inductances which are function of the rotor position and, consequently, of time (except if the rotor is at standstill). This fact brings an extra-level of complexity to the model of the machine, as can be seen from, for example, (3.12). Thankfully, these equations can be simplified with a change of reference frame.

The originally presented voltage equations (3.7) are associated with the concentrated stator windings (a, b and c). R. H. Park was the first to propose a change of variables where these equations are referred to two fictitious windings (q, d) contained within a reference frame fixed to the rotor.

This transformation is henceforth called the Park's Transformation and, as any other real transformation, can be thought of as a transformation between 3-phase variables related to a stationary circuit, and an arbitrary reference frame (which may be rotating or not). This change of variables is expressed in a general mathematical form as [82]:

$$\begin{bmatrix} h_a \\ h_b \\ h_c \end{bmatrix} = K_s \begin{bmatrix} h_q \\ h_d \\ h_0 \end{bmatrix} \tag{3.13}$$

where

$$K_s = \frac{2}{3}\begin{bmatrix} \cos(\theta) & \cos(\theta - \frac{2\pi}{3}) & \cos(\theta + \frac{2\pi}{3}) \\ \sin(\theta) & \sin(\theta - \frac{2\pi}{3}) & \sin(\theta + \frac{2\pi}{3}) \\ \frac{1}{2} & \frac{1}{2} & \frac{1}{2} \end{bmatrix},$$

and h can represent voltage, current or flux linkages. The inverse transformation is:

$$K_s^{-1} = \begin{bmatrix} \cos(\theta) & \sin(\theta) & 1 \\ \cos(\theta - \frac{2\pi}{3}) & \sin(\theta - \frac{2\pi}{3}) & 1 \\ \cos(\theta + \frac{2\pi}{3}) & \sin(\theta + \frac{2\pi}{3}) & 1 \end{bmatrix}.$$

By defining θ as the angular displacement of the rotor in relation to some direction (that is, $\theta = \theta_r$), the Park Transformation (K_r) is defined and the voltage equations cease to contain time-varying inductances.

3.2.5 Flux Equations in the Rotor Reference Frame

Applying Park Transformation K_r to (3.1) yields:

$$\begin{bmatrix} \lambda_q \\ \lambda_d \\ \lambda_Q \\ \lambda_F \\ \lambda_D \end{bmatrix} = \begin{bmatrix} K_r L_S K_{r^{-1}} & K_r L_{SR} \\ \frac{2}{3} L_{SR}^T K_r^{-1} & L_R \end{bmatrix} \begin{bmatrix} -i_{qds} \\ i_{QFD} \end{bmatrix}, \tag{3.14}$$

where i_{qds} is the vector of the stator currents referred to the rotor-reference frame, i.e. $i_{qds} = [i_q\ i_d\ i_0]^T$, and $i_{QfD} = [i_Q\ i_f\ i_D]^T$ is the vector of rotor currents. Considering a perfectly balanced three-phase machine, developing (3.14), and considering a nonactive field excitation voltage leads to the following set of equations:

$$\begin{aligned} \lambda_q &= -L_l i_q + L_{aq}(-i_q + i_Q), \\ \lambda_d &= -L_l i_d + L_{ad}(-i_d + i_D + i_F), \\ \lambda_Q &= L_{lQ} i_Q + L_{aq}(-i_q + i_Q), \\ \lambda_F &= L_{lF} i_F + L_{ad}(-i_d + i_F + i_D), \\ \lambda_D &= L_{lD} i_D + L_{ad}(-i_d + i_F + i_D), \end{aligned} \tag{3.15}$$

this set of equations is useful in the process of obtaining circuit parameters (inductances and resistances) used in control design from the parameters usually given by manufactures (operational inductances), as is shown in Section 3.2.8. This set is also useful in the development of flux and magnetic saturation estimators, shown in Section 3.3.4.

3.2.6 Voltage Equations in the Rotor Reference Frame

The voltage equations given in the rotor reference frame are usually given as the following set [82]:

$$\begin{aligned} v_q &= -r_s i_q + \omega_r \lambda_d + p\lambda_{qs}, \\ v_d &= -r_s i_d - \omega_r \lambda_q + p\lambda_{ds}, \\ v_Q &= r_Q i_Q + p\lambda_Q, \\ v_F &= r_F i_F + p\lambda_F, \\ v_D &= r_D i_d + p\lambda D. \end{aligned} \tag{3.16}$$

3.2.7 Torque Equation in the Rotor Reference Frame

It can be shown that the electrical torque equation in the rotor-reference frame is given as [85], [86]:

$$T_e = \frac{3}{2}(\lambda_d i_q - \lambda_q i_d). \tag{3.17}$$

This formulation is considerably simpler than the one previously presented and will allow the development of relatively simple torque control. It is important to observe that the variables λ_q and λ_d are the rotor-reference frame components of the stator flux. There are others ways of representing (3.17), namely using the air-gap flux components [85].

3.2.8 Equivalent Circuits and Operational Impedances

Synchronous machine electrical data is usually supplied by manufacturers in the form of time constants, synchronous reactances, transient reactances and subtransient reactances. The development shown until now has been given in terms of inductances, these quantities possess the same values when given in per-unit [87]. The flux equations (3.15) can also be presented in terms of reactances X and flux linkages per second ϕ [82]:

$$\begin{aligned} \phi_q &= -X_l i_q + X_{aq}(-i_q + i_Q) \\ \phi_d &= -X_l i_d + X_{ad}(-i_d + i_D + i_F) \\ \phi_Q &= X_{lQ} i_Q + X_{aq}(-i_q + i_Q) \\ \phi_F &= X_{lF} i_F + X_{ad}(-i_d + i_F + i_D) \\ \phi_D &= X_{lD} i_D + X_{ad}(-i_d + i_F + i_D). \end{aligned} \tag{3.18}$$

That being said, the development of control systems shown throughout this work will employ inductances (L) and flux linkages (λ), using appropriate per-unit systems.

Stator flux components can be written as function of field voltages and rotor

currents, as shown in Section 3.2.5. The relationships previously presented between fluxes, rotor currents, and rotor voltages in a machine model with a single damper winding on each axis is often depicted through the equivalent circuits shown in Figure 3.2 [82] [88]. It is important to observe that a new quantity representing the field excitation voltage, V_F, has been added. The equations given previously considered a null field excitation voltage, that is, $V_F = 0$.

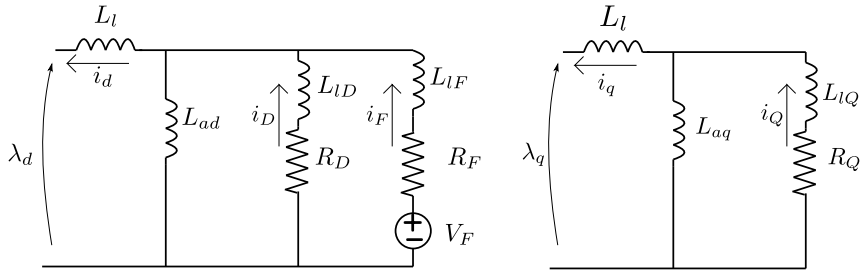

Figure 3.2: Equivalent circuits representing the 2.1 synchronous machine model.

These circuit representations are useful in the control design presented in Chapter 6. The inductances and resistances present in these circuits can be obtained from manipulations of the manufacturer data given in the form of operational impedances and time constants [79].

Operational impedances are transfer functions describing the relationship between rotor currents and stator flux linkages per second [76]. They are given by the form:

$$\phi_{q,d} = X_{q,d}(s)\, i_{q,d}. \tag{3.19}$$

As previously stated, this is equivalent, in per-unit, to:

$$\lambda_{q,d} = L_{q,d}(s)\, i_{q,d}. \tag{3.20}$$

Now the development of synchronous, transient, and subtransient inductances is presented for the quadrature and direct axes.

Quadrature-axis Operational Inductance

The operational inductance in the q-axis is given by:

$$\lambda_q = L_q(s)\, i_q, \tag{3.21}$$

it is possible to write $L_q(s)$ as the transfer function (3.22)

$$L_q(s) = L_q \frac{(1 + sT_q'')}{(1 + sT_{qo}'')}. \tag{3.22}$$

The $L_q = L_l + L_{aq}$ quantity is the q-axis synchronous inductance. The time constants T_q'' and T_{qo}'' are related to the circuit elements shown in Figure 3.2 by:

$$\begin{aligned} T_q'' = \ (L_{lQ} + \frac{L_l L_{aq}}{L_l + L_{aq}}) \frac{1}{R_Q} = (L_{lQ} + \frac{L_l L_{aq}}{L_q}) \frac{1}{R_Q}, \\ T_{qo}'' = \frac{L_{aq} + L_{lQ}}{R_Q}. \end{aligned} \tag{3.23}$$

Synchronous, transient and subtransient inductances are approximations for the response of $L_q(s)$ to phenomena with different dynamic behaviors. The operational impedances response to steady-state operation is defined as the synchronous inductance L_q [76]:

$$L_q = L_q(s)|_{s=0} = L_l + L_{aq}. \tag{3.24}$$

Observing the circuit in Figure 3.2 it becomes clear that (3.24) is equivalent to opening the rotor circuit damper winding.

In this model, the other behavior region for the q-axis is to consider the response of the electrical machine to fast references and define $L_q^{''}$, the subtransient inductance [82]:

$$L_q^{''} = L_q(s)|_{s=\infty} = L_l + \frac{L_{aq} L_{lQ}}{L_{aq} + L_{lQ}}. \tag{3.25}$$

In terms of the equivalent circuit, this quantity is equivalent to taking every damper winding into account.

Direct-axis Operational Inductance

The d-axis component of stator flux λ_d is, just like in the q-axis case, a function of the respective operational inductance $L_d(s)$ and stator current i_d:

$$\lambda_d = -L_d(s)\, i_d \tag{3.26}$$

it is possible to approximate $L_d(s)$ in terms of the transfer function:

$$L_d(s) = L_d \frac{(1 + sT_d')(1 + sT_d'')}{(1 + sT_{do}')(1 + sT_{do}'')}. \tag{3.27}$$

the d-axis time constants are given by:

$$\begin{aligned} T'_{do} &= \frac{L_{lF} + L_{ad}}{R_F}, \\ T''_{do} &= \frac{1}{R_D}(L_{lD} + \frac{L_{lF}L_{ad}}{L_{lF} + L_{ad}}), \\ T'_{d} &= \frac{1}{R_F}(L_{lF} + \frac{L_{ad}L_{l}}{L_{l} + L_{ad}}), \\ T''_{d} &= \frac{1}{R_D}(L_{lD} + \frac{L_{ad}L_{ld}L_{lF}}{L_{lF}L_{ad} + L_{lF}L_{l} + L_{l}L_{ad}}). \end{aligned} \tag{3.28}$$

Similarly to the q-axis case, the synchronous d-axis inductance is given by:

$$L_d = L_d(s)|_{s=0} = L_l + L_{ad} \tag{3.29}$$

and the subtransient d-axis inductance is [82]:

$$L''_d = L_d(s)|_{s=\infty} = L_l + \frac{L_{ad}L_{lF}L_{lD}}{L_{ad}L_{lF} + L_{ad}L_{lD} + L_{lF}L_{lD}} \tag{3.30}$$

just like in the q-axis case, that amounts to taking into account every damper winding branch in Figure 3.2. Unlike the q-axis though, the d-axis circuit has, in this model, two branches portraying the rotor behavior. A transient inductance is, thus, defined as an intermediate behavior between synchronous and subtransient responses. This is defined by switching off the d-axis damping circuit [82] [83], resulting in:

$$L'_d = L_d(s)|_{s=\infty} = L_l + \frac{L_{ad}L_{lF}}{L_{ad} + L_{lF}}. \tag{3.31}$$

Equations (3.23), (3.24), (3.25), (3.28) (3.29), (3.30) and (3.31)present a relationship between the usual datasheet values and the circuit resistances and inductances values that are actually used to design the electrical drive control systems.

Obtaining Circuit Variables from Operational Impedances

From the time constants, synchronous, transient and sub-transient inductances, values for the circuit quantities are obtained as follows for the q-axis [83]:

$$\begin{aligned} r_Q &= \frac{L_q}{T''_{qo}}, \\ Ll_Q &= \frac{L_q}{T''_{qo}}, \end{aligned} \tag{3.32}$$

and for the d-axis:

$$\begin{aligned} r_D =& \frac{L_{lD} + \frac{L_{lF}L_{ad}}{L_{lF}+L_{ad}}}{T''_d} \frac{L''_d}{L'_d}, \\ Ll_D =& \frac{L''_d L_{ad} L_{lF} - L_l L_{ad} L_{lF}}{L_l L_{lF} + L_l L_{ad} + L_{ad} L_{lF} - L''_d L_{lF} - L''_d L_{ad}}, \\ Ll_F =& \frac{L_{ad}(L'_d - L_l)}{L_d - L'_d}, \\ R_F =& \frac{L_{lF} + L_{ad}}{T'_{do}}. \end{aligned} \tag{3.33}$$

3.2.9 Machine Saturation

So far the whole model has been done disregarding magnetic saturation effects. Models of salient-pole synchronous machines implemented in simulation software like PSCAD/EMTDC usually only take into account magnetic saturation in the d-axis. Leakage inductances are considered to be constant and magnetizing inductances vary as function of magnetizing current $i_m = i_F - i_d + i_D$. Figure 3.2 is now redrawn presenting not only the stator flux linkages but also the air-gap flux linkages $\lambda_{ad,aq}$:

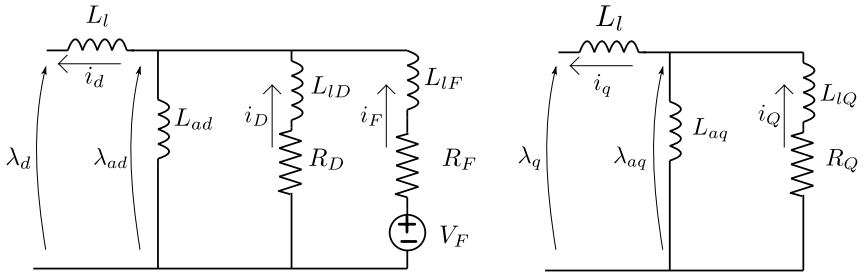

Figure 3.3: Equivalent circuits representing the 1d1q synchronous machine model with the variables related to magnetization.

These circuits show that the air-gap flux linkages differ from the stator-flux linkages previously presented in (3.15). They are represented by the following set of equations:

$$\begin{aligned} \lambda_{ad} =& (i_D + i_F - i_d)(L_{ad}), \\ \lambda_{aq} =& (i_Q - i_q)(L_{aq}). \end{aligned} \tag{3.34}$$

Figure 3.4 illustrates a typical d-axis saturation, based on data from a currently operational synchronous machine in the Brazilian power system, and the variation of magnetizing inductance L_{ad} as function of the operating point in the non-linear magnetizing curve [89] [90]. In this usual model, hysteresis is not taken into account [90].

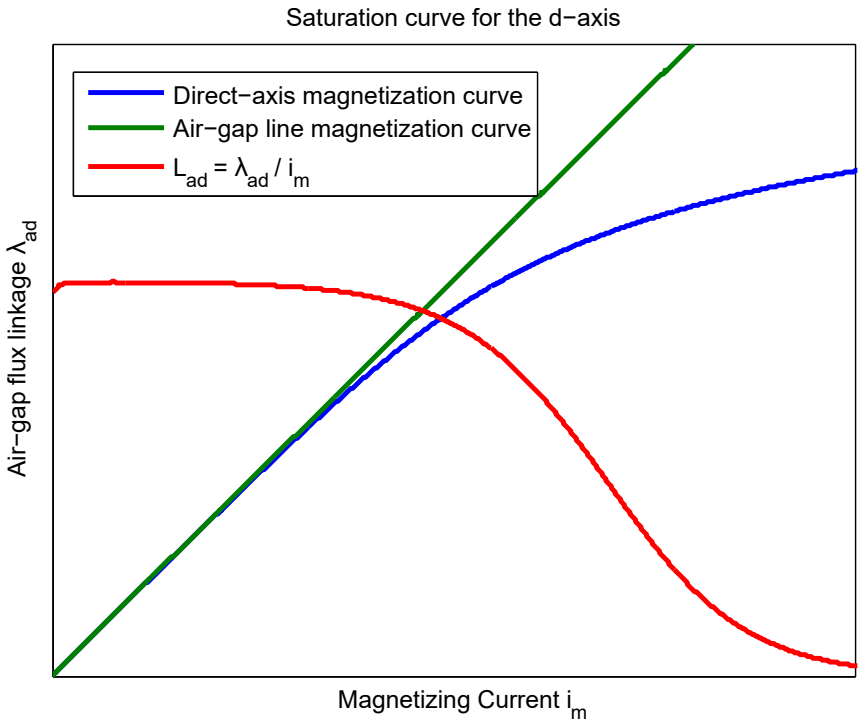

Figure 3.4: Typical saturation behavior of synchronous machine models and magnetizing branch inductance variation.

This is a typical curve for the variation of L_{ad} [83] [90]. There is a way of deriving this curve using the electrical drive itself. That is, the drive performs a saturation scan before the operation commences and, with this information, implements a saturation estimator [83]. This saturation estimator is explained in Section 3.3.3.

Magnetization curves as presented by manufacturers usually have the field winding current on the horizontal axis and the RMS terminal voltage on the vertical axis, and, from that curve, it is possible to obtain variables related to per-unit quantities, as is shown in Chapter 6.

3.3 Vector Control of a Wound-Rotor Synchronous Machine

3.3.1 Introduction to AC Machines Vector Control

In multiple applications, it is desirable to quickly and precisely control the electric torque developed by an electrical machine. Historically, this kind of high-dynamics control has been implemented with relative easy on dc machines, specially the ones with separate excitation, where the developed torque is proportional to the simple product between a flux-producing current and a torque-producing current. Torque production on ac machines can be understood in the same manner: as the product of two currents, or, as the interaction between a flux (generated by the flux-generating current) and a current. This unified understanding of electric torque production among dc and ac machines only took place in the 1970s, with the works of Blaschke, Haase, and Leonhard [83] [85]. This line of work has shown that, with appropriate reference frames, the torque equations for electric machines could be written in simplified forms, similar to those of dc machines. As this control technique requires the use of reference frames which, usually, follow a specific flux linkage, these techniques are sometimes called Field-Oriented Control (FOC) [83] or, as they are based on the control of the spatial angle between physical quantities and not only their modulus, they are also known as Vector Control [85].

Vector control can be developed in a relatively simple manner for electrically excited (and permanent-magnet) synchronous machines. Its development begins with the fundamental torque equation, (3.17):

$$T_e = \frac{3}{2}(\lambda_d i_q - \lambda_q i_d).$$

This equation has, at first, been presented as done by Krause [82], i.e. as a consequence of applying the rotor-reference frame transformation to the torque equation written in the machine-reference variables (3.17). In the light of vector control, this equation can be understood as the vector product of the stator-flux linkage space vector λ_s and the stator current space vector i_s [85]:

$$T_e = \frac{3}{2}(\lambda_s \times i_s). \tag{3.35}$$

Equation (3.35) shows that torque is maximized if the angle between stator flux and stator current space vectors are kept as close as possible to 90^o degrees. This gives rise to one possible vector-control technique implementation known as the stator flux oriented control, where the reference frame is set to follow the stator flux linkage (see, for example, [83] or [91]). There are other possible implementations [80] [85],

depending upon which reference is chosen. For example, (3.35) can be rewritten in terms of the air-gap flux linkage and this quantity can be chosen as the reference, giving rise to air-gap flux oriented control (e.g. [85]). These techniques have been historically, for example with the work of Blaschke, developed with induction machines in mind [83] [92]. Vector control is, however, a general concept applicable to any ac machine.

Further understanding about torque production in salient-pole synchronous machines can be obtained by rewriting (3.17) employing the relationships between stator fluxes and currents previously estabilished by (3.15):

$$\begin{aligned}\lambda_d &= -L_l i_d + L_{ad}(-i_d + i_D + i_F)\\ \lambda_q &= -L_l i_q + L_{aq}(-i_q + i_Q)\end{aligned}$$

substituting the d-q axes stator fluxes from (3.15) into (3.17) yields:

$$T_e = \frac{3}{2}\left[(-L_l i_d + L_{ad}(-i_d + i_D + i_F))i_q - (-L_l i_q + L_{aq}(-i_q + i_Q))\, i_d\right]. \tag{3.36}$$

Identifying $\lambda_{aF} = L_{ad} i_F$ as the contribution of the field-winding for the air-gap flux linkage:

$$T_e = \frac{3}{2}\left[\underbrace{(L_d - L_q) i_q i_d}_{R} + \underbrace{\lambda_{aF} i_q}_{S} + \underbrace{L_{ad} i_D i_q - L_{aq} i_Q i_d}_{D}\right] \tag{3.37}$$

where R, S and D mark the terms related to, respectively, the saliency (or reluctance) torque, excitation torque, and induction machine (or damper) torque [80] [85]. Damper winding currents are usually disregarded, leading to:

$$T_e = \frac{3}{2}\left[(L_d - L_q) i_q i_d + \lambda_{aF} i_q\right]. \tag{3.38}$$

As previously stated, vector control of ac machines is dependent on torque formulations which are a product of flux-producing currents with torque producing currents, both in space quadrature [85]. Equation 3.38 shows precisely this behavior for the excitation torque, where the flux producing current is i_F, giving rise to λ_{aF}, and i_q is the quadrature torque-producing currents. As the field winding is fixed to the d-axis, both currents are in quadrature. The first term could simply be eliminated by setting $i_d = 0$, in what is known as the Zero Direct-current Control (ZDC) and that would be already enough to employ some form of vector control to an electrically excited synchronous machine. However, there is a more advantageous option, related to the minimization of stator current, which is known as Maximum Torque per Ampere (MTPA) operation [78]. This technique will allow for the optimal use of reluctance torque in the salient-pole synchronous machine.

3.3.2 Stator Current References based on Maximum Torque per Ampere Operation

A desirable way of controlling electrical machines is to precisely and quickly control torque while maintaining stator current values as small as possible. The vector control technique which enables this is sometimes called the Maximum Torque per Ampere (MTPA) technique. For non-salient rotor machines there is no reluctance torque and, therefore, this is trivially achieved by setting $i_d = 0$. For salient pole rotor machines this must be achieved differently. Wu [78] presents this technique in a relatively straightforward way for salient-pole permanent-magnet synchronous machines and alternatives for electrically excited synchronous machines are presented in other works [83] [85].

Equation (3.38) shows that a certain electric torque might happen in different (i_d, i_q) points [78]. To illustrate this, an example of a synchronous machine with $L_d = 1.25, L_q = 0.7$ and $\lambda_{aF} = 1.0$ is presented. Figure 3.5 shows a contour plot of torque as function of d,q axis stator currents.

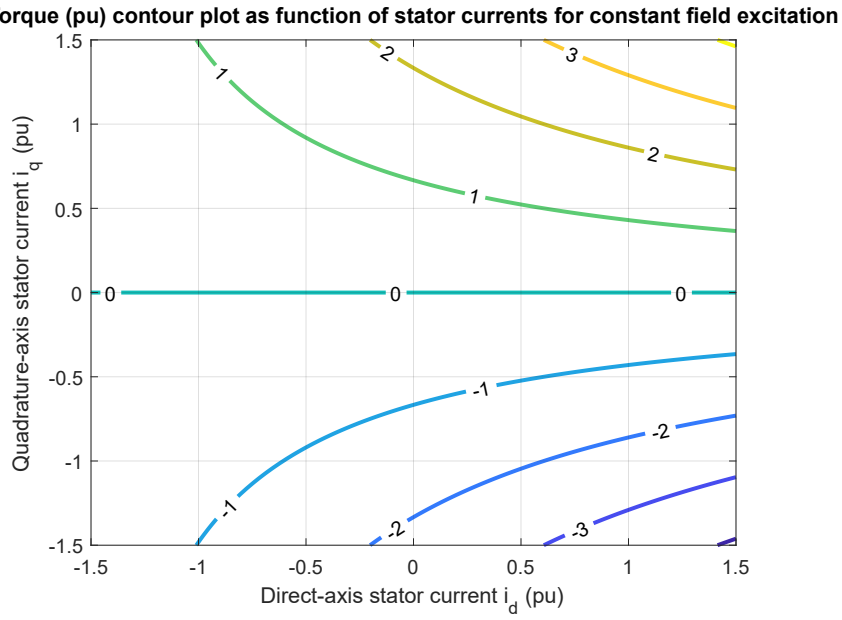

Figure 3.5: Contour plot of developed torque for $L_d = 1.25, L_q = 0.7, \lambda_{aF} = 1.0$.

Clearly there are infinite points on the i_d, i_q plane leading to the same torque. To further expand on this point, now only the unitary torque curve is kept and the contour plot for the modulus of the stator current is superimposed to it. The result is shown in Figure 3.6.

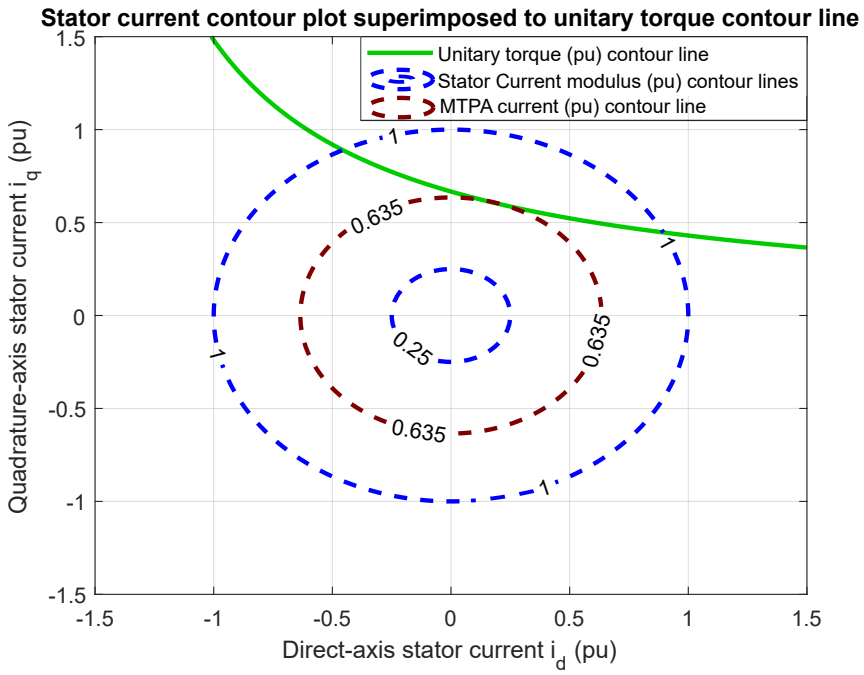

Figure 3.6: Superimposed stator current and unitary torque contour lines, clearly there is an optimal operation point on the i_d, i_q plane.

Figure 3.6 shows that there is a single operating point which minimizes the modulus of the stator current. The objective of MTPA operation is to somehow compute this point in real-time.

Electrical torque can be written as the vector product between stator-flux linkage and stator currents, as shown by (3.35). Therefore, (3.35) is maximized when the space vectors of these two quantities are in quadrature. Thus, to obtain optimum references for i_d and i_q the following procedure is followed in this dissertation. First, the modulus of the stator flux space vector is obtained:

$$|\lambda_s| = \sqrt{\lambda_d^2 + \lambda_q^2} \tag{3.39}$$

λ_d and λ_d are estimated as shown in Section 3.3.4. The angle between the stator flux space vector and the machine rotor is given by:

$$\delta_{\lambda_s} = \arctan\left(\frac{\lambda_q}{\lambda_d}\right) \tag{3.40}$$

as the objective is to keep i_s and λ_s in quadrature, the modulus of $i_{s\,ref}$ is given by, via (3.35):

$$|i_{s\,ref}| = \frac{2}{3}\frac{T_{e\,ref}}{|\lambda_s|} \tag{3.41}$$

and the references for the rotor-reference frame current axis components are given

by:

$$\begin{aligned} i_{d\,ref} &= |i_{s\,ref}| \cos\left(\delta_{\lambda_s} + \frac{\pi}{2}\right) \\ i_{q\,ref} &= |i_{s\,ref}| \sin\left(\delta_{\lambda_s} + \frac{\pi}{2}\right). \end{aligned} \tag{3.42}$$

The process explained in this Subsection is represented as the MTPA block in Figure 3.8, shown at Subsection 3.3.5.

3.3.3 Magnetic Saturation Estimation

As previously shown in Section 3.2.9, the machine saturation is modeled exclusively for the d-axis and is considered to be a variation on the value of L_{ad}. As shown by Pyrhönen et al. [83], a possible way of obtaining a curve for the L_{ad} variation is to take advantage of the electrical drive and control the variables in such a way as to calculate L_{ad} as function of magnetizing current. This is done by setting $i_d = 0$, maintaining i_q with a constant value, varying i_F, and measuring the electrical torque. Doing this process and then employing (3.38) for each i_F value allows to obtain the curve relating L_{ad} and the magnetizing current.

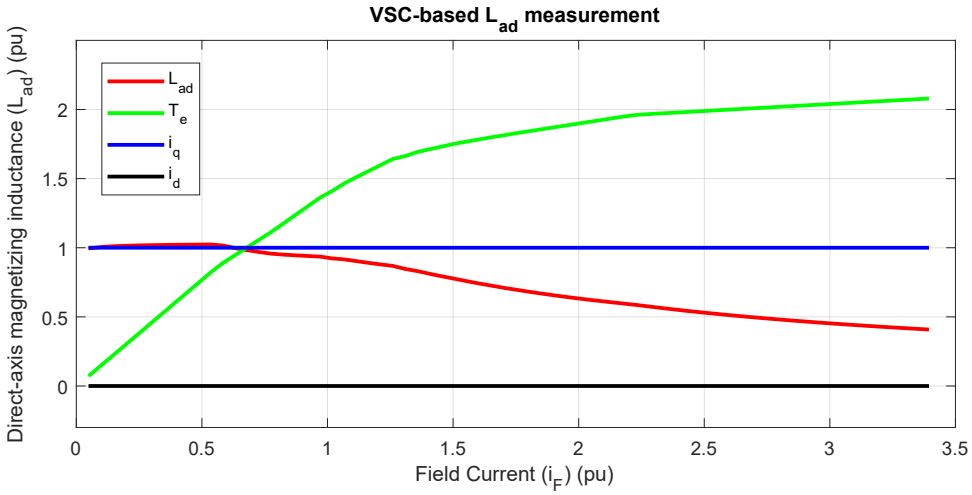

Figure 3.7: Result of the L_{ad} measurement using the VSC-based electrical drive.

It can be observed that the L_{ad} curve obtained follows the same general form of the one shown in Figure 3.4, based directly on machine data. With the set of points describing this curve, it is possible to then build a look-up table which receives $i_m = i_F - i_d$ and returns L_{ad}, as depicted in Figure 3.8. This estimation procedure is necessary to estimate the machine flux linkages, as will be seen in the next subsection.

3.3.4 Air-gap and Stator Flux Linkages Estimator

As the stator current references are based upon stator flux, it could seem, at first, that there would be no need to estimate or control air-gap flux linkage. The motivation for this estimation comes from the fact that a stiff air-gap flux linkage leads to better dynamic performance of the synchronous machine, effectively counterbalancing damper winding currents. This strategy is known as reaction control [83]. It would be possible to simply keep a constant i_F order and control the machine that way, although with inferior dynamic performance [83].

There is a coupling between direct axis and quadrature axis voltage equations, which is proportional to stator flux quantities, as can be seen in Equation (3.16). The stator-flux linkage is, therefore, not only necessary to obtain the stator-current references, as previously shown, but is also necessary to decouple axes equations in current control.

In this work, the vector control strategy employs nested direct-axis air-gap flux linkage and field current control loops. While field current can be measured, air-gap flux linkage must be estimated and, as seen in (3.36), is a function of not only measurable currents i_q, i_F and i_d, but also of the unmeasurable damper winding currents i_Q and i_D. Therefore, it is necessary to estimate these damper currents. This can be done through the following set of equations for the d-axis [83]:

$$\begin{aligned} i_D &= (K_{td} i_d + K_{tf} i_F)\left(\frac{1}{\tau_{rD} s + 1} - 1\right), \\ K_{td} &= \frac{L_{ad}}{L_{ad} + L_l + L_{lD}}, \\ K_{tf} &= \frac{L_{ad} + L_l}{L_{ad} + L_l + L_{lD}}, \\ \tau_{rD} &= \frac{L_{ad} + L_l + L_{lD}}{r_D}, \end{aligned} \tag{3.43}$$

and the following set for the q-axis:

$$\begin{aligned} i_Q &= K_{tq} i_q \left(\frac{1}{\tau_{rQ} s + 1} - 1\right), \\ K_{tq} &= \frac{L_{aq}}{L_{aq} + L_l}, \\ \tau_{rQ} &= \frac{L_{aq} + L_l}{r_Q}. \end{aligned} \tag{3.44}$$

With both damper circuits currents and L_{ad} (Section 3.3.3) estimated, the air-gap and stator flux components can be estimated using (3.36).

3.3.5 Employed Vector Control Strategy

Figure 3.8 shows how the control fundamental blocks are set together in the vector control employed in this work. The way in which the control loops are designed is presented in Chapter 6.

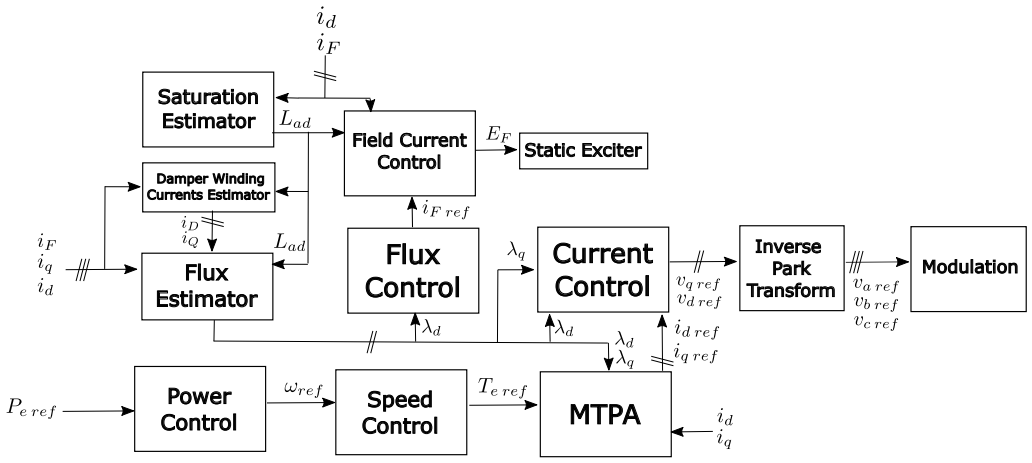

Figure 3.8: Simplified view of the proposed vector control strategy.

3.4 Modeling and Control of Modular Multilevel Converters

3.4.1 Introduction to the Modular Multilevel Converter

The Two-Level Voltage-Sourced Converter (2L-VSC) is the kind of power electronics converter most commonly connected to ac power grids given its relative simple modulation, low cost and multiple advantages over the previously dominant Current Sourced Converters (CSC) . In applications requiring dc-side voltages above 2 kV, though, this topology becomes less interesting. This is the case because there are no power semiconductors capable of blocking voltages above certain levels and the series connection of such forced commutation semiconductor switches is still an open problem in terms of technological difficulties in equalizing the switches characteristics for reliable valve build-up. Even if this difficulty were to be overcome, the switching of high-voltages would be associated with insulation stresses and large switching power losses. The solution for the application of VSC for high voltages and powers came in the form of multilevel topologies, specially in the form of the Modular Multilevel Converter, where the pole-to-pole voltage is divided between multiple semiconductor switches by using the concept of submodule (SM) , with no necessity for series connections [57] [93] . The MMC, depicted in Figure 3.9, not only eliminates the problems previously cited, but also presents other advantages. The

submodule-based construction leads to minimization of problems related to electromagnetic interference (EMI), superior reliability and its multiple voltage levels considerably reduce the harmonic frequencies injection, leading to smaller ac-filters, or to their complete absence [60] [94].

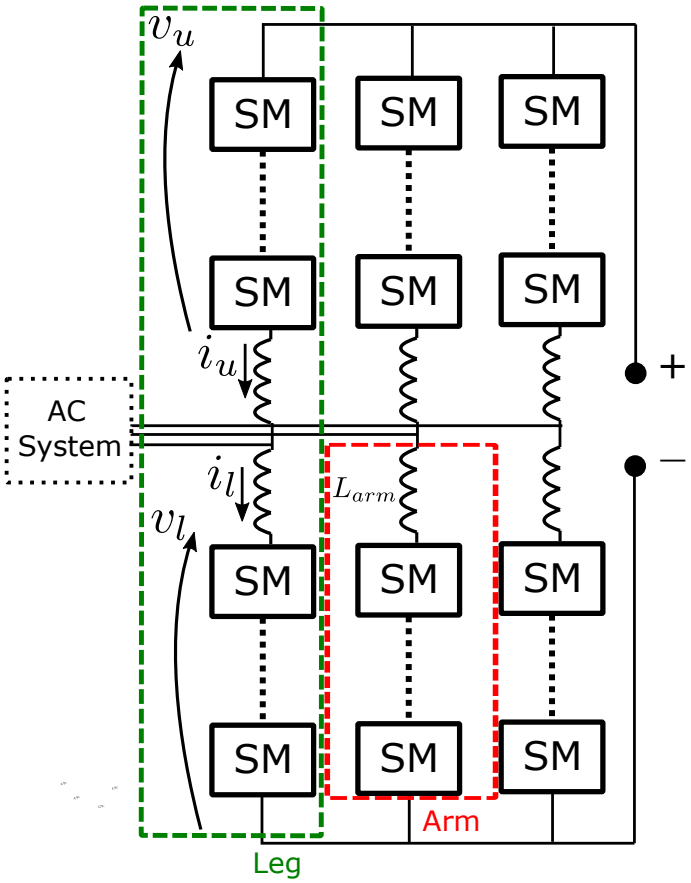

Figure 3.9: Topology of the Modular Multilevel Converter.

There are, conceptually, multiple topologies for the submodules shown in Figure 3.9. In most practical applications though, only two of them are applied, these are the half-bridge and full-bridge submodules.

Half-bridge submodules are based on the circuit shown in Figure 3.10. This type of submodule has the main advantage of, amongst the possible submodule configurations, being the one with the lowest loss levels, requirements of volume, and cost. Its main drawback is the impossibility of producing negative v_{out} voltages. A MMC built using this sort of submodule is sensitive to dc-side faults and, as of 2020, requires the actuation of ac-side circuit breakers in these cases. This will remain to be the case until the on-going developments towards dc-side circuit breakers are complete. Most of the operating MMCs in the world are built with this kind of submodule, as most HVdc links dc-sides are based on underground (or submarine) cables [60]. This work will focus on this topology.

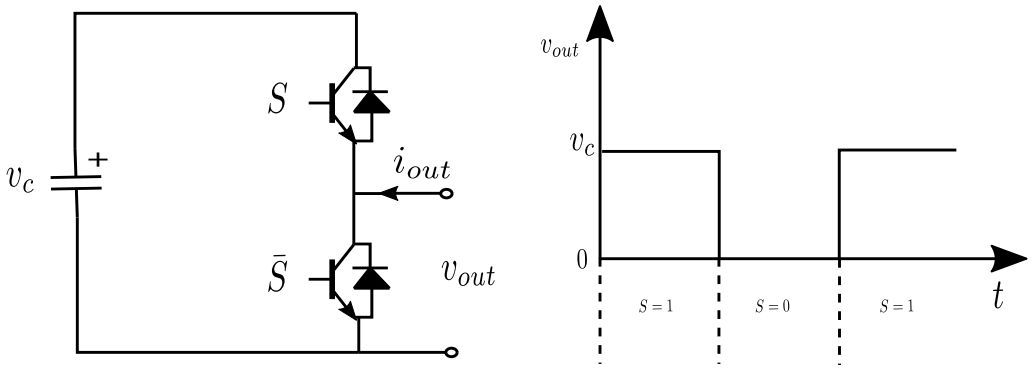

Figure 3.10: Topology of the half-bridge submodule and its external voltage as function of switch positions.

3.4.2 Mathematical Modeling

The MMC can be described as a system with four state-variables per phase, each of these will be described throughout this subsection. The modeling presented here is valid for a MMC with M phases and, with that in mind, Figure 3.9 is redrawn in a single-phase visualization, as shown in Figure 3.11. The MMC considered here is built with half-bridge submodules and that v_u and v_l voltages can have dc and ac components. At this first exposition the total absence of common-mode voltages (CMV) is assumed.

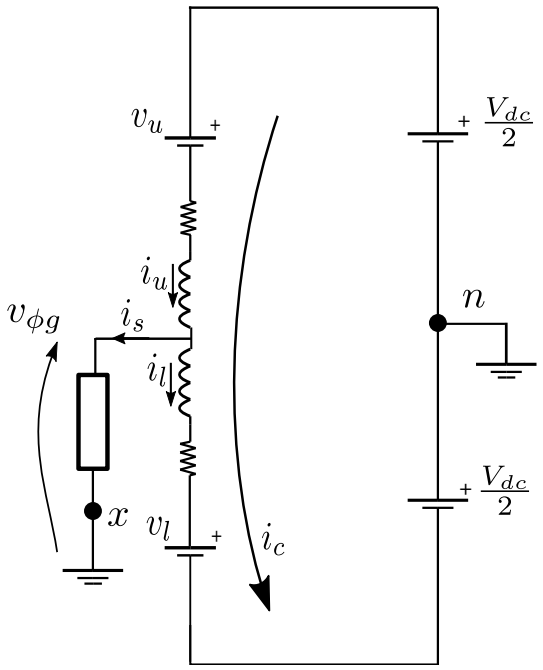

Figure 3.11: Single-phase MMC.

From inspection of Figure 3.11, the relation between the arm currents (i_u, i_l) and the phase current i_s can be written as:

$$i_s = i_u - i_l. \tag{3.45}$$

There is also a current (i_c) circulating through the MMC arms and not flowing to the ac grid. It contributes equally to both arms currents and, with that in mind, the pair of arm currents, i_u and i_l, can be written as function of phase current i_s and circulating current i_c:

$$\begin{aligned} i_u &= \frac{i_s}{2} + i_c \\ i_l &= -\frac{i_s}{2} + i_c. \end{aligned} \tag{3.46}$$

Manipulation of (3.46) makes it possible to reach an equation for the circulating current as function of upper and lower arm currents:

$$i_c = \frac{i_u + i_l}{2}. \tag{3.47}$$

It is important to observe that there is also a dc-side current i_{dc} and that, via KCL, a dc component must be present in the arm currents. That is, there are dc and ac components in the arm currents. Under the assumption that i_c has only dc components, the following condition for an M-phase MMC is immediate:

$$i_c = \frac{i_{dc}}{M}. \tag{3.48}$$

Of course the condition of a purely dc circulating current does not arise naturally and is, for the purpose of this initial exposition, a product of an ideal control technique which suppresses the other i_c harmonic frequencies. As will be seen later the MMC has a tendency of having circulating currents with multiple frequencies and, specially in the case of low-frequency operation of medium-voltage drives, sometimes they are not suppressed. Figure 3.12 depicts the flow of fundamental frequency ac and circulating dc currents within the three-phase MMC.

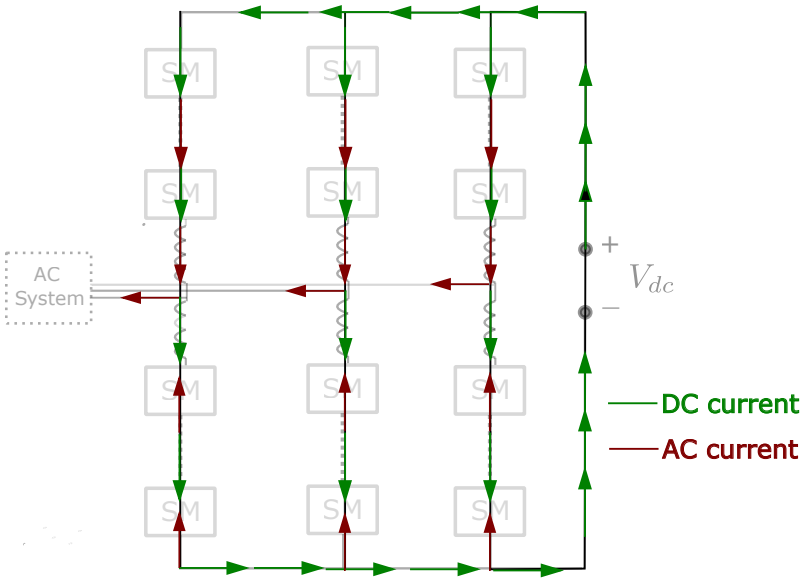

Figure 3.12: Flow of fundamental frequency and dc currents within the MMC.

As previously stated, the single-phase MMC can be represented by four state variables. By now, two of them have been presented, i_s and i_c. It is time to define its dynamical equations. Using Kirchhoff's Voltage Law (KVL) following a loop both through the upper and lower arm of the MMC of Figure 3.11 yields:

$$v_{\phi g} = \frac{V_{dc}}{2} - v_u - R\, i_u - L\frac{di_u}{dt} \tag{3.49}$$

$$v_{\phi g} = -\frac{V_{dc}}{2} + v_l + R\, i_l + L\frac{di_l}{dt}. \tag{3.50}$$

Summing (3.50) and (3.49) and remembering the definition of the phase current i_s:

$$\frac{v_l - v_u}{2} - \frac{R}{2} i_s - \frac{L}{2}\frac{di_s}{dt} = v_{\phi g} \tag{3.51}$$

now subtracting (3.50) from (3.49) and employing the definition of the circulating current i_c:

$$\frac{V_{dc}}{2} - \frac{v_l + v_u}{2} - Ri_c - L\frac{di_c}{dt} = 0. \tag{3.52}$$

Equations (3.51) and (3.52) govern, respectively, the external current and circulating current dynamics. It is noticeable that there are voltage terms in each of these equations which propel these currents. From them the phase (or differential) voltage v_s and the leg-offset voltage v_c definitions are [95]:

$$\begin{aligned} v_s &= \frac{v_l - v_u}{2} \\ v_c &= \frac{V_{dc} - v_l - v_u}{2}. \end{aligned} \tag{3.53}$$

Substituting those definitions back into (3.49) and (3.50) results in:

$$v_s - \frac{R}{2} i_s - \frac{L}{2} \frac{di_s}{dt} = v_{\phi g} \tag{3.54}$$

$$v_c - R i_c - L \frac{di_c}{dt} = 0. \tag{3.55}$$

With (3.54) and (3.55) there is a dynamics description for two of the state variables of the MMC. These two equations can be written in terms of equivalent circuits. The other state variables are related to the dynamics of v_u and v_l, which are related to the voltages of the submodules. Before expanding on this subject, the concept of averaging the MMC model is presented.

3.4.3 Averaging Principle and the Dynamics of Submodule Capacitor Voltages

We first observe that every submodule can be considered to be simply connected or disconnected and, therefore, every submodule has a boolean quantity, $n^i_{u,l}$, where the high state means the submodule is connected. It is also clear that the voltage of an arm is the sum of its individual submodule voltages $v^i_{SMu,l}$, that is:

$$v_{u,l} = \sum_{i=1}^{N} n^i_{u,l} \, v^i_{SMu,l}. \tag{3.56}$$

This equation can be made considerably simpler by taking into account the fact that, as will be shown later, the converter switching is modulated in such a way as to maintain the mean value of every SM voltage the same. With that, (3.56) can be rewritten:

$$v_{u,l} = \frac{\sum_{i=1}^{N} v^i_{SMu,l}}{N} \sum_{i=1}^{N} n^i_{u,l} \tag{3.57}$$

Further simplification can be acquired with additional considerations [57]:

- The quantity $\frac{1}{N} \sum_{i=1}^{N} n^i_{u,l}$ can be seen as a new quantity, $n_{u,l}$, which is the normalization of the amount of connected submodules in an arm. That is, a set of N boolean quantities is substituted by a single quantity varying discretely between 0 and 1, with N steps.

- There is a high enough number of submodules per arm so as to consider that $n_{u,l}$ actually varies continuously between 0 and 1.

- Submodules voltages are balanced. This way, for dynamical modeling purposes, the difference between them can be disregarded.

Taking these into account, arm voltages are written simply as:

$$v_{u,l} = n_{u,l} \sum_{i=1}^{N} v^i_{SM\,u,l}, \tag{3.58}$$

using this principle is specially advantageous taking into account that every submodule capacitor voltage is a state variable of the dynamic model, making it a model with, at least, dozens of variables. By applying the averaging principle the sum over the N capacitors of each arm becomes the state variable. With that, for a single-phase MMC, there are two equations governing the sum of the capacitors voltages:

$$\frac{C}{N}\frac{d\sum_{i=1}^{N} v^i_{SM\,u}}{dt} = n_u\,(\frac{i_s}{2} + i_c) = n_u\,i_u \tag{3.59}$$

$$\frac{C}{N}\frac{d\sum_{i=1}^{N} v^i_{SM\,l}}{dt} = n_l\,(-\frac{i_s}{2} + i_c) = n_l\,i_l \tag{3.60}$$

From the development shown above, multiple options to effectively modulate the converter arise. From the knowledge of desired leg-offset voltages and differential mode voltages, how to obtain a reference for the arm voltages?

3.4.4 Modulation Techniques

The development shown in the last subsection allows for the representation of voltages $v_{c,s}$ as function of the insertion indices, that is, as function of the number of submodules that are inserted in each arm. The insertion of submodules is, ultimately, the way by which any variable related to the MMC is controlled. By substituting (3.58) into (3.53) the following set of equations is obtained:

$$\begin{aligned} v_s &= \frac{-n_u \sum_{i=1}^{N} v^i_{SMu} + n_l \sum_{i=1}^{N} v^i_{SMl}}{2}, \\ v_c &= \frac{V_{dc} - n_u \sum_{i=1}^{N} v^i_{SMu} - n_l \sum_{i=1}^{N} v^i_{SMl}}{2}, \end{aligned} \tag{3.61}$$

algebraic manipulation leads to the insertion indices references for both upper and lower arm as function of the references for differential and leg-offset voltages [96]:

$$\begin{aligned} n_u &= \frac{\frac{V_{dc}}{2} - v_{c\,ref} - v_{s\,ref}}{\sum_{i=1}^{N} v^i_{SMu}} \\ n_l &= \frac{\frac{V_{dc}}{2} - v_{c\,ref} + v_{s\,ref}}{\sum_{i=1}^{N} v^i_{SMl}}. \end{aligned} \tag{3.62}$$

Disregarding any voltage ripple, the denominator of the right hand-side of these equations is:

$$\sum_{i=1}^{N} v_{SMu}^{i} = \sum_{i=1}^{N} v_{SMl}^{i} = V_{dc}. \tag{3.63}$$

In reality, though, there is ripple and these values actually oscillate around the average value of V_{dc}. With that, there are four ways through which $\sum_{i=1}^{N} v_{SMu,l}^{i}$ can be substituted in the MMC control [57] [96], giving rise to different index selection techniques:

- Direct Voltage Control, this strategy considers the summation of the voltages of the SM of each arm to be the average value, that is, $\sum_{i=1}^{N} v_{SMu}^{i} = \sum_{i=1}^{N} v_{SMl}^{i} = V_{dc}$.
- Closed-Loop Control, in this strategy the summation of the voltages of the SM of each arm are actually measured.
- Open-Loop Control, in this strategy the ripple in the summation of the SM voltages are estimated and added to the average value.
- Hybrid Control, this strategy considers the summation of the arm SM voltages to be the summation of the average value, V_{dc}, and of the measured ripple, obtained at the output of a band-pass filtered measurement of the summation of the SM voltages.

A comparison between these techniques is performed by Christe et al. for medium voltage drives [96]. The authors consider an averaged model of the MMC arms and disregard quantization effects, that is, consider the indices to be real numbers. It is concluded that the Direct Modulation technique requires circulating current control to become feasible but otherwise presents advantages such as good dynamic performance and relative simplicity by not requiring the estimators, energy controllers, and digital filters related to some of the other options. Furthermore, they conclude that for high-dynamics control the Closed-Loop control technique is recommended. Given the simplicity and acceptable dynamics related to Direct Modulation, this is the option chosen for the present work.

The entire discussion presented so far considers an equivalent string of arm submodules. The manner by which a certain index $n_{u,l}$ gives rise to firing signals for each submodule while maintaining the SM dc voltages balanced has not been presented. There are multiple ways by which this can be done, including individual submodule voltage control and multiple Pulse-Width Modulation (PWM) implementations [57]. As the MMC is often employed for HVdc-links, containing therefore hundreds

of submodules, it is usual to also find options with very low switching frequency such as Nearest Level Control (NLC) and Selective Harmonic Elimination PWM (SHE-PWM) being discussed in the literature.

The studied medium-voltage application applied a relatively small number of submodules, if compared with the hundreds applied in HVdc applications. In such a case, techniques with higher switching frequencies are usually necessary. The technique applied in this work employs Phase-Shifted Carrier PWM (PSC-PWM) with sorting algorithm, as also done, for example, by Darus et al. [95]. In this PWM technique there are as many carriers as there are submodules (that is, 2N); For each arm there are N carriers, time-shifted from each other by $\frac{360^o}{N}$. The carriers from the upper and lower arms can be shifted between each other or not, what affects the harmonic frequencies generated, as discussed in the literature [57] [97]. If the carriers are shifted, the scheme is known as interleaved PSC-PWM.

The Phase-Shifted Carrier PWM scheme presents beneficial points, namely, even stress distribution among semiconductors and the production of an equivalent high-switching frequency [97]. Figure 3.13 shows the basic idea of PSC-PWM, there are N carriers per arm and, in one of the possible implementations, a single reference for each arm. This reference can be further modified for each SM to guarantee SM voltage balancing. The procedure followed in this work is to use a single reference for each arm, the comparison between this reference and the carriers results in the number of submodules that should be connected in that arm, not specifying which ones. The average value of $v_{u,l}$ remains V_{dc} because of the sorting algorithm, which enforces voltage balancing, the PWM scheme controls the ac portion of these voltages. With that, the reference for internal voltage $v_{c\,ref}$ contains only ac terms and the denominators of (3.62) are set to half V_{dc} [95].

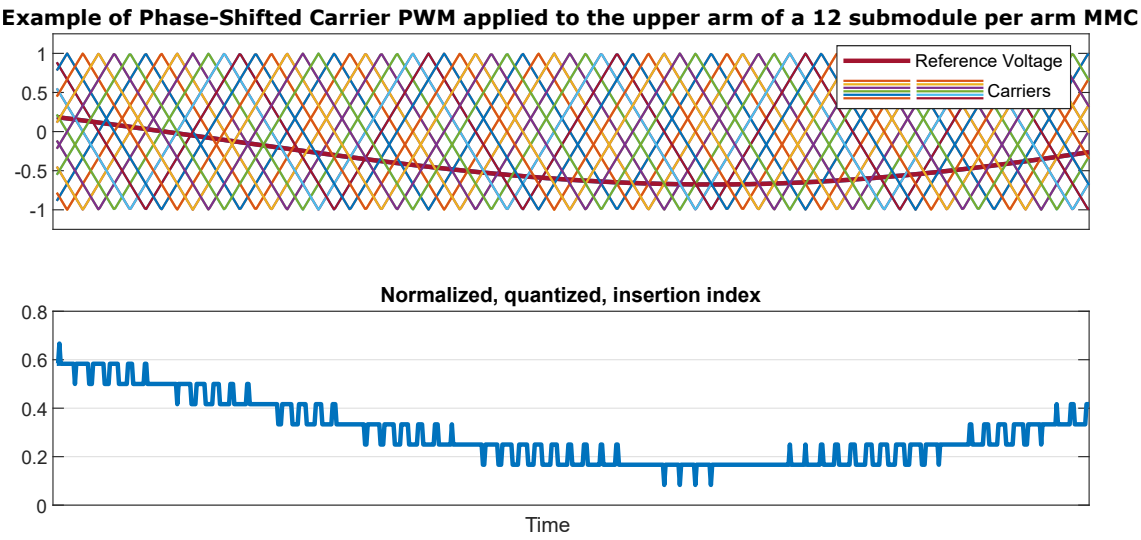

Figure 3.13: Example of upper arm modulation using phase-shifted carrier PWM.

The task of identifying which SM should be connected and ensure SM voltage balancing is given to a sorting algorithm. The sorting algorithm is a usual technique employed in MMC and is based upon the analysis of the voltage of each arm submodules and in the ordering of their voltages. With the ordered list, it is possible to choose which submodules should be connected for a certain arm current direction. This technique is depicted in Figure 3.14.

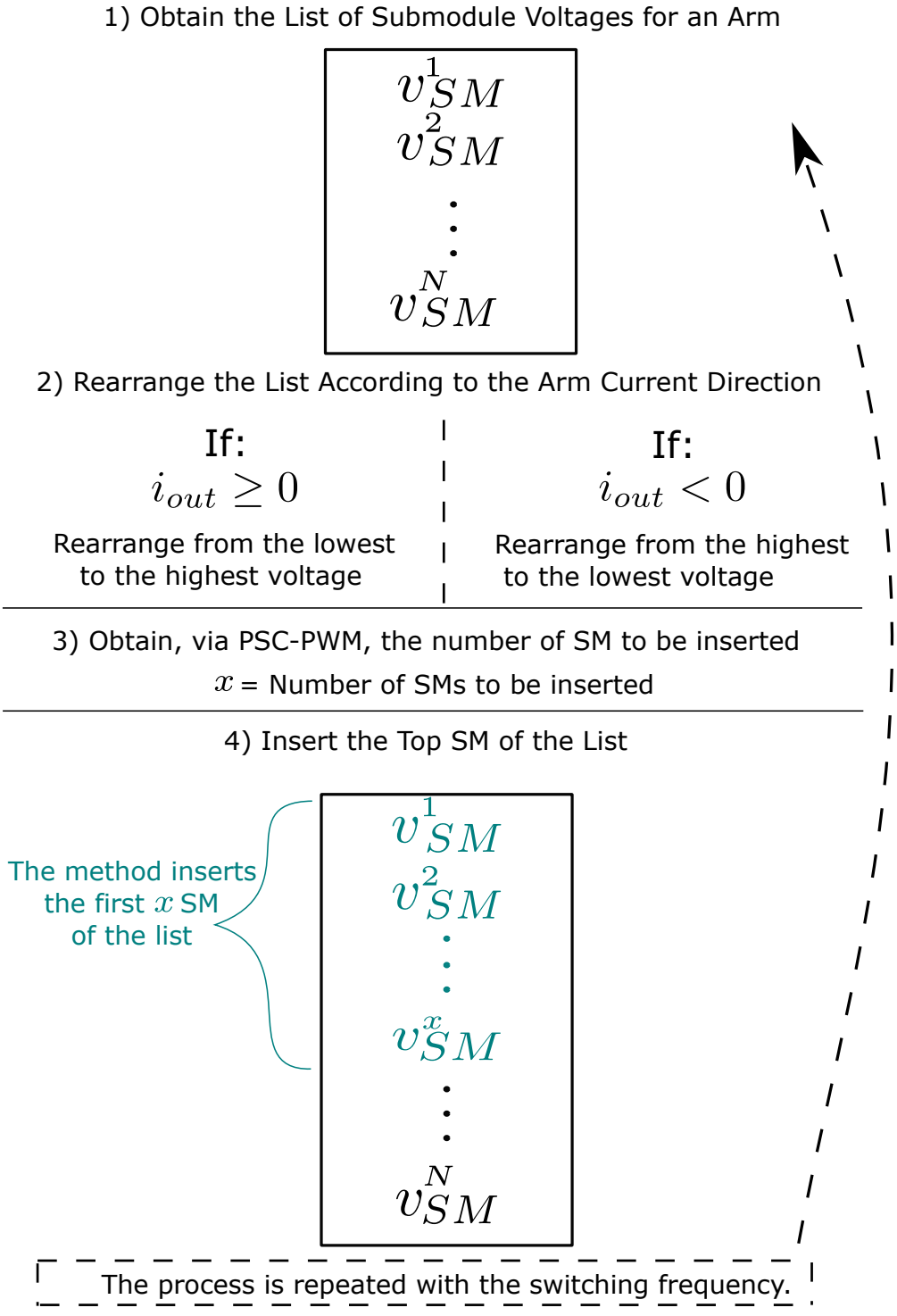

Figure 3.14: Submodule voltage sorting algorithm.

A general overview of the employed modulation scheme can be seen in Figure 3.15.

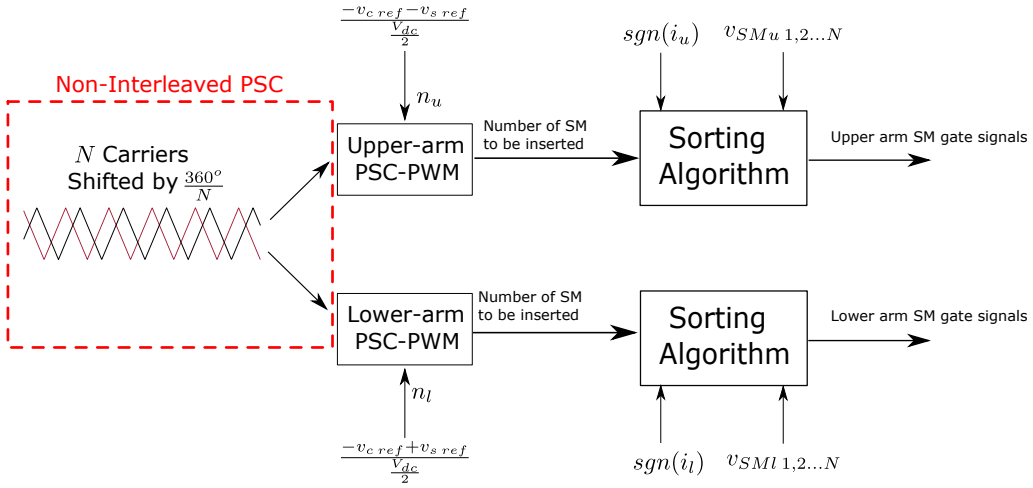

Figure 3.15: Submodule voltage sorting algorithm.

3.4.5 Circulating Currents and Capacitor-Voltage Ripple

A fundamental characteristic of the MMC is that there are unavoidable low-frequency voltage ripple in the capacitors of the submodules. This is an important difference in relation to the 2L-VSC, where there is no low-frequency ripple at the dc-bus voltage. The development presented up to this point has the assumption that there is an ideal circulating current suppression control which leaves only the unavoidable circulating dc component flowing through the arms. This assumption is now dropped and a second harmonic circulating current, which is expected to appear without Circulating Current Suppression Control (CCSC), is added. As previously discussed and shown in Figure 3.12, there are, necessarily, dc and fundamental frequency currents flowing through the arms. With the further addition of second harmonics, the $i_{u,l}$ currents in a phase of a three-phase MMC can be written as:

$$i_u = i_{s2}\sin(2\omega t + \theta) + \frac{\sqrt{2}}{2} i_s \sin(\omega t + \phi) + \frac{i_{dc}}{3} \tag{3.64}$$

$$i_l = i_{s2}\sin(2\omega t + \theta) - \frac{\sqrt{2}}{2} i_s \sin(\omega t + \phi) + \frac{i_{dc}}{3}. \tag{3.65}$$

The current passing through the SM capacitors of an arm can be defined as the product between the average switching function of the arm SM, $S_{SM\,u,l}$, and the average current passing through the arm in which the SM can be found [98].

$$i_{cap\,u,l} = S_{SMu,l}\, i_{u,l}. \tag{3.66}$$

The average switching functions have, in a general form, dc and fundamental ac frequency components, the later with amplitude S_{amp}. This comes from the form of the average insertion indices $n_{u,l}$:

$$\begin{aligned} S_{SMu} &= \frac{1}{2} - \frac{S_{amp}\sin(\omega t)}{2}, \\ S_{SMl} &= \frac{1}{2} + \frac{S_{amp}\sin(\omega t)}{2}. \end{aligned} \tag{3.67}$$

Substituting (3.64), (3.65) and (3.67) into (3.66) leads to the formulation of the average capacitor current for the upper and lower arms submodules:

$$\begin{aligned} i_{SMcap\,u} = {} & \frac{i_{dc}}{6} - \frac{\sqrt{2}S_{amp}i_s\cos(\phi)}{8} - \frac{i_{dc}}{6}S_{amp}\sin(\omega t) + \frac{\sqrt{2}i_s\sin(\omega t+\phi)}{4} \\ & -\frac{1}{4}i_{s2}S_{amp}\cos(\omega t+\theta) + \frac{\sqrt{2}i_s\cos(2\omega t+\phi)}{8} + \frac{1}{2}i_{s2}\sin(2\omega t+\theta) \\ & +\frac{1}{4}i_{s2}S_{amp}\cos(3\omega t+\theta) \\ i_{SMcap\,l} = {} & \frac{i_{dc}}{6} - \frac{\sqrt{2}S_{amp}i_s\cos(\phi)}{8} + \frac{i_{dc}}{6}S_{amp}\sin(\omega t) - \frac{\sqrt{2}i_s\sin(\omega t+\phi)}{4} \\ & +\frac{1}{4}i_{s2}S_{amp}\cos(\omega t+\theta) + \frac{\sqrt{2}i_s\cos(2\omega t+\phi)}{8} + \frac{1}{2}i_{s2}\sin(2\omega t+\theta) \\ & -\frac{1}{4}i_{s2}S_{amp}\cos(3\omega t+\theta), \end{aligned} \tag{3.68}$$

now the average SM capacitor voltage ripple at a certain frequency can be obtained by multiplying the current terms of (3.68) relative to this frequency with the corresponding capacitor impedance. The result for the fundamental frequency ripple is:

$$\begin{aligned} v_{SMcap\,u\,ripple} = {} & \frac{i_{dc}}{6\omega C_{SM}}S_{amp}\sin(\omega t) + \frac{\sqrt{2}i_s\sin(\omega t+\phi)}{4\omega C_{SM}} \\ & -\frac{1}{4\omega C_{SM}}i_{s2}S_{amp}\cos(\omega t+\theta) \\ v_{SMcap\,l\,ripple} = {} & -\frac{i_{dc}}{6\omega C_{SM}}S_{amp}\sin(\omega t) - \frac{\sqrt{2}i_s\sin(\omega t+\phi)}{4\omega C_{SM}} \\ & +\frac{1}{4\omega C_{SM}}i_{s2}S_{amp}\cos(\omega t+\theta). \end{aligned} \tag{3.69}$$

The presence of ω in the denominator of every term explains why low-frequency operation is a known challenge to the MMC. With low-frequency, the voltage ripple in each SM tends to become unacceptably high. Increased values of capacitance could help counterbalance this ripple, but at increased financial costs and converter volume. Notice that the traditional CCSC applied to the second harmonic frequency of the circulating current would not be able to nullify any term of the upper and lower arms ripples (3.69). Therefore, the conventional CCSC is not the solution

to low-frequency operation of the MMC. In fact, as shown ahead, it is the exact opposite, the techniques designed to counter this problem are based on the control of certain circulating currents frequencies and not on the classical second-harmonic suppression.

3.5 Control Technique for Low-Frequency Operation

There are multiple applications of Modular Multilevel Converters in the medium-voltage range. Some examples are Flexible-ac Transmission System (FACTS) devices [99] and Medium-Voltage direct-current (MVdc) grids [100]. In the beginning of the 2010 decade, the first works regarding MMCs applied to transformerless medium-voltage drives are published and the possible difficulties of low-frequency operation are identified (e.g. [101]).

A set of papers have been published proposing techniques for the operation of the MMC under low-frequencies without torque limitations. These techniques are usually based, fundamentally, on understanding the power oscillations that happen within the converter and to damp these oscillations through the control of two variables: the circulating currents and the common-mode voltage [102]. This work applies the technique proposed by Jung et al. [103] [104] and compares the application of different waveforms as common-mode voltage. The exposition of the technique begins with Figure 3.16, where the ac-side neutral bus x is not grounded, so that it is possible to measure a common-mode voltage between this bus and the neutral bus, n.

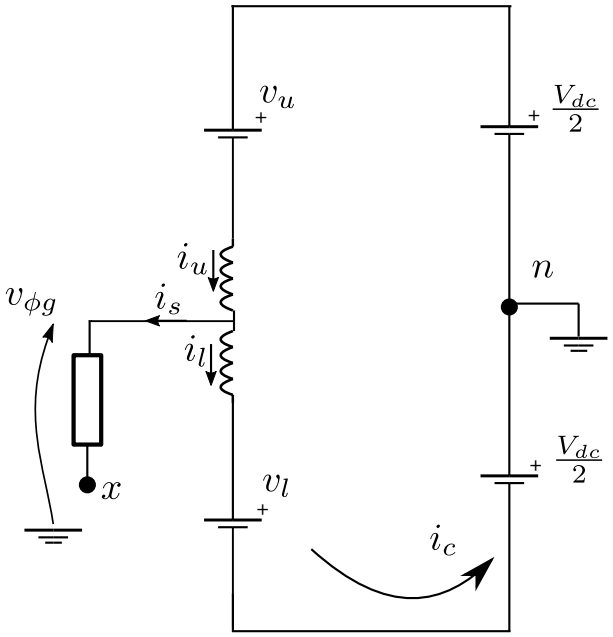

Figure 3.16: MMC single-phase equivalent with neutral points ©2020 IEEE. Reproduced from [67].

Adding the contribution from the common-mode voltage v_{xn} into the arm voltages given by (3.62), substituting (3.58) and algebraically manipulating the result yields (3.70).

$$\begin{aligned} v_u &= \frac{V_{dc}}{2} - v_{c\,ref} - v_{s\,ref} - v_{xn}, \\ v_l &= \frac{V_{dc}}{2} - v_{c\,ref} + v_{s\,ref} + v_{xn}. \end{aligned} \tag{3.70}$$

With the definitions of v_u and v_l, it is possible to write the power flowing through each arm as:

$$\begin{aligned} p_u = v_u i_u &= \left(\frac{V_{dc}}{2} - v_{s\,ref} - v_{xn} - v_{c\,ref}\right)\left(\frac{i_s}{2} + i_c\right), \\ p_l = v_l i_l &= \left(\frac{V_{dc}}{2} + v_{s\,ref} + v_{xn} - v_{c\,ref}\right)\left(\frac{-i_s}{2} + i_c\right). \end{aligned} \tag{3.71}$$

A source of voltage ripple is the power exchange between upper and lower arms from a same MMC leg. This difference is, from (3.71), given by:

$$p_u - p_l = \frac{V_{dc} i_s}{2} - 2v_{s\,ref} i_c - 2v_{xn} i_c - v_{c\,ref} i_s. \tag{3.72}$$

When the MMC is supplying external low-frequency currents, the two first right hand-side terms will have a large amount of low-frequency components, leading to low-frequency energy exchange, and consequently, to energy unbalance. There are terms which are dependent upon the common-mode voltage, which does not affect the output current of the MMC. This fact brings an extra degree of freedom to

the converter. The same logic is valid for the circulating current i_c. The high and low-frequency components of these variables are identified, respectively, by the superscripts HF and LF:

$$\begin{aligned} v_{xn} &= v_{xn}^{HF}, \\ i_c &= i_c^{LF} + i_c^{HF}, \end{aligned} \tag{3.73}$$

and (3.72) is rewritten with only the low-frequency terms. This equation should be nullified via control action, as these low-frequency components will lead to a high energy unbalance between arms:

$$p_u - p_l|^{LF} = \frac{V_{dc} i_s}{2} - 2 v_{s\,ref} i_c^{LF} - (2 v_{xn}^{HF} i_c^{HF})^{LF} = 0. \tag{3.74}$$

For the last right-hand side term to have very low-frequency terms, i_c^{HF} and v_{xn}^{HF} are set to be of the same frequency. To accomplish this, the same frequency of v_{xn} is imposed to the voltage v_c that drives i_c. For example, if a sinusoidal waveform is chosen for the common-mode voltage:

$$\begin{aligned} v_{xn} &= V_{xn} \cos(\omega_{cm}) \\ v_c &= V_c \cos(\omega_{cm} + \theta_c) \end{aligned} \tag{3.75}$$

the displacement angle θ_c is, if the arm resistance R is disregarded, set to $\frac{\pi}{2}\ rad$. The common-mode voltage is directly injected into the converter, with a desired frequency and waveform, the next step is to define the peak voltage V_c, of the voltage v_c. From (3.75), $(2 v_{xn}^{HF} i_c^{HF})^{LF}$ can be rewritten as:

$$\begin{gathered} (2 v_{xn}^{HF} i_c^{HF})^{LF} = \frac{2 v_{xn} v_{c\,ref}}{\omega_{cm} L_{arm}} = \\ \left(\frac{2 v_{xn} v_{c\,ref}}{\omega_{cm} L_{arm}} \cos(\omega_{cm} t) \sin(\omega_{cm} t + \frac{\pi}{2}) \right)^{LF}. \end{gathered} \tag{3.76}$$

Finally, the relationship below is found:

$$(2 v_{xn}^{HF} i_c^{HF})^{LF} = \frac{v_{xn} V_c}{\omega_h L_{arm}}, \tag{3.77}$$

substituting (3.77) back into (3.74), considering that the power difference between the arms should be null, a definition for the peak value of the leg-offset voltage is obtained:

$$V_C = \frac{\omega_{cm} L}{v_{xn}} \left(\frac{V_{dc} i_s}{2} - 2 v_{s\,ref} i_c^{LF} \right). \tag{3.78}$$

A question remains, what are proper selections for the high frequency ω_{cm}, and waveform of v_c? No analytical rationale behind the choice of ω_{cm} is given by Jung, but a value of 100 Hz is applied in the experimental validation. Regarding the

waveform choice, Li [105] shows that the circulating currents related to sinusoidal waveforms are twice the ones related to square-wave injection. The application of a real square-wave is, in practice, impossible, as there would be the necessity of an infinite dv/dt level. That is the rationale behind the usual application of the trapezoidal waveform. Jung reports that, for the trapezoidal waveform, a 37% smaller circulating current was measured in comparison to the sinusoidal waveform application case. This choice does not come without drawbacks, though. As there are harmonic frequencies injection into the dc-side current, notwithstanding the general possible problems present in the driven machine caused by common-mode voltages with high frequency components. More on this topic is presented in Subsection 3.5.1.

Jung et al. consider that, for the application of a square or similar waveform, the resistance of the arm is the dominant impedance component [103] and that, consequently, the angle θ_c becomes zero. Furthermore, the waveform of v_{xn} and v_c are no longer the shown in (3.75) and are then defined as:

$$v_{xn\,sq} = \begin{cases} -V_{xn} & 0 \leq t < \frac{1}{2f_{cm}}, \\ V_{xn} & \frac{1}{2f_{cm}} \leq t < \frac{1}{f_{cm}}, \end{cases} \tag{3.79}$$

$$v_{c\,sq} = \begin{cases} -\frac{R}{2V_{xn}}\left(\frac{V_{dc}i_s}{2} - 2v_{s\,ref}i_c\right) & 0 \leq t < \frac{1}{2f_{cm}}, \\ \frac{R}{2V_{xn}}\left(\frac{V_{dc}i_s}{2} - 2v_{s\,ref}i_c\right) & \frac{1}{2f_{cm}} \leq t < \frac{1}{f_{cm}}. \end{cases} \tag{3.80}$$

In the control scheme, the reference for the peak value of v_c does not come purely from its analytical expression given by (3.80), it has another component, which is the output of a PI controller, following a reference for the energy difference between arms (E_Δ) in the same leg:

$$\begin{aligned} E_\Delta &= E_u - E_l, \\ E_u &= \frac{C_{SM}}{2}\sum_{i=1}^{i=N}(v^i_{SM\,l})^2, \\ E_l &= \frac{C_{SM}}{2}\sum_{i=1}^{i=N}(v^i_{SM\,u})^2. \end{aligned} \tag{3.81}$$

The strategy is depicted in Figure 3.17. The objective is to have no energy unbalance between arms, therefore, $E_{\Delta\,ref} = 0$. As can be seen, (3.80) acts as a feed-forward term. The kind of scheme shown in Figure 3.17 is called the energy balancing controller, or, the vertical balancing controller [61]. The scheme for a sinusoidal voltage injection would follow the same pattern.

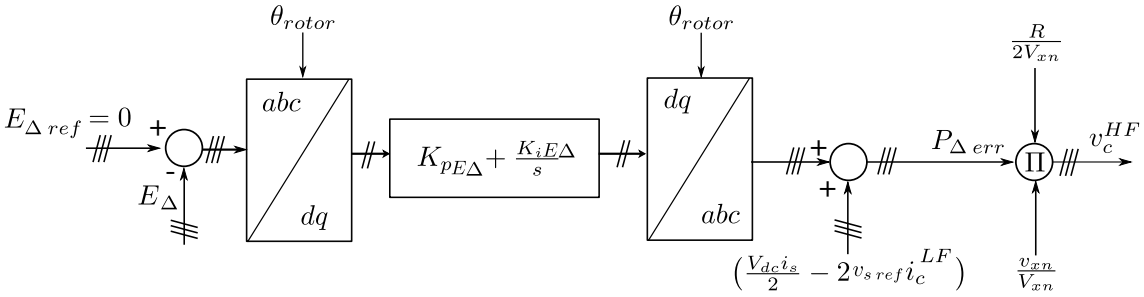

Figure 3.17: Vertical balancing controller considering square-wave injection ©2020 IEEE. Reproduced with modifications from [67].

The PI controller depicted in Figure 3.17 is located within the rotor-oriented frame. In the original scheme shown by Jung in 2014 [103], to the best of the author's understanding, there are no details about on which reference frame this PI-controller should be operating. In this dissertation, the rotor-oriented reference frame has been chosen based on the fact that, under low-frequency operation, the feed-forward term $\frac{V_{dc} i_s}{2} - 2 v_{s\,ref} i_c^{LF}$ has, as predominant, the rotor frequency component.

Another source of possible MMC capacitors voltage instability is the difference between energy input and output into the converter legs, keeping the energy within the MMC leg stable is the objective of what is known as the averaging control, or horizontal balancing controller [61]. The accumulation or depletion of energy per time unit in a leg of the converter is written as:

$$p_u + p_l = V_{dc} i_c - 2 v_{c\,ref} i_c - v_{s\,ref} i_s - v_{xn} i_s, \tag{3.82}$$

the same procedure followed for the vertical balancing controller is applied here, the low-frequency variations of (3.82) are the ones capable of causing voltage instability and therefore this equation is rewritten in terms of low-frequency components:

$$(p_u + p_l)^{LF} = V_{dc} i_c^{LF} - v_{s\,ref} i_s. \tag{3.83}$$

It is possible to, once again, obtain a feed-forward term. In this case, the feed-forward refers to the low-frequency circulating current order to be fed to the CCSC. By setting (3.83) to zero, it is possible to obtain:

$$i_c = \frac{v_{s\,ref} i_s}{V_{dc}}. \tag{3.84}$$

As for the vertical balancing controller case, the order is complemented by a PI controller tracking a reference of energy. In this case the controlled energy is the summation of the energy in the two arms of a same leg, and not the difference.

The total energy in a converter leg E_Σ is given by:

$$E_\Sigma = E_u + E_l. \tag{3.85}$$

The reference for this value is simply given by substituting the nominal SM capacitor voltage in the definition of E_u and E_l, given by (3.81). Adding horizontal balancing control to Figure 3.17 leads to the complete low-frequency control technique, shown in Figure 3.18.

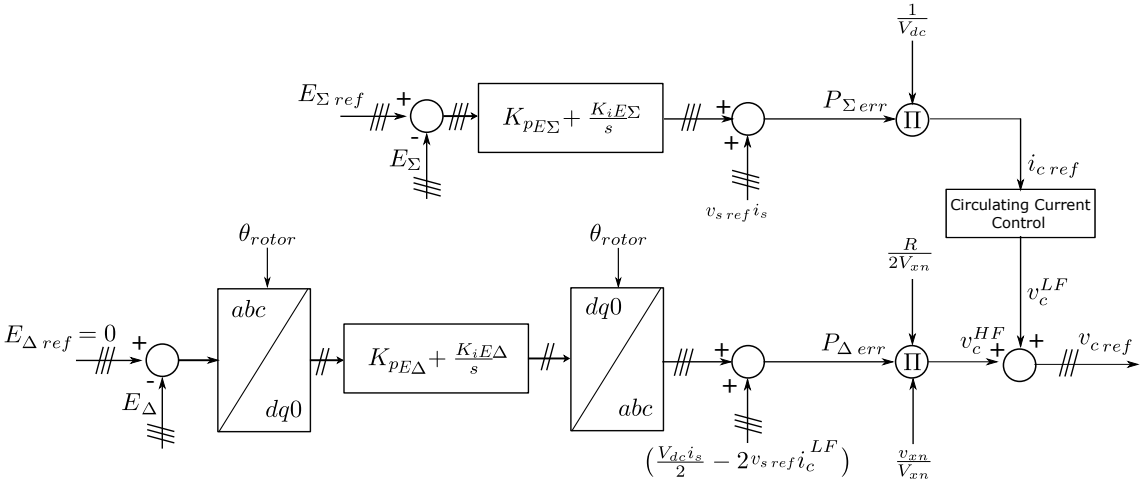

Figure 3.18: Low-frequency control of the MMC ©2020 IEEE. Reproduced from [67].

This control scheme is only active for low-frequency operation. When the frequency reaches a certain boundary, the horizontal balancing $i_{c\,ref}$ is set to zero and the CCSC resumes classical operation, simply suppressing circulating currents. The common-mode voltage injection is also interrupted. In this dissertation, the boundary frequency is set to 12 Hz.

3.5.1 Common-mode Voltage Drawbacks and Proposed Waveform

The effects of common-mode voltages on machines driven via power electronics has been subject of study since the 1990s. Originally, the source of this voltage was solely the power semiconductors switching characteristic, which caused a fraction of the dc-voltage to appear at the neutral of the driven machine and force current circulation through the stray capacitances present between conducting surfaces of the machine [106]. This current flow through the machine can happen in different ways depending upon machine characteristics and upon characteristics of the common-mode voltage waveform. This subsection briefly reviews these effects and discusses, in the context

of the low-frequency operation of the MMC, a common-mode waveform that could reduce some of these effects in comparison to the trapezoidal waveform.

Common-mode voltages related to power-electronics converters can generate what are known as bearing currents, these currents can possibly reduce a machine lifespan. They flow through the shaft and bearings of the driven machine, possibly causing loss of quality of lubricant oil, which increases vibrations and the risk of bearing failure [107]. These currents are divided in five types:

- Small capacitive currents: related to the dv/dt levels of the CMV, specially common in small machines near nominal speed operation. Usually considered to be harmless;
- Electrostatic discharge currents: related to the peak value of the CMV, and associated to machines operating near nominal speeds;
- Rotor grounded currents: possibly dangerous, high-intensity currents. Related to situations in which the machine has a grounded rotor shaft and poorly grounded casing. Specially related to large machines and pumps. Can be avoided with the use of shielded cables [108];
- Circulating bearing currents: related to large machines operating under low-speed. Due to CMV, a high-frequency current is established through the stray capacitances between stator windings and the stator iron. This initial current may induce a second current, circulating inside the machine and passing through the bearings. This induced machine happens specially under low-speed operation, for the bearing resistances are smaller on this range [109];
- Conduction currents: a current is established between the stator and rotor through stray capacitances, then flows through the bearings to the external frame. This current follows the same path of small capacitive currents but is differentiated by its relation to low-frequency operation [107].

A detailed discussion on the subject is beyond the scope of this work and can be found in, for example, Reference [110]. In general, the presence of bearing currents is related to CMV and the subsequent emergence of high-frequency currents flowing through stray capacitances. Reducing the high-frequency components and the amplitude of CMV is desirable to reduce the impact of these currents into the driven machine [111]. One of the advantages of the MMC is the smaller switching-related CMV levels if compared to the 2L-VSC [112], an effect increased with higher number of submodules per arm [113]. Besides, multiple techniques based on PWM variations have been proposed to reduce this CMV even further [114] [115] [116] [117]. In the case of the MMC operating under low-frequencies, though, there is the obvious

problem that CMV is being purposely injected with high amplitudes. According to Li et al. [118], Du et al. [119], and other works [120], this injection might be capable of causing bearing currents circulation and associated problems. Li et al. propose topological modifications to the MMC to deal with this and also point out, in other publication [105], that large CMV dv/dt levels could lead to stresses on the MMC arm inductors.

In this work, waveforms are compared in order to investigate if a differentiable approximation of a square-wave, henceforth called "smoothed square wave", could present advantages over the usually employed trapezoidal waveform. Figure 3.19 shows the two waveforms compared in this thesis, a square wave is also added to the graph. Care is taken to set a trapezoidal waveform and a smoothed square waveform that have the same maximum dv/dt and the same peak voltage levels.

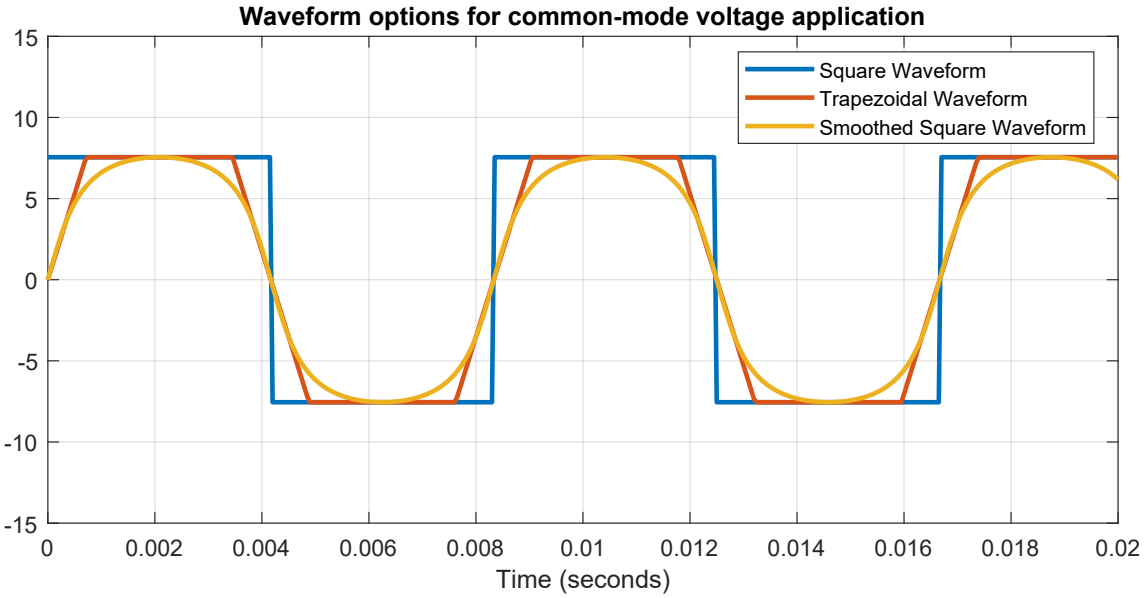

Figure 3.19: Comparison of possible waveforms to be applied as common-mode voltage ©2020 IEEE. Reproduced from [67].

The smoothed square waveform shown in Figure 3.19 has a closed expression based on trigonometric functions [1]:

$$sm_{sq}(t) = \frac{A}{\arctan\left(\frac{1}{\delta}\right)} \arctan\left(\frac{\sin(\omega_{cm} t)}{\delta}\right) \tag{3.86}$$

where δ is a positive real number. given in rad^{-1}. A is given in kV, and ω_{cm} in rad/s. Increasing the parameter δ leads to smoother signals, as shown in Figure 3.20.

[1] A discussion on ways of obtaining closed formulas for differentiable approximations of waveforms can be found at https://mathematica.stackexchange.com/a/38295, where formulas similar to (3.86) are described by user **ybeltukov**. There is at least another closed-form expression for a square-wave's differentiable approximation, described in Reference [121].

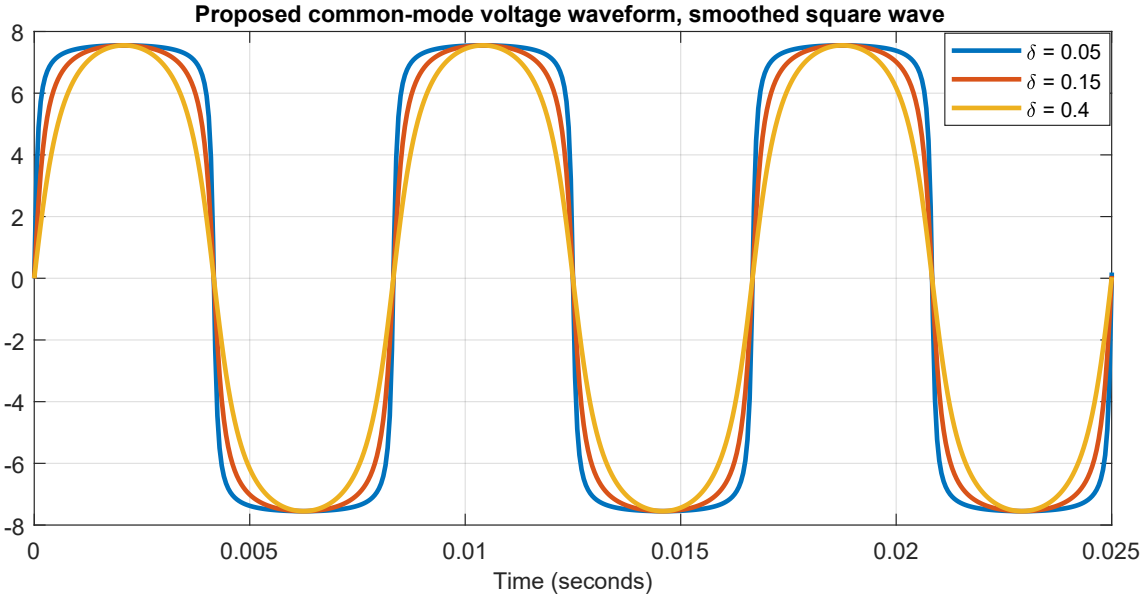

Figure 3.20: Proposed common-mode voltage waveform. Equation (3.86) parameters: A = 7.6, $\omega_{cm} = 753.98$ rad/s. ©2020 IEEE. Reproduced from [67].

The fact that such an expression exists is advantageous for the application of this waveform as the injected CMV. The existence of a closed-formula allows a relatively simple implementation of this option in a digital controller. Another possible advantage of such an expression is the fact that the variables δ and A can be chosen as function of chosen values for the frequency, peak-voltage and maximum dv/dt levels of the CMV. To obtain these relationships, the time derivative of (3.86) is first obtained:

$$\frac{dsm_{sq}(t)}{dt} = \frac{\omega_{cm} A\delta \cos(\omega_{cm} t)}{\arctan\left(\frac{1}{\delta}\right)\left[\delta^2 + \sin(\omega_{cm} t)^2\right]}, \tag{3.87}$$

the time derivative zeroes are located at $\omega_{cm} t = \frac{n\pi}{2}$. Therefore, the $sm_{sq}(t)$ peak value is:

$$sm_{sq}(t)_{peak} = A. \tag{3.88}$$

The time derivative maxima are located at $\omega_{cm} t = n\pi$. Thus, the maximum dv/dt level of the waveform can be written:

$$\left|\frac{dv}{dt}\right|_{max} = \frac{\omega_{cm} A}{\delta \ \arctan(\frac{1}{\delta})}. \tag{3.89}$$

Eq. (3.89) can be solved numerically for the variable δ. The minimum attainable dv/dt level is that of a sinusoidal wave: $\omega_{cm} A$, this is expected from Figure 3.20, where the waveform becomes increasingly smoother with higher δ, approaching the shape of a sinusoidal waveform.

A comparison between the smoothed square waveform and the trapezoidal waveform is made in terms of harmonic frequencies components. The signals shown in

Figure 3.19 are compared. In this example, $\delta = 0.4$. Figure 3.21 shows the harmonic frequencies, starting from the third order, present in each of the waveforms.

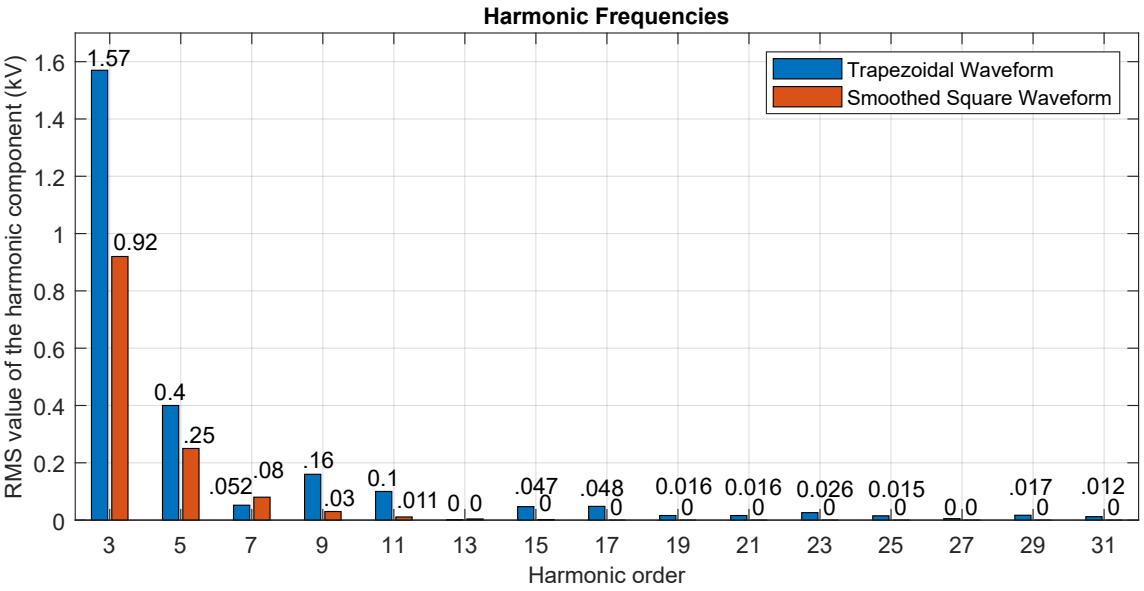

Figure 3.21: Comparison of RMS values of the harmonic components of trapezoidal and smoothed square waveform, fundamental frequency is 120 Hz. Values below 0.01 kV were considered to be null. ©2020 IEEE. Reproduced from [67].

The smoothed square waveform presents basically no harmonic components beyond the eleventh order, while the trapezoidal waveform, with the same peak and maximum dv/dt voltage levels, still present harmonic frequencies up to, at least, the 31st harmonic order. This seems to be an advantageous property of this waveform, as most bearing currents types, including the induced type, are related to high frequency currents flowing through machine stray capacitances. Taking these points into account, it might be advantageous, if possible, to apply this waveform instead of the usually studied trapezoidal waveform.

A question arises when applying this new waveform: the discussion so far has established that, depending upon the common-mode voltage waveform, the definition of the leg-offset voltage v_c may have or not a displacement angle in relationship to the common-mode voltage v_{xn}. When using this smoothed waveform, should the accompanying v_c order be displaced by $\frac{\pi}{2}$ as is the case for sinusoidal waveforms, or not displaced as is the case for the square-wave forms? The performed PSCAD/EMTDC simulations with $\delta = 0.4$ have shown that not adding any displacement to v_c has yielded good results, that is, the procedure applied to the square and trapezoidal waveforms remains valid.

3.6 MMC Simulation Model

Modular Multilevel Converters are considerably more complex than the usual 2L-VSC and this can lead to slower simulation times. The literature reports multiple techniques for the simulation of this type of converter, depending upon the objective of the study [57].

One of the objectives of this work is to evaluate internal variables such as the capacitor voltage ripples. This type of investigation requires detailed models representing the inner working of each submodule. The PSCAD/EMTDC model library contains a proper, submodule-level detailed model, which has been applied in this work. More detail on the inner workings of this model can be found in Reference [63].

3.7 Chapter Conclusions

The MMC has a tendency towards submodule voltage ripple during low frequency operation, the usually employed control technique developed to circumvent this condition is based on injection of common-mode voltage. As of today, the waveform usually employed is the trapezoidal waveform and, in this chapter, an alternative waveform with smaller high frequency components has been presented. This proposed waveform is a differentiable approximation of a square wave with the advantages of retaining the possibility of adjustable maximum dv/dt and peak voltage levels, and of being described by a closed-form expression.

Chapter 4

Methodology

4.1 Introduction

This dissertation consists fundamentally on time-domain simulation studies of a Full-size Converter VS-PHS using a Modular Multilevel Converter. These simulations are performed using the PSCAD/EMTDC software in its 4.6.3 version. There are three main lines of investigation:

- The design of the MMC-based VS-PHS, including main-circuit design and control system design, critically evaluating the possibility of retro-fit of existing units;
- The behavior of the MMC during start-up procedures compatible with those effectively employed in operating VS-PHS employing FSC, including the feasibility of a new common-mode voltage waveform;
- Synthetic inertia provision of the VS-PHS during pumping mode.

In the case of main-circuit design, the converter is designed with a similar nominal power to those currently operational in VS-PHS applications, the power semiconductor device applied is the same proposed by Steimer et al. [44] and applied in some currently operational projects [122]. The synchronous machine and hydraulic circuit data have been, as much as possible, based upon real data and criteria for PHS units, as reported by the literature [19] [69].

4.2 Hydraulic Data

4.2.1 Hydraulic Circuit

The energy density of a PHS reservoir greatly benefits from high heads. These high heads will, naturally, require longer penstocks, which will cause some energy losses.

PHS units follow a general rule of feasibility: usually a location is only considered fit for PHS if the ratio between the length of the penstock and the Head is below 10 [123].

As the PHS unit studied here does not really exist, the author has been forced to simply choose a value for the penstock length. As this work's objective is not to analyze hydraulic phenomena in detail, a ratio of 3 between penstock length and head is chosen. With this relatively short penstock the chance of elastic water column phenomena being of relevance to our studies is diminished [19]. Other quantities such as the diameter of the penstock are chosen based on typical values found in [19]. Using these choices and the hydraulic equations presented in Chapter 2, the data used in the hydraulic circuit model is derived and presented in Table 4.1.

Table 4.1: Hydraulic data.

Hydraulic Circuit Variable	**Value**
Nominal Head (H)	200 m
Penstock Length (L)	600 m
Penstock Diameter	2.5 m

4.2.2 Pumping Mode of the Reversible Pump-Turbine

Liang et al. [62] model a Francis Pump-Turbine within the range of hundreds of MW, the constants used in their modeling are considered to be a good first approximation to the case studied here, so they are slightly modified and applied as presented in Table 4.2, as has been exposed in further detail in Chapter 2:

Table 4.2: Pumping mode model data.

Pump model variable	**Value**
Variable relating speed and pump Head (a_0)	1.7
Variable relating speed-flow product and pump losses (a_1)	-0.2
Variable relating flow and pump losses (a_2)	-0.3
Variable relating flow and penstock losses (f_c)	0.01

4.3 Synchronous Machine Data

The machine modeled in this work is based on a 101.3 MVA synchronous machine currently operational on a hydro power plant. This particular apparent power value is chosen based on the current power trend for power-electronics based pumped hydro storage: while the scientific literature agrees that full-sized multilevel converters will eventually surpass the DFIM dominance on the hundreds of MW range, the present situation is that VS-PHS projects with full-size converters are confined to an upper boundary of, approximately, 150 MVA. Grimsel 2 VS-PHS is within that range [59] and the author believes that pioneering projects applying the MMC will remain within that power range.

4.3.1 Electrical Data

Table 4.3 shows the synchronous machine data as usually given by manufacturers, that is, in terms of traditional operational impedances and time constants of the studied synchronous machine.

Table 4.3: Synchronous machine data.

Circuit Variable	**Nominal Value**
Synchronous Reactance X_d	1.15 pu
Transient Reactance X'_d	0.32 pu
Sub Transient Reactance X''_d	0.26 pu
Synchronous Reactance X_q	0.75 pu
Sub-Transient Reactance X''_q	0.23 pu
Leakage Reactance X_l	0.12 pu
Transient Time T'_{do}	7.71 s
Sub-Transient Time T''_{do}	0.07 s
Sub-Transient Time T''_{qo}	0.2 s
Nominal Voltage (rms)	13.8 kV
Apparent Power	101.3 MVA
Nominal Electrical Frequency	60 Hz
Inertia Constant (H_{SM})	2.8 s

Given that one of the aspects of this work deals with common-mode voltage, it is reported that the neutral series resistance of the machine's model in PSCAD/EMTDC is 10 kΩ.

4.3.2 Saturation Data

Table 4.4 shows the magnetization characteristics in terms of magnetizing current and stator voltage, as entered into PSCAD/EMTDC.

Table 4.4: Synchronous machine magnetization characteristics as entered into PSCAD/EMTDC.

Current	Terminal Voltage
0.0 pu	0.0 pu
0.45 pu	0.57 pu
0.63 pu	0.742 pu
0.81 pu	0.931 pu
0.9 pu	1.0 pu
1.035 pu	1.1 pu
1.2163 pu	1.16 pu
1.368 pu	1.2 pu
1.8 pu	1.3 pu
2.7 pu	1.375 pu

The air-gap line nominal voltage is related to a current of 750 A, therefore configuring this current value as 1.0 pu.

4.4 Electrical Network Data

Two networks are employed throughout this work. Namely, first a Thevenin equivalent is directly connected to the PHS model. This network model is employed for simulations in which the only objective is to verify the behavior of the converter internal variables, or of the machine-side converter controlled variables. To investigate the dynamics of a power system, an 11-bus test network has been built. This is a modified version of the network presented in [124], which is itself originally inspired in the two-area system by Kundur [76].

4.4.1 Thevenin Equivalent

The applied Thevenin Equivalent Network has the characteristics shown in Table 4.5:

Table 4.5: Data regarding the Thevenin Equivalent Network.

Characteristic	Value
Voltage	500 kV
Short-Circuit MVA	5000 MVA
X/R Ratio	20

4.4.2 11-bus System

The unifilar diagram of the 11-bus system is shown in Figure 4.1. In this system, a VS-PHS with 8 parallel machines is employed, so the total rated active power is,

approximately, 800 MW.

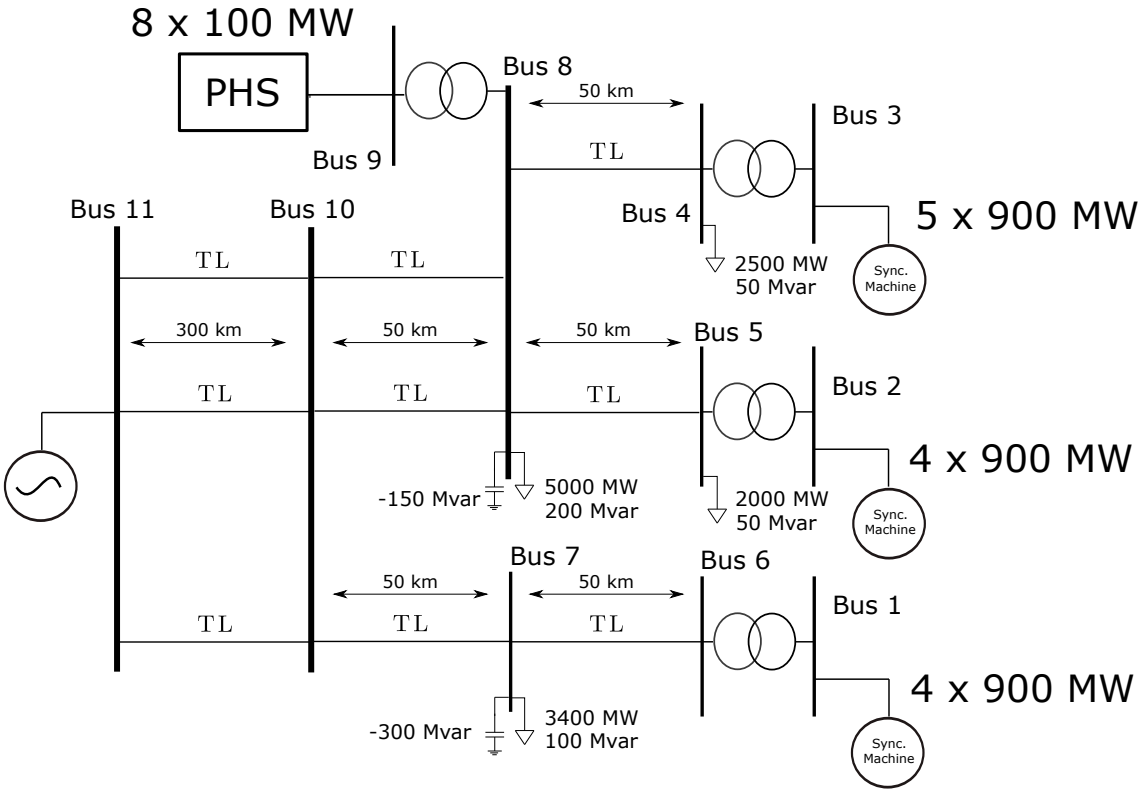

Figure 4.1: 11-bus system employed in simulations with the objective of investigating the synthetic inertial response of the MMC based VS-PHS.

The characteristics of the transmission lines (represented by TL), transformers and synchronous machines are presented on the Appendix A.

4.5 First Simulation Case: Start-up Procedure

The difficulties of low-operation frequency of modular multilevel converters have been widely reported [57] [60] [101]. The first simulation case is an investigation of this phenomenon. The MMC internal variables are observed and the effect of multiple control techniques are investigated. The simulation is performed with the Thevenin Equivalent network. The start-up procedure is based upon the Grimsel 2 unit operational experience [53], the time frames come from results reported in the literature [51] [70] which put the necessary time for start-up in, approximately, 60 seconds. The timeline of events during the start-up are:

- From t = 0 s to t = 25 s, the Reversible Pump-Turbine is accelerated to nominal speed against a closed spherical valve, that situation is modeled by ideally closed wicket gates ($G = 0$);

- the MMC low-frequency operation mode is active while the machine speed remains below 0.2 pu;
- From t = 25 s to t = 55 s, wicket gates are linearly opened until the fully opened state ($G = 1$).

It is expected that, with the implemented technique, this procedure allows for the correct start-up of the RPT in terms of active power while the SM capacitor voltages remain within the upper boundary of 3.3 kV, as will be further discussed in Chapter 5. It is also expected that even throughout the start-up, the MTPA scheme leads to almost no requirements of reactive power provision by the machine-side converter.

The start-up procedure is to be simulated with and without the low-frequency strategy described in Chapter 3. The injection of the proposed smooth waveform and of a trapezoidal waveform with similar amplitude and maximum dv/dt levels are compared. Every simulation is performed with a time-step of 10 μs.

4.6 Second Simulation Case: Synthetic Inertial Response

The 11-bus system is set to operate in the point described in Appendix A. In this situation, the stiff voltage source of Bus 11 is exporting, approximately, 1800 MW to the system with boundaries defined by Buses 7 and 8.

In the simulation, a contingency defined by the opening of two of the three circuits that connect Bus 11 to Bus 10 happens, causing an immediate decrease of power supply to the receiving system and, consequently, a frequency dip. The response of the PHS with inertial response during this time-period is observed.

It is expected that the VS-PHS with synthetic inertia decreases its power consumption in a considerably fast manner and contributes to reduction of ROCOF and frequency nadir.

4.7 Chapter Conclusions

This dissertation is organized in two PSCAD/EMTDC simulation cases. In one of them, the VS-PHS model is connected to a Thevenin equivalent with the objective of studying the start-up procedure. The other simulation case uses an 11-bus test system in order to evaluate the unit behavior during synthetic inertia provision. Data for the VS-PHS hydraulic components and start-up procedure are based on the operational experience reported on the literature.

Chapter 5

Modular Multilevel Converter Main Circuit Design

This chapter describes the MMC main circuit design. It deals with the main aspects of such a design, as outlined in [57]. It is important to notice that, as a back-to-back topology is employed, there are actually two converters: the machine side and grid side converters; in this thesis they are both identical. It is also important to notice that the several parts of main circuit design are not entirely uncoupled and the order in which the sections are presented is not representative of a correct order to follow in the design of a MMC. The modular multilevel converter main circuit design is an iterative process [57] and this is shown throughout the chapter.

In terms of the specific application of VS-PHS, this chapter shows that, if the machine-side converter is connected directly to the synchronous machine, the currently available semiconductor devices might be surpassed in terms of maximum rated electrical current. A similar discussion is presented by Milovanovic and Dujic [125], including alternatives related to parallelization options within the MMC structure. Literature review has also shown that, even though some IGCT devices may be compatible with the application in terms of voltage and current capability, their presently available commercial form might bring a set of complexities related to pulse driving [126]. The objective of the chapter is not to propose a design which solves every problem but to report on some challenges that could arise when employing the IGCT.

5.1 Nominal Power Selection

In this dissertation the MMC converter is designed to be able to withstand a power factor down to 0.8. Therefore, the converter nominal apparent power is 126.87 MVA.

5.2 Switching Semiconductor Device Selection

In one of the first papers proposing the application of MMCs to Pumped-Hydro Storage, Steimer et al. [44] propose the application of advanced IGCT technology. Applying IGCT, the authors say, a converter with a total efficiency of approximately 98% could be attained [44]. The IGCT has been chosen for the implementation of multiple currently operational medium-voltage high-power converters [122]. The superior efficiency of IGCT, its good reliability and applicability to MMCs, are also reported by Sharifabadi et al. [57]. If compared with the IGBT (Insulated-Gate Bipolar Transistor), the IGCT has approximately half the cost for the same capacity, higher surge current withstanding, and higher reliability. Disadvantages also arise though, as the presently available IGCTs require separate dc power supplies for the gate pulses and also snubber circuits. The power rating required for the driving circuit stands between 50 and 100 W, while for the IGBT it stands in the 10 W range. For the specific MMC application, which is based on submodules, the need for sets of separately excited dc supplies can considerably increase the cost and volume of the converter [126].

A bibliographic research on the voltage and current withstanding capabilities of the IGCT has been made. The 4.5 kV maximum voltage value is found for commercial IGCTs in multiple references [57] [127] [128] [129]. In terms of current capability, the main limiting factor of the IGCT is the maximum turn-off (that is, the maximum controllable) current and not the thermal capacity [130]. The maximum controllable current value of 5.5 kA, for an IGCT operating with 3.3 kV, has been reported in [131]. Another reference [132] reports 5 kA for operation with 2.8 kV. These electrical current values are superior in relation to the ones found for the IGBT, reported in the range between 2.4 kA [127] and 3.6 kA [133]. An alternative would be to adopt parallel connection of IGBT devices, allowing a larger current capability. This kind of parallel connection is reported to not be feasible with devices based on thyristor technology (such as the IGCT) [134]. The on-resistance value of IGCT is set to be 0.24 mΩ, based on ABB information [135].

The chosen device should be able to withstand a current i_{dev} that is function of the rated dc current i_{dc} and of the peak ac current i_{peakac} [57], as shown in (5.1):

$$i_{dev} = \frac{i_{peakac}}{3} + \frac{i_{dc}}{2}. \tag{5.1}$$

The power selection made in Section 5.1 leads to, assuming an operation under 0.9 pu ac voltage, $i_{acpeak} = 8.33$ kA and, assuming a dc voltage level of 28 kV (a reasonable value as will be seen later), $i_{dc} = 4.53$kA, yielding a value of $i_{dev} = 5.6$kA, slightly above the 5.5 kA mark reported by reference [131].

By now two factors presented in the introduction of this chapter are clear; first of all, the present power semiconductor device technology is pushed to its maximum capabilities in electrical drives such as the one studied here, the second point is that the main circuit design is an integrated process where choosing the dc-voltage level becomes also a function of the switching device's capabilities. This discussion is concluded by reporting that, for the present main-circuit design, the IGCT has advantages such as its higher current capabilities and superior efficiency, and that adjustments on the dc-voltage level will be made in order to maintain currents under the rated values. Employing a transformer between the converter and the machine would also solve the problem but at a higher cost and larger footprint, requiring an area that is possibly not available given that the equipment would be operating inside a dam. Another alternative would be to employ a parallel association of MMCs, as is done, for example, in the MMC-based STATCOM built in NP Kunta, in India [99]. This option would also bring higher costs and require more room for two converters and for duplicates of auxiliary equipment.

5.3 DC Voltage Selection

The previous section has shown that the dc-voltage selection is coupled to the device rating. Therefore, first the rationale behind the initial 28 kV value estimate is presented and then, in a second iteration, the voltage level is increased, keeping the currents within the semiconductor device rated values.

As presented in Chapter 4, the synchronous machine employed in this thesis has a 13.8 kV rated voltage and is Y connected. Therefore, the peak phase voltage is equal to 11.26 kV. A maximum operating voltage of 1.1 pu is considered and, therefore, the maximum operating peak phase voltage is 12.4 kV. At the same time, it is usual practice to have a dc voltage higher than strictly necessary, this extra dc voltage is sometimes called the electrical drive voltage reserve and usually remains within the 5% to 10% range [83]. In the first iteration a voltage reserve of 12%, approximately, is employed. This choice leads to the dc voltage level, between poles, of 28 kV.

As shown in the previous section though, increasing this voltage level would lead to a smaller contribution of current from the dc side, possibly reducing it enough to remain within the IGCT capabilities. The dc voltage level V_{dc} is, therefore, increased to 33 kV. This new level leads to, via 5.1, $i_{dev} = 5.45\,\text{kA}$. This value is, of course, calculated for the most stressing condition for the MMC, with 0.9 pu ac voltage and maximum apparent power. A condition very unlikely to occur at the machine-side converter, given the MTPA technique employed and the relationship between stator voltage and machine speed. Taking this into account, it is considered that the main-circuit design can proceed with the 33 kV dc voltage level choice. It is important

to once again notice that this design exercise shows a tendency of transformer-less VS-PHS applications with relatively low dc-voltage levels to considerably stress the semiconductor devices, specially taking into account that the machine used here does not have a particularly large power rating.

5.4 Number of Submodules

After a dc voltage level has been chosen, it is necessary to set the number of submodules (N) contained in each MMC arm. This decision is a function of, besides the dc voltage level itself, the power semiconductor employed. As the total dc link voltage V_{dc} will be imposed upon N submodules, the maximum withstanding voltage of the semiconductor technology will define the suitable number of submodules.

As shown in Section 5.2, the maximum current withstanding has been set considering that the switching devices will operate under a maximum voltage of 3.3 kV. A dc-voltage level ripple around 10% in each SM voltage is usually reported as a reasonable value [57] [136], as the MMC is applied in an variable speed application, we choose to apply N = 12 submodules per arm, allowing for percentual ripples up to 16 %.

5.5 Switching Frequency

While increasing the switching frequency leads to better harmonic elimination and to smaller voltage fluctuation on each MMC submodule, the IGCT is a device optimized to reduce conduction losses and has a typical switching frequency in the 500 Hz range [135] [137]. At the same time, it is reported that a better voltage balancing between the submodules is obtained from a switching frequency which is not a multiple of the fundamental frequency [57]. The machine-side converter is related to a variable frequency ac-system, so the extent to which such a recommendation is relevant is not clear. However, based on the grid-side converter, the author has chosen a switching frequency for every submodule of 687 Hz (11.45 times that of the 60 Hz fundamental). The PWM scheme employed is the Phase-Shifted Carrier PWM, as explained in Chapter 3.

5.6 Submodules Capacitance

The definition of the submodules capacitance requires the definition of the energy-power ratio of the converter E_P:

$$E_P = \frac{E_{Cmax}}{S_{MMC}}, \tag{5.2}$$

where E_{Cmax} is the maximum energy stored in the capacitors and S_{MMC} is the converter's rated power. The energy-power ratio concept is very similar to the usual inertia constant H usually employed for synchronous machines.

As the capacitors are responsible for, approximately, half of each submodule's volume, it is desirable to minimize capacitance in order to reduce the overall converter's size [138]. On the other hand, larger capacitors lead to smaller voltage fluctuations. Capacitance choice is, therefore, a trade-off between performance and cost which can be represented by E_P. Larger energy-power ratio values would lead to bulkier converters while presenting smaller voltage fluctuation. Zygmanowski et al. [136] report that typical values of E_P for MMCs fall within the 10-50 kJ/MVA range and present a table with multiple design choices from the scientific literature. In [138], a minimum value of 39 kJ/MVA is recommended for a converter operating in a 50 Hz grid and dealing with pure reactive power operation, [57], on the other hand, presents the range of 30-40 kJ/MVA as a reasonable first estimation for capacitor sizing, both references consider a 10% voltage ripple in each SM to be acceptable.

The total energy stored in the dc-side of the MMC's submodules can be written, if it is considered that the voltage between submodules are equally distributed (that is, there is no variation between each submodule voltage), as [136] [138]:

$$E_{dclink} = 6N\frac{C_{SM}}{2}V_{SM}^2, \tag{5.3}$$

where N is the number of submodules in each arm, C_{SM} is the capacitance of each submodule and V_{SM} is the nominal voltage in each submodule, considering, as previously said, that the dc-link voltage is equally distributed throughout the N submodules in the on-state.

The variable frequency nature of the VS-PHS application requires regular low frequency operation, under relatively low voltages. Pure reactive power control, on the other hand, would only happen on the grid-side converter, where frequency would only deviate slightly from the nominal value. Also, the nature of the VS-PHS application requires an attempt to minimize the volume of the converter, given the expected scarcity of physical space inside a dam. Given these observations, the design choice followed here is, in a first attempt, to apply two-thirds of the

value recommended by Green at. al [138], that is $E_P = 26$ kJ/MVA, this value could possibly be reduced if modulation with triple harmonic insertion were used [138] but that is not the case here. As previously states, this value could also be described as the converter's inertia constant. In this case, this value would be 26 ms, a value approximately one hundred times smaller than the inertia constant of the synchronous machine employed in this dissertation.

Substituting (5.2) into (5.3) yields a closed formula for the capacitance of each submodule for given values of N, E_P and V_{dc}:

$$C_{SM} = E_P N \frac{S_{nom}}{3V_{dc}^2}, \tag{5.4}$$

applying the chosen values of N, E_p, S_{nom} and V_{dc}, (5.4) yields, approximately, $C_{SM} = 12000\,\mu$F. That is above most, but not all, of the design examples found by Zygmanowski et al. [136]. This gives a value for total capacitance of each arm of $C_{arm} = 1000\,\mu$F.

5.7 Arm Inductances Selection

Arm inductance selection is another way of possibly increasing the maximum current capability of the converter, larger arm inductances might cause a larger voltage drop within the converter in relation to the external ac voltage [57]. In this work, though, the selection is done mainly to avoid resonances within the converter.

As discussed in Chapter 3, the MMC has a circulating current containing harmonics of even order. The procedure outlined in [136] is followed. With that, the circulating current suppression control is not considered in the decision process. As discussed, the steady state converter operation will have the CCSC activated, so the choice presented in this section can be understood as conservative.

In an MMC, the operating frequency under which resonance occurs can be written as [136]:

$$f_{reson} = \frac{1}{L_{arm}C_{arm}} \frac{2(h^2-1) + m_a^2 h^2}{8h^2(h^2-1)}, \tag{5.5}$$

where h is the even-order harmonic, h = 2n, n = 1, 2, ... ∞ and m_a is the modulation index. By manipulating (5.5) it is possible to find which values of inductance would cause resonance for each set of variables. In order to determine which are safe arm inductance values choices, operating frequencies of 45, 50, and 60 Hz are studied while the capacitance is set to be the value chosen in the previous section. The modulation index is allowed, for each of those frequencies, to vary between 0.1 and 1.0. Priority is given to the harmonic frequencies of order 2 and 4, as done in [136]. The results are shown in Figure 5.1.

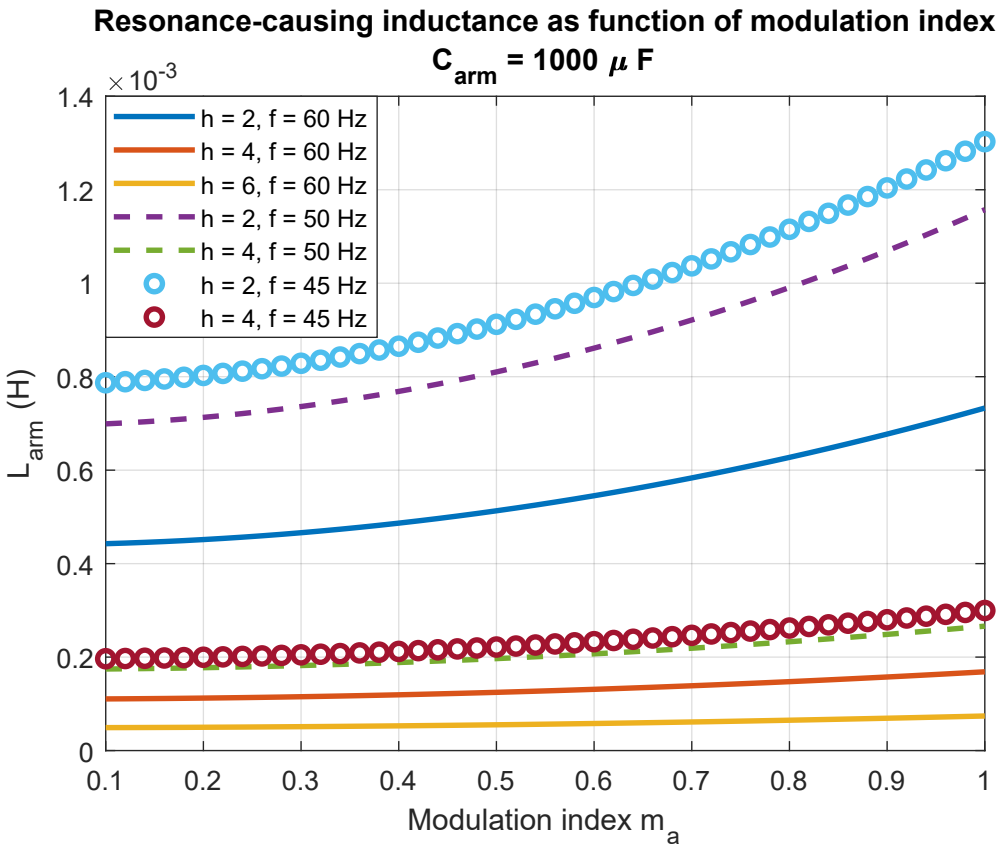

Figure 5.1: Set of arm inductances which are resonance-prone.

Each line represents a set of undesirable choices and, as the electrical drive operating frequency is expected to vary between, approximately, 60 Hz and 45 Hz, we can choose the two extreme plotted lines in Figure 5.1 as boundaries of an undesirable region that might be attained during the drive operation, this region is shown in red in Figure 5.2.

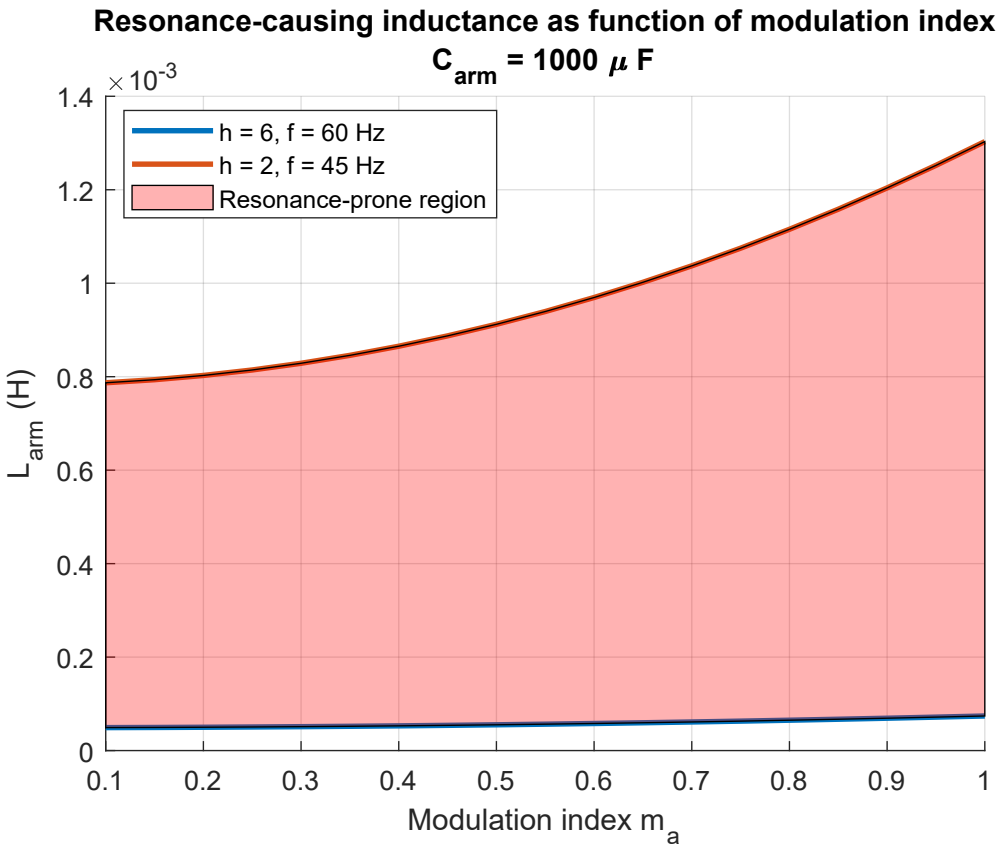

Figure 5.2: Resonance-prone arm inductance selections for the expected operating region of the machine-side converter.

Observing the undesirable region of Figure 5.2, the design of arm inductance is set to be $L_{arm} = 1.4\,\text{mH}$. This value is equivalent to 0.2 pu in the converter base. If there were no need for an operation in frequencies as low as 45 Hz, this value could be reduced to approximately 0.11 pu. This can be observed on Figure 5.1, as the highest values of resonance-causing inductances are related to 45 Hz operation. Values in the $0.1 - 0.15$ pu region are reported as usual for converters required to deal with dc-link faults without bypass thyristors or other techniques to protect the SM switches [57]. The wide frequency operating region gives rise to this peculiarity where a back-to-back converter ends up having an arm inductance with the same per unit scale of converters prone to dc-link faults.

5.8 AC Filter

It is widely reported that modular multilevel converters applied to HVdc links usually require very small filters or none at all. It is well known that the harmonic generation levels of such converters are very small [57] [93] [127] and that usually the most worrying power quality related phenomena is related to harmonic instability caused by the interaction between the converter and other equipment on the

power grid [94]. The usual characteristics of filters for MMC are reported by a CIGRE Working Group [94]. It is reported that filters for such converters are usually very small, have a low quality factor ($Q \leq 3$) and are tuned to frequencies close to the switching frequency. This report also contains harmonic distortion levels recommended by the IEC 61000-3-6 standard. In this work, simulations without ac filters are performed, the results for the voltage distortion at the Point of Common-Coupling (PCC) are investigated and compared with the levels presented in the IEC 61000-3-6 standard. The Total Harmonic Distortion (THD) definition applied in this work excludes interharmonics, as considered by the same IEC standard [94]. Distortion levels for simulation cases with the detailed MMC model and a 5 μs time-step are presented. The grid model considers a Thevenin Equivalent with short-circuit power of 5000 MVA and an X/R ratio of 20. This grid based on a Thevenin equivalent is the same described in Chapter 4. The distortion levels are evaluated during steady-state operation, that is, power quality considerations are not made for the start-up procedure. To verify the distortion levels, a simulation is run with the Variable-Speed Pumped Hydro station operating with unity power factor and absorbing 85 MW of active power. The distortion levels for this condition are shown in Table 5.1.

Table 5.1: Comparison between distortion levels as required by IEC 61000-3-6 for High-Voltage and Extra High-Voltage grids and distortion levels as found via simulation.

Harmonic order	**IEC 61000-3-6 requirement**	**Simulation without ac filter**
2	1.4 %	0.023 %
3	2.0 %	0.015 %
4	0.8 %	0.012 %
5	2.0 %	0.010 %
6	0.4 %	0.010 %
7	2.0 %	0.007 %
8	0.4 %	0.008 %
9	1.0 %	0.008 %
11	1.5 %	0.01 %
13	1.5 %	0.009 %
15	0.3 %	0.008 %
21	0.2 %	0.01 %

By observing the values shown in Table 5.1 it becomes clear that the observed distortion levels are well within the recommended ranges. Taking this into account and the fact that it is desirable to minimize room requirements, the design decision is to operate without an ac filter.

5.9 Chapter Conclusions

This chapter has shown that medium voltage electrical drives with power ratings in the range of the hundreds of MW not employing a transformer at the machine-side are quite demanding regarding the electrical current ratings of the presently available power semiconductor switches, as described in the literature [125]. The semiconductor employed, the IGCT, presents advanteges related to smaller conduction losses. Yet, the parallel association of IGCTs is still an open problem. This is a possible caveat for the application of the MMC on VS-PHS in an IGCT-based, transformerless configuration. The addition of a transformer, or of parallel-connected MMCs, would possibly violate tight room availability and would also eliminate one of the MMC-based solution advantages over the solution presently operational at Grimsel 2, employing the three-level Active Neutral Point-Clamped Converter. On the other hand, even though the converter must deal with low-frequency operation, it was not necessary to increase the amount of energy within the converter to counteract this. In other words, this is a regular converter in terms of capacitor sizing.

Chapter 6

Control Systems Design

6.1 Introduction

In this work, the control system design is presented for the machine-side converter and for the grid-side converter. As the case studied here is that of a back-to-back structure, there are different control structures spread among the two converters. Figure 6.1 shows a general view of the control objectives and measurements of each converter.

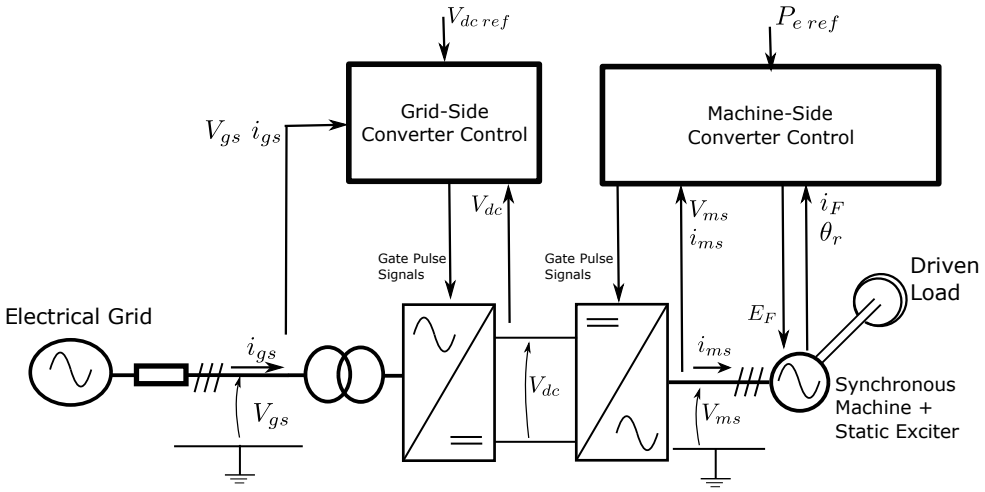

Figure 6.1: Basic control structures present in each of the converters.

In the structure adopted here, the machine-side converter contains a field-oriented control structure and has the objective of tracking a certain active power reference while operating with a power factor as close as possible to unity. This is a usual control structure, commonly found in the literature [78] [139]. The grid-side converter has two objectives, it controls the dc-bus voltage level and, consequently, allows for the correct flow of active power; it is also capable of contributing to ac-voltage control, configuring the provision of an ancillary service. The machine-side converter control general strategy and estimators have been presented in Chapter 3

and the present chapter deals with the design of controllers and with the system dynamic responses

A typical way of designing a controller is to set the control loop to have a specified bandwidth response [140] [141]. This can be done, equivalently, by choosing a certain desired time constant for the equivalent first order transfer function. Usually, for Voltage-Source Converters, current control is the most basic and fundamental control loop [86] and is the first control design level detailed in this chapter. Before proceeding, it is important to remember that the relationship between the time constant τ, in seconds, of a first order transfer function and its bandwidth α_B, in radians per second, is given by (6.1):

$$\tau = \frac{1}{\alpha_B}. \tag{6.1}$$

If the interest lies in using a PI controller of the form $K_p + \frac{K_i}{s}$ to control a first-order plant and, therefore, acquire a closed-loop transfer function with certain specified time constant t_c and bandwidth α_c, a criterion for the choice of K_p and K_i becomes necessary. In the case of current control, the so-called first-order plant is an RL circuit, the control loop described here becomes, therefore, the one shown in Figure 6.2.

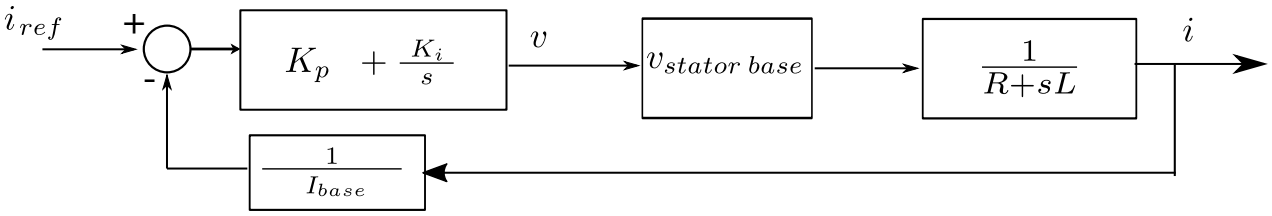

Figure 6.2: Current Control Loop.

The open-loop transfer function of the control scheme shown in Figure 6.2 can be described and developed as follows [86] [141]:

$$G(s) = \left(K_p + \frac{K_i}{s}\right)\left(\frac{1}{R+sL}\right) = \left(\frac{K_p}{sL}\right)\left(\frac{s+\frac{K_i}{K_p}}{\frac{R}{L}+s}\right), \tag{6.2}$$

clearly $G(s)$ has a pole $p_1 = \frac{-R}{L}$, at the same time, there is a zero $z_1 = -\frac{K_i}{K_p}$. The objective is to have a closed loop behavior similar to a first order transfer function of the form $\frac{1}{1+\tau_i s}$, such a closed loop behavior requires an open loop gain with no zeroes and a single pole. This can be achieved canceling p_1 with z_1 through the following criterion [86]:

$$K_p = \frac{L}{\tau_i}$$
$$K_i = \frac{R}{\tau_i}. \tag{6.3}$$

Alternatively, this same criterion can be presented as function of bandwidth and taking into account the per-unit bases. For the proportional term, given in pu/pu [140]:

$$K_p = \frac{\alpha_c X_L(\Omega)}{Z_{base}} \tag{6.4}$$

and for the integral term, given in 1/s :

$$K_i = \frac{\alpha_c R(\Omega)}{Z_{base}}. \tag{6.5}$$

Once there is a criterion for the choice of controller constants given a desired bandwidth, the next question is, what is the criterion for choosing the desired bandwidth for current control? In the case of VSC, the choice of current control time constants usually remains between 0.2 and 2.0 ms [86]. In this work, $t_i = 2.0$ ms is chosen. Leading, via (6.1), to $\alpha_c = 500$ rad/s.

Proportional-Integral controllers are only capable of reference tracking of dc-quantities and, for that reason, the control of grid-connected converters is usually made in the synchronous reference frame based upon synchronization via Phase-Locked Loop (PLL) [86]. That is the procedure followed here for the grid-side converter. Important observations must be made regarding the machine-side converter, though, as it configures a variable-frequency system and the synchronization happens in relation to the machine rotor position, more detail on that is given in Section 6.2.

6.1.1 Per-Unit Systems

Electrically excited synchronous machines have fundamentally two per-unit base systems, one for the excitation systems and one for the network [76]. As can be seen in Figure 3.3, the rotor and stator circuits, even though electrically isolated, can be represented as a single circuit. That, as for the case of transformers, happens due to a certain choice of per-unit systems [89]. The per-unit system which allows for a single circuit representation is usually called the L_{ad}-base reciprocal system [76] and, of course, results in different impedance base values for rotor and stator circuits. As for any electromagnetically coupled circuit, the bases for apparent power and time must be the same [89]. This system, as usually used by the manufacturers for stator quantities, has the following characteristics [83] [86] [89]:

- Stator base-voltage v_{base}: peak phase voltage.
- Stator base-power: S_{3ph}, the three-phase machine rated power in MVA.
- Stator base-current i_{base}: peak line current.

The manufacturers also supply the machine saturation curve, from which the base-current for the excitation system can be obtained [76] [89]:

- Excitation system base-current I_{Fbase}: current value that, at the air-gap line, generates nominal terminal voltage.

From the data given by the manufacturer it is possible to obtain the current and voltage bases (i_{Fbase}, V_{Fbase}) for the rotor circuits on the L_{ad}-reciprocal system and on the non-reciprocal system (I_{Fbase},E_{Fbase}) using the following relationships [76]:

$$\begin{aligned} i_{Fbase} &= \frac{I_{Fbase}}{L_{ad}} \\ V_{Fbase} &= \frac{S_{3ph}}{i_{Fbase}} = \frac{r_F}{L_{ad}} E_{Fbase} \end{aligned} \tag{6.6}$$

6.2 Control of the Machine-Side Converter

6.2.1 Introduction

This section covers the detailed control design of the machine-side converter, using the modeling and control concepts covered in the preceding chapters. The control technique employed here is the so-called air-gap flux oriented control. As the objective is to present the control design, results are first presented using a VSC converter averaged model. The final results, using a detailed MMC model, are presented in Chapter 7.

As the control of an electrically excited synchronous machine consists of multiple basic blocks, this chapter is divided in multiple sections, one for each major control objective:

- Stator Current Control
- Excitation Control (Field Current)
- Air-Gap Flux Control
- Speed Control
- Power Control
- Magnetic Saturation Estimator

6.2.2 Stator Current Control

As previously stated, the control systems based on PI controllers employ the synchronous reference frame and, with that, there are two current controllers for each converter, each one dealing with the current in each axis of the rotating reference given by the angle of the machine's rotor. Therefore, there are two independent branches, as shown in Figure 6.3, containing regular feedback control and a decoupling factor between the direct and quadrature axis.

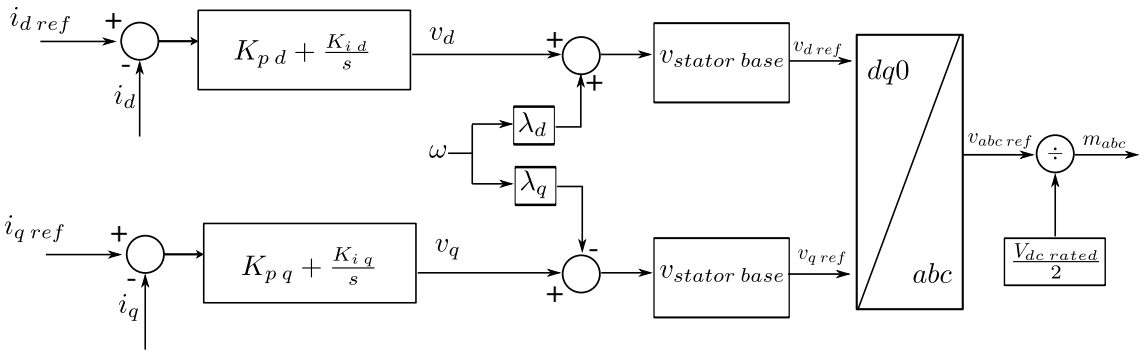

Figure 6.3: Stator current control diagram.

To design the PI controllers, the closed-loop control model shown in Figure 6.4 is employed:

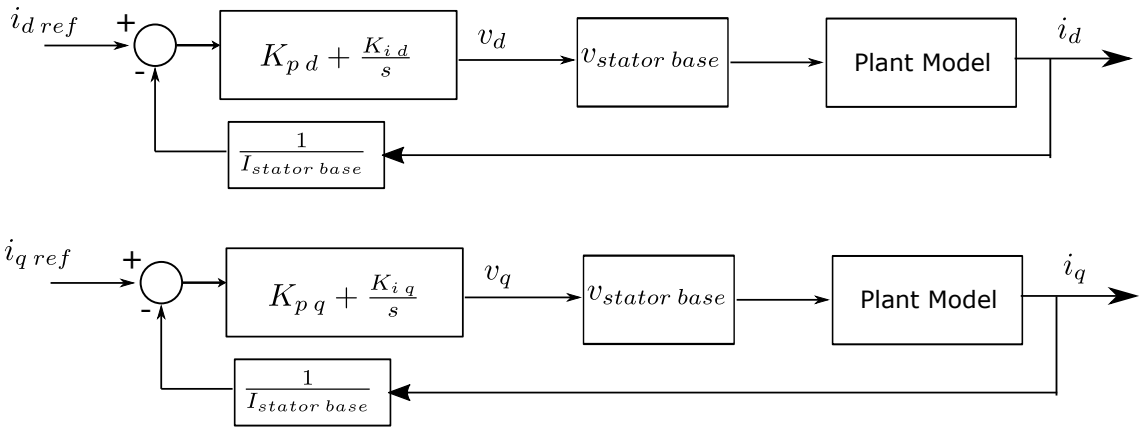

Figure 6.4: Stator current control diagram.

The design of the d-axis current is now presented.

Direct-Axis Stator Current Control

The machine data given in Chapter 4 contains part of the circuit parameters necessary for controller design, namely: armature resistance ($r_s = 4.4\,m\Omega$) and synchronous inductance ($L_d = 5.7$ mH) values. The other value of interest comes from the converter data. In the usual MMC model, the converter output current is being

driven through this resistance r_{MMC}, usually considered to be a quantity modeling the MMC losses and assuming values reaching 0.1 Ω for converters with hundreds of submodules [57] [142]. An approximation considering the slope resistance of the IGCT presented in Chapter 5 and that the output current can be flowing through up to 12 submodules yields $r_{MMC} = 2.9\,\text{m}\Omega$. The MMC arm inductances are not considered in the stator current control design, as the synchronous machine model inductance values are 8 times larger than the MMC arm inductances.

With the necessary data for the control design already gathered, a discussion regarding the synchronous machine model must be introduced. The current control design is made as if the plant were a RL circuit, but a synchronous machine model actually presents different time constants (namely: synchronous, transient and sub-transient). The design criterion followed here was using the synchronous inductance. This is done because the current control loop reference is the final output in a cascade of slower control loops, ultimately leading to relatively slow reference changes. With that, it is expected that, during most operation circumstances, synchronous inductance better represents the machine. This discussion yields the Plant Model, for the controlled machine, from the point of view of stator current control, shown in Figure 6.3

$$\frac{i_d(s)}{v_d(s)} = \frac{1}{r_{MMC} + r_s + s\,L_d}, \tag{6.7}$$

by applying these inductance and resistance values to (6.4) and (6.5), the following d-axis controller constants are found: $K_{pd} = 1.52$ and $K_{id} = 1.9365\ \text{s}^{-1}$. A closed loop model is built in Matlab and its step response is shown in Figure 6.5.

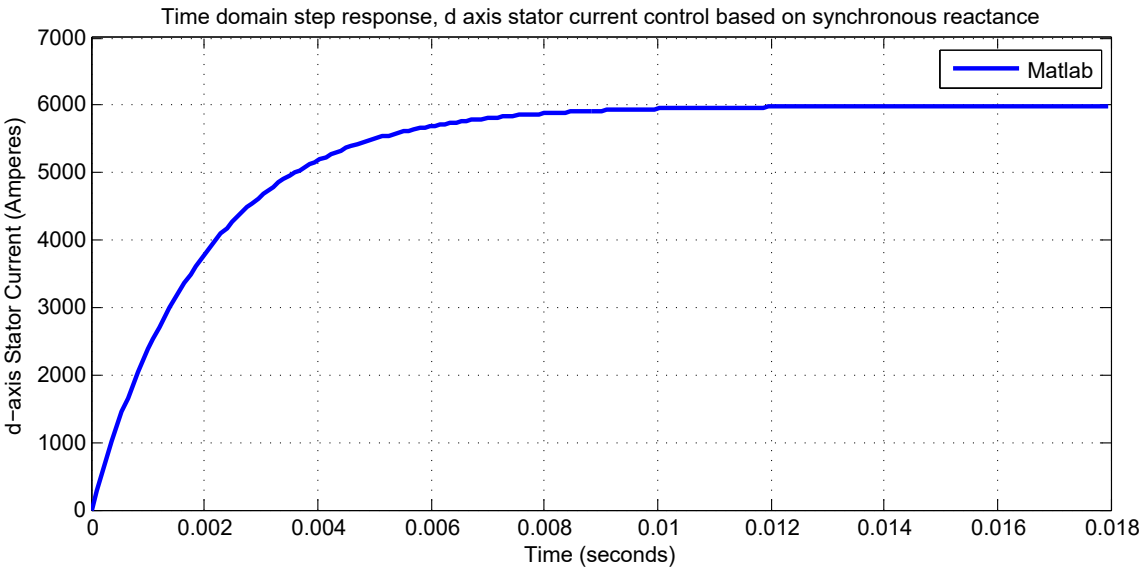

Figure 6.5: Matlab d-axis current step response.

The response has good correspondence with the desired time constant. The system reaches the final value in approximately 0.01 s. That is, five times the chosen time constant, as expected. The Matlab command *bandwidth* returns $\omega_c = 498.98$ rad/s, further confirming that, if our machine model represents the plant correctly, the time-domain control objectives have been obtained. Figure 6.6 shows the comparison between the response obtained in Matlab and PSCAD.

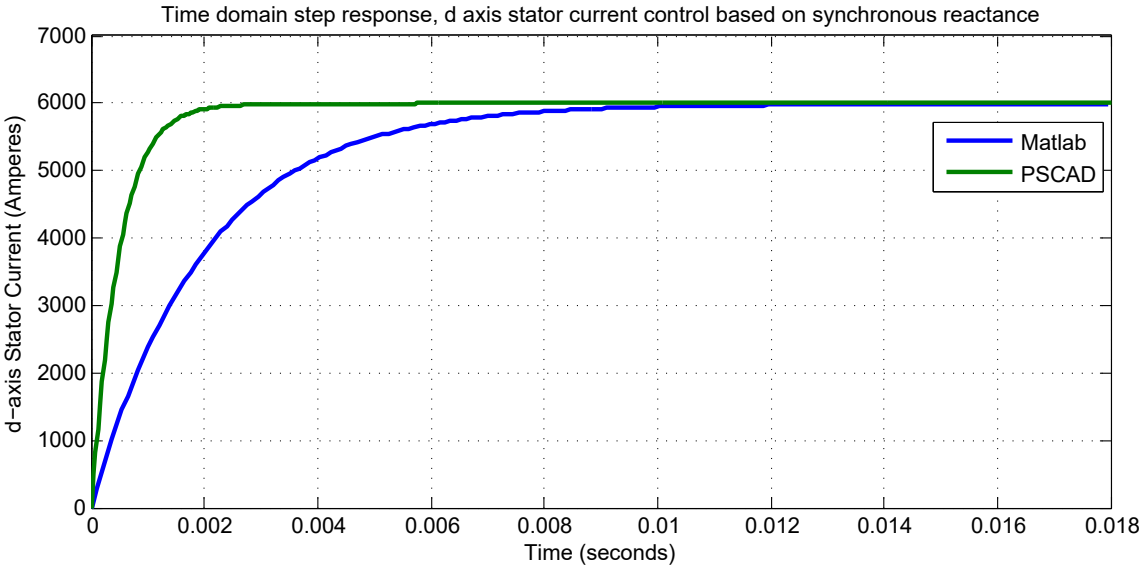

Figure 6.6: d-axis current step response, comparison between PSCAD and Matlab models for a control design considering synchronous reactance.

The responses shown in Figure 6.6 are considerably different, and that is explained by the fact that the design applied L_d. In other words, the Matlab machine model has been built using the response of the machine to slow phenomena and has

been tested for a sharp change of stator current. Figure 6.7 shows the same comparison, but now the model has been updated and the control has been redesigned using L''_d, leading to another proportional constant ($K_{pd} = 0.3448$).

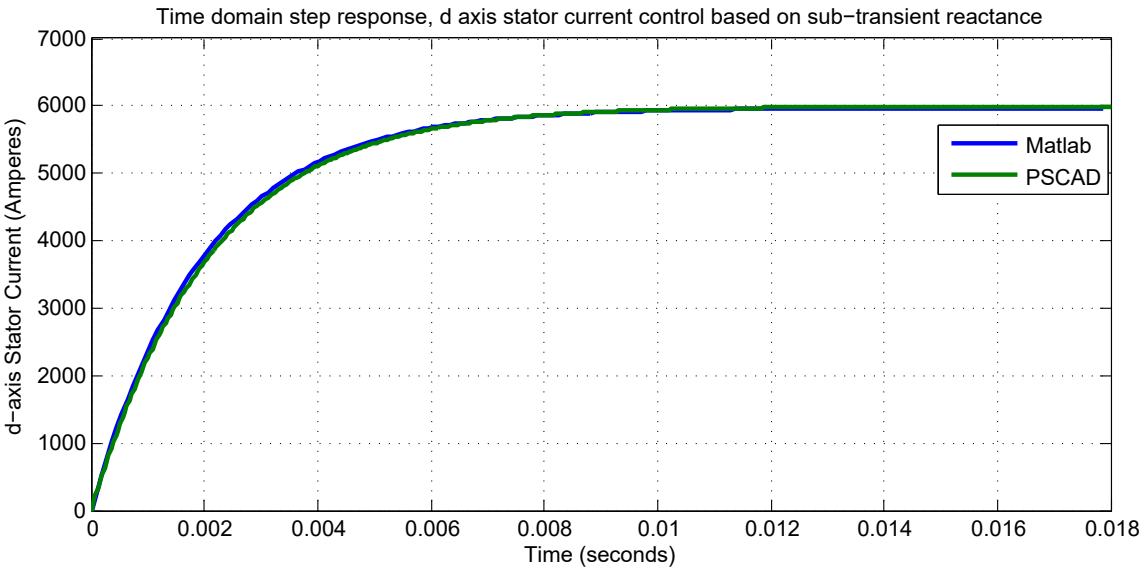

Figure 6.7: d-axis current step response, comparison between PSCAD and Matlab models for a control design considering sub-transient reactance.

It can be seen that now the responses are very similar and present the desired time-domain behavior. That is expected as now the model more accurately represents the machine for this kind of input. This result demonstrates the equivalence between Matlab and PSCAD models and the usefulness of the applied control design method. As previously stated, though, the PI controller actually used throughout this work is the one based on synchronous quantities, with that in mind, the gains are the ones presented previously: $K_{pd} = 1.52$ and $K_{id} = 1.9365$ s^{-1}. A final time-domain comparison is done between Matlab (with the L_d based model) and PSCAD for a filtered step response. A first-order filter with 20 ms time constant is added to the input. Figure 6.8 shows that for this kind of smoother reference, the responses are similar.

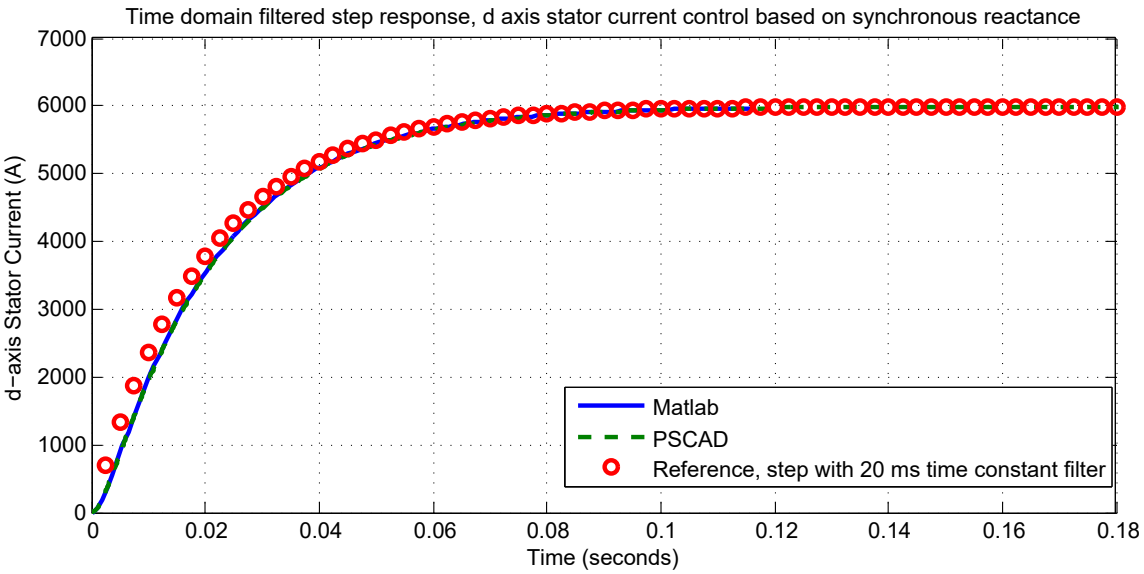

Figure 6.8: d-axis current filtered step reference and responses simulated on PSCAD and Matlab, for the final control design considering synchronous reactance.

Some investigation on the behavior of this control loop regarding stability is now presented.

Stability of the Direct-Axis Stator Current Control

From the point of view of stability, the bandwidth of the output current closed loop α_c has upper limits dependent upon the delays related to the MMC control [57]. A recommended design practice is that the bandwidth of the closed loop should be, at least, 10 times smaller than the angular frequency related to the sampling period (T_s) [86]. In the present case this criterion is easily satisfied, as the bandwidth choice has been mostly motivated by the large inductances related to the synchronous machine. If an excessively fast control (that is, with a large bandwidth) were chosen, this could require large voltage references and, therefore, overmodulation. With that in mind, an example in terms of phase and gain margins is now presented and shows that the d-axis current control loop as previously designed presents no problems from the stability point of view.

We begin by considering that the total delay related to the converter is $1.5T_s$ and that the sampling frequency f_s is $5\,kHz$. This gives a total delay time $T_d = 0.3$ ms. Adding this delay to the block diagram shown in Figure 6.2 and plotting the bode diagram (see Figure 6.9) allows the observation that both gain margin (which is infinite) and phase margin (which is 81.6°) indicate a closed-loop stable system with a good margin against uncertainties.

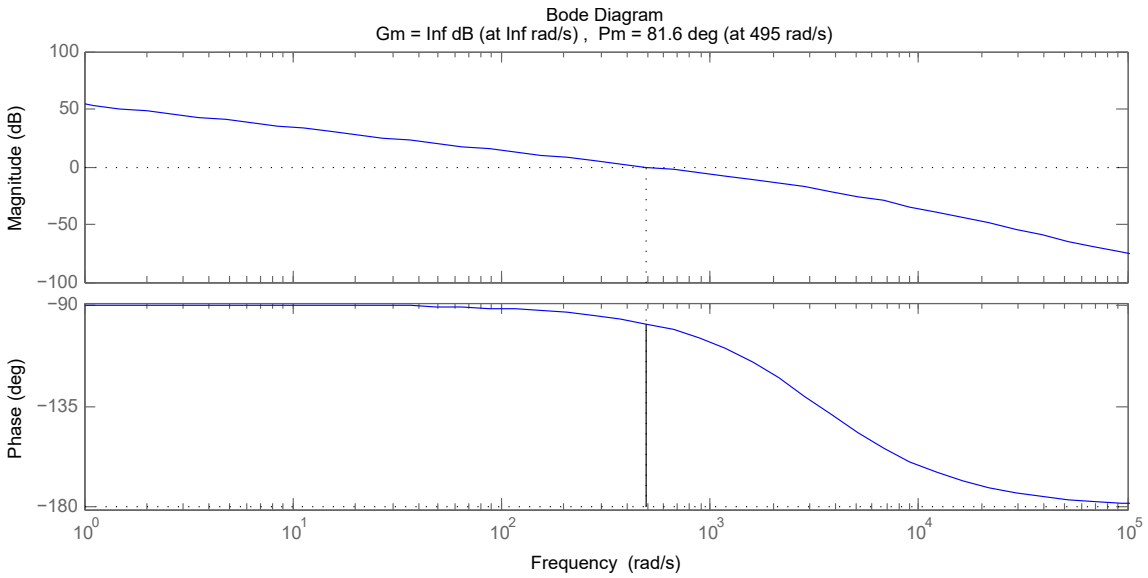

Figure 6.9: d-axis current control frequency response, considering a total delay time of 0.3 ms related to switching, communication, and sampling.

Quadrature-Axis Stator Current Control

The same procedure is followed through for the q-axis circuit. In this case, the constants of interest are: $r_s = 4.4\ \text{m}\Omega$, $r_{MMC} = 2.9\ \text{m}\Omega$ and $L_q = 3.7\ \text{mH}$. The transfer function relating voltage and output current becomes, for the q-axis:

$$G(s) = \frac{1}{r_{MMC} + r_a + s\,L_q}. \tag{6.8}$$

Application of these inductance and resistance values to (6.4) and (6.5), leads to the the following q-axis controller constants: $K_{pq} = 0.99$ and $K_{iq} = 1.9365\ \text{s}^{-1}$. Just like in the case for the d-axis, there is a difference between modeling for the synchronous response and the sub-transient one, the control based on the synchronous reactance transfer function is the one employed, for the same reasons explained for the d-axis. The response for the synchronous reactance Matlab model and control design is shown in Figure 6.10:

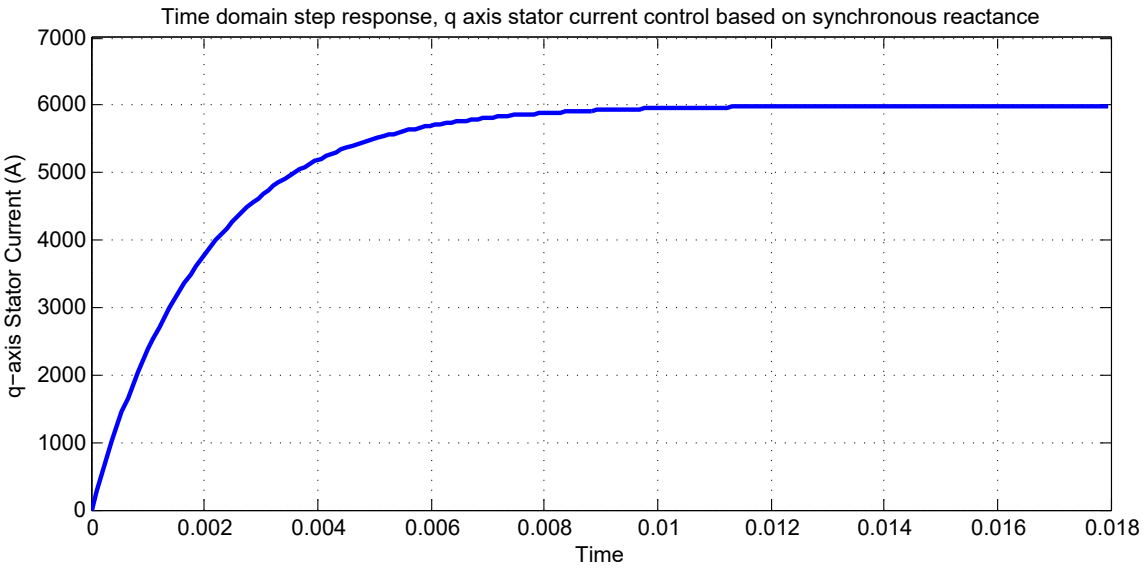

Figure 6.10: Matlab q-axis current step response.

Stability of the Quadrature-Axis Stator Current Control

As done for the d-axis stator current control, a total delay time $T_d = 0.3\,ms$ is considered and the gain and phase margins are obtained via Matlab. The results are exactly the same, as the control design criterion and total delay time are the same, that is: both gain margin (infinite) and a 85.5° phase margin indicate a closed-loop stable system.

6.2.3 Field Current Control

There are multiple ways of integrating field current control in a vector-oriented controlled synchronous machine. In the first place, it depends upon which flux-linkage orientation is being used. Reference [83] presents an example of such a control focusing on the stator-flux linkage, [85] detailedly describes control using air-gap flux oriented control. In both cases the field current value is not directly controlled but becomes a consequence of the desired flux value. Using flux as the controlled variable is related to improved dynamical behavior if compared with the strategy of simply using field current control [83]. In this work limitations of the excitation system are taken into account.

Figure 6.11 shows the basic idea of field current control as implemented in PSCAD/EMTDC. Previously, it was commented that there are two usual bases for field circuits, the L_{ad}-reciprocal base and the non-reciprocal one. The synchronous machine model of PSCAD/EMTDC outputs i_F in the L_{ad}-reciprocal base and expects a voltage input E_F in the non-reciprocal one, therefore, a change of base is necessary.

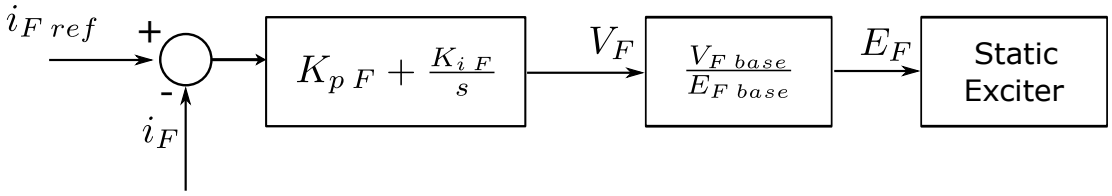

Figure 6.11: Field current control.

To advance in the control design, the closed-loop diagram block shown in Figure 6.12 is used,

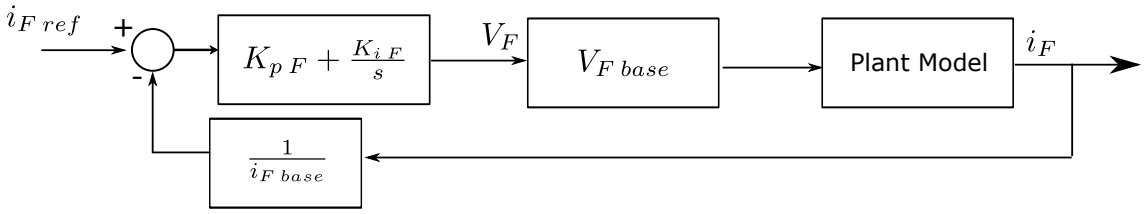

Figure 6.12: Field current control block diagram.

Because the machine rotor effectively behaves in different ways for different kinds of responses, field current control could be implemented taking into account different electrical time constants for the plant model. Employing T'_{do}, for example, is considered to be enough for the design of excitation control in regular hydro plants [143] and that is the criterion used here. The controlled plant for this control loop is given by:

$$\frac{i_F(s)}{V_F(s)} = \frac{1}{r_F + s\,(L_{ad} + L_F)}. \tag{6.9}$$

The procedure is the same one followed for stator current control. The choice of field current control closed loop bandwidth must be based upon the circuit and excitation system characteristics. It is expected that the field current control should have a considerably slower response in comparison to those of stator currents, given that the rotor field inductance is considerably larger [91].

A static excitation system is capable of bidirectional voltage input in the field circuit, but its voltage ceiling is usually in the range of hundreds of volts [144]. Increasing this level to the range of a few kV is possible and can be found in operational synchronous machine, but care must be taken regarding insulation levels [145]. This could present an obstacle in the retro-fitting of existing FS-PHS with decades old synchronous machines. There is also the delay added by the excitation system, which is in the range of milliseconds for static exciters [146]. Based on what has been found in the literature, the static exciter is modeled as a first-order filter with a 2 ms time-constant [143] and is part of the "Plant Model" shown in 6.12. In this initial control design no considerations about the ceiling voltage are present. In the next sections, when complete simulations are performed, the comparison be-

tween the imposed excitation voltage and usually possible ceiling voltage levels is presented.

The chosen bandwidth is $\alpha = 15$ rad/s. Applying this to (6.4) and (6.5) leads to: $K_p = 0.0478$ and $K_i = 0.2439$ s^{-1}. Figure 6.13 shows the response for both PSCAD and Matlab models. Once again a difference between models is expected, for the same reasons of the stator current case, and also due to the presence of disturbances such as direct axis damping current i_D, as shown by (3.15). The effects of such disturbances into the air-gap flux linkage is discussed further in in the flux control section.

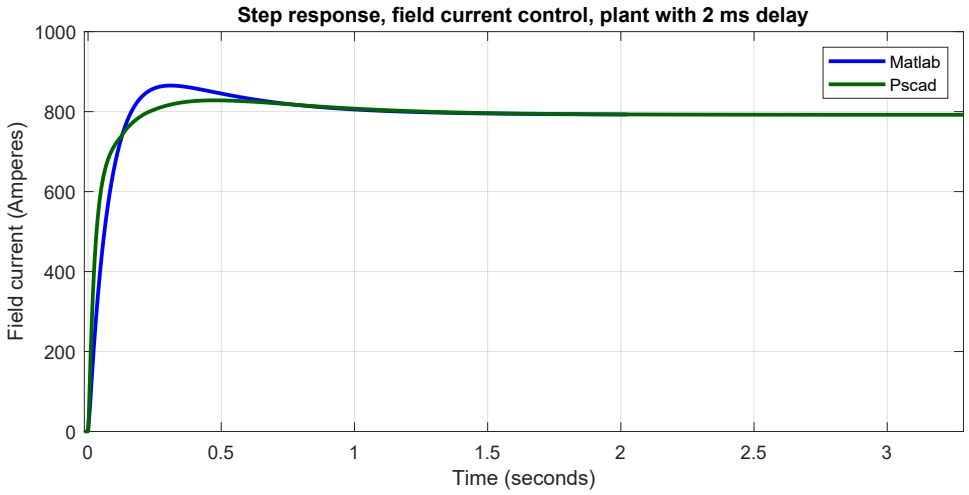

Figure 6.13: Field current control step response using T'_{do} as plant transfer function.

The frequency response diagram of Figure 6.14 shows that the desired bandwidth has been obtained with a phase margin of 80^o.

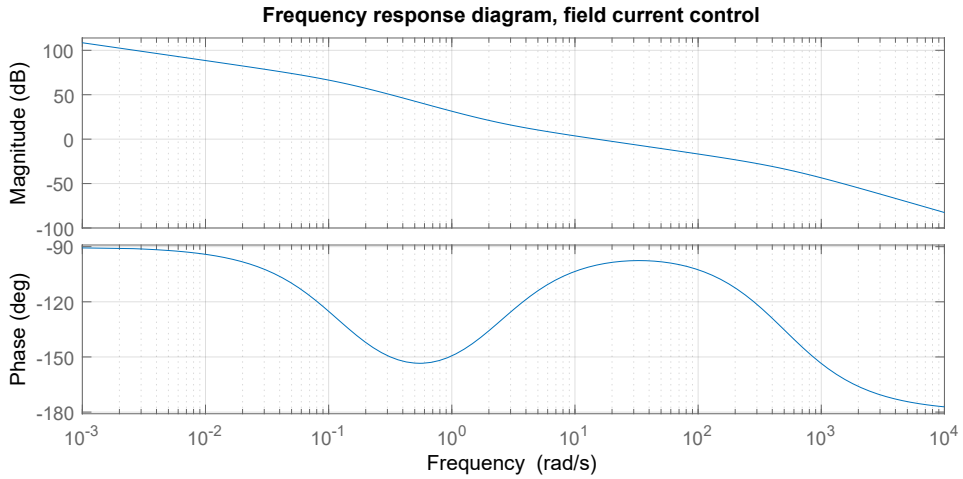

Figure 6.14: Field current control frequency response.

6.2.4 Direct Axis Air-Gap Flux Control

Air-gap flux and field current control loops are nested, as shown in Figure 6.15. As a well known control procedure, the outer control loop must be slower than the inner one [86] [91]. The criterion here is to define a flux control bandwidth 4 times smaller than the closed field current control loop one [91]. This results in $\alpha_\phi = 3.75$ rad/s. Disregarding the stator current i_d and the damper circuit current i_D contributions shown in (3.15), the air-gap flux control plant model is:

$$\frac{\lambda_{ad}}{i_F} = L_{ad}. \tag{6.10}$$

In this case, the main control objective is disturbance rejection, as the air-gap flux reference remains constant, except for flux weakening regions. Using the closed loop transfer function of field current control obtained previously and using Matlab *pidtune* options, the following PI-controller gains are defined: $K_p = 0.0$ and $K_i = 3.3$ s^{-1}.

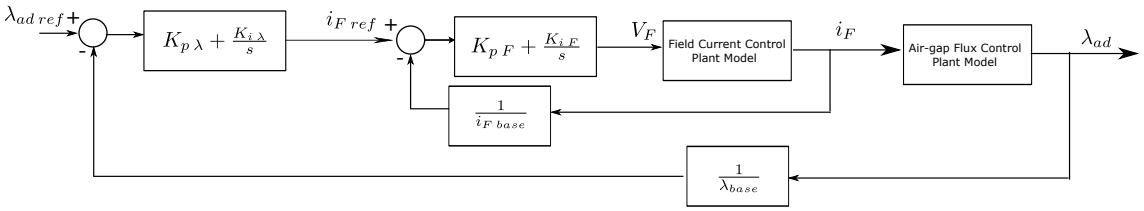

Figure 6.15: Direct-axis air-gap flux control modeling.

Disturbance rejection becomes important, as stator d-axis current i_d and damper winding current i_D interfere with the air-gap flux linkage. Thus, the control scheme implemented presents feed-forward terms, as shown in Figure 6.16.

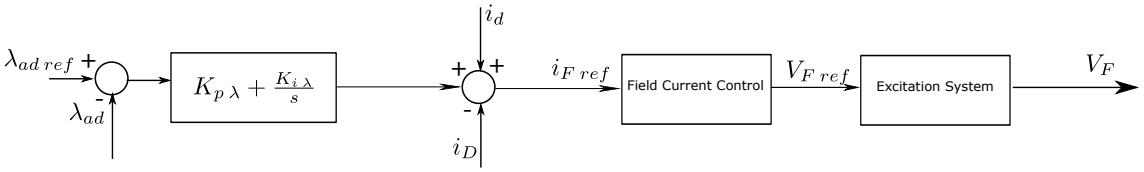

Figure 6.16: Direct-axis air-gap flux control structure

The step response of the designed control system in both PSCAD and Matlab is shown in Figure 6.17:

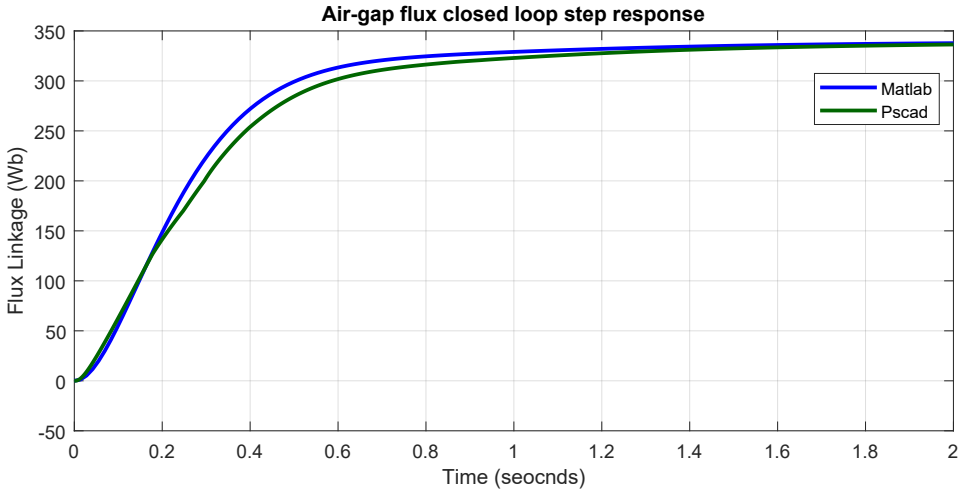

Figure 6.17: Direct-axis air-gap flux step response, with disturbance rejection on the PSCAD simulation response.

Figure 6.18 shows the effect of disturbance rejection via feed-forward term. A unitary step reference is given for i_d control while air-gap flux reference is constant. In practice, as shown ahead, such sharp reference changes for i_d are not common and, thus, this is a pessimistic scenario. With feed-forward, the controlled flux returns in less than 0.1 seconds to 95% of the reference value.

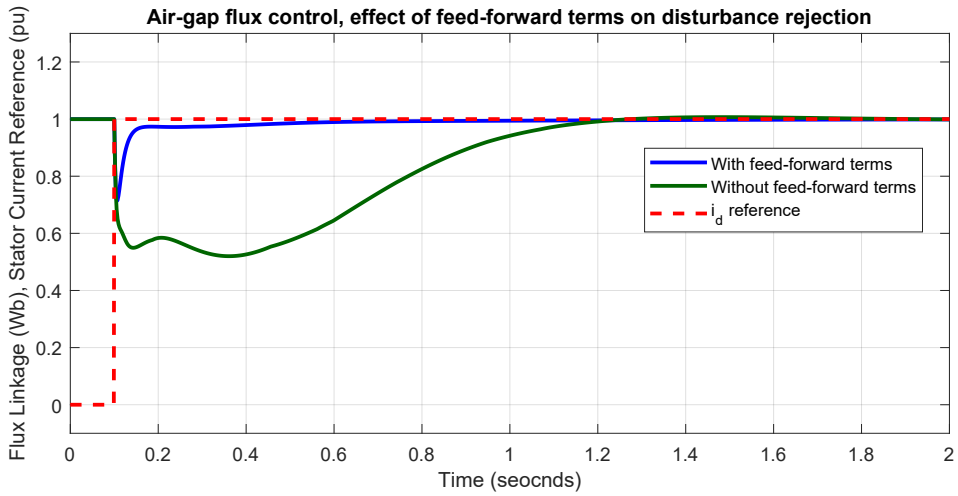

Figure 6.18: Direct-axis air-gap flux step response, with disturbance rejection on the PSCAD simulation response.

A first investigation on the excitation system behavior is done, an initial ceiling of 2.1 kV is set for V_F and a PSCAD case test with the two pessimistic scenarios, a unitary step in λ_{ad} reference and, 4 seconds later, a unitary step in the i_d reference. Figure 6.19 shows that, for both cases, V_F remains within the chosen ceiling voltage boundary. As shown in Chapter 7, for the disturbances and reference changes that actually take place during operation, this ceiling could be even lower.

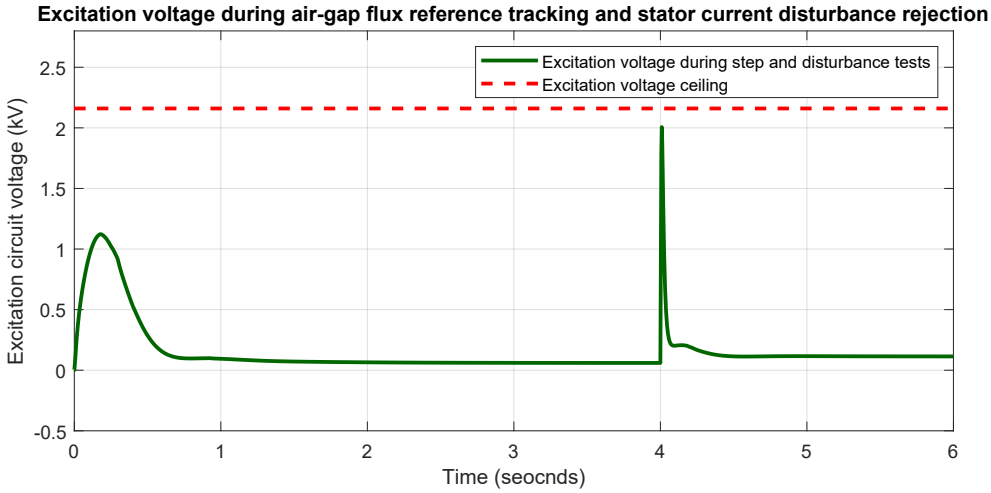

Figure 6.19: Excitation voltage during both air-gap flux reference tracking and stator current disturbance rejection.

6.2.5 Speed Control

In the case of speed control using purely PI-controllers, obtaining fast response without overshoot is not feasible [147]. For this loop control, therefore, the addition of a Two-degree-of-freedom (2-DOF) PI is necessary for a better performance [147]. This leads to the control structure shown in Figure 6.2.5:

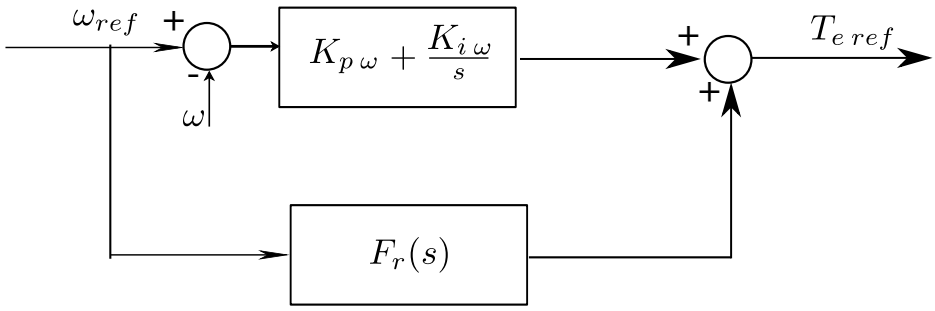

Figure 6.20: Conceptual block diagram of the speed control.

For the design of the structure related to the 2-DOF PI, the following equation, derived in [147], is used:

$$F_r(s) = \frac{J\alpha_\omega \left[(m-1)s - \frac{\alpha_\omega}{4\zeta^2}\right]}{s + m\alpha_\omega}, \tag{6.11}$$

where α_ω is the desired bandwidth for the closed loop speed control, ζ is the desired damping, and m is a parameter to be set. By setting $m = 1$, the same load-torque rejection and measurement noise amplification of the regular PI design are attained. By using this criterion, the transfer function shown in 6.11 becomes the first-order

filter:

$$F_r(s) = -\frac{J\frac{\alpha_\omega^2}{4\zeta^2}}{s+\alpha_\omega}. \tag{6.12}$$

For the speed control, the K_p and K_i constants are set as [147]:

$$K_p = J\alpha_\omega \tag{6.13}$$

$$K_i = J\left(\frac{\alpha_\omega}{2\zeta}\right)^2. \tag{6.14}$$

The data of interest to perform this tuning comes from Table 4.3. In per-unit, $J = 2H$ [84], so $J = 5.6$ pu. The desired bandwidth is set to 1.5 rad/s. Inserting these values into (6.12), (6.13) and (6.14) yields $F_r(s) = -\frac{3.14}{s+0.004}$, $K_{p\omega} = 8.4$ and $K_{i\omega} = 3.3$ s^{-1}. As shown in Chapter 2, the range of speed of the pump is 0.15 pu. Therefore, the step response given to the PSCAD model in order to test this control loop is within the nominal speed range (0.8 pu to 0.95 pu).

Figure 6.21 shows the response of the PSCAD model to this reference step when the wicket gates are completely closed, that is, the machine is spinning without propelling water. A comparison is shown between the case with and without 2-DOF PI. As expected, the addition of the filter $F_r(s)$ gives a response with smaller overshoot.

Figure 6.21: Speed control with and without 2DOF-PI. PSCAD PHS model with closed wicket gates (G = 0)

.

Now the same result is shown for the case with fully opened wicket gates ($G = 1$) in Figure 6.22. This is important to confirm that speed control, that has been designed considering only the machine inertia and disregarding the mechanical torque produced by the hydraulic circuit as a disturbance, works properly for multiple gate positions. The power developed by the pump P_p is also shown, it is observable that,

for $\omega = 0.95$ pu, P_p is close to 1.0 pu, as expected from the hydraulic circuit model described in Chapter 2. The initial value, between 0.3 and 0.35 pu is also very similar to the expected from Figure 2.8. From the point of view of speed control, there is a difference, as the response takes longer to actually reach the final value due to the mechanical nature of the disturbance. This configures no problem for the general control structure, as shown in the next subsection describing the outermost control loop, related to the mechanical power.

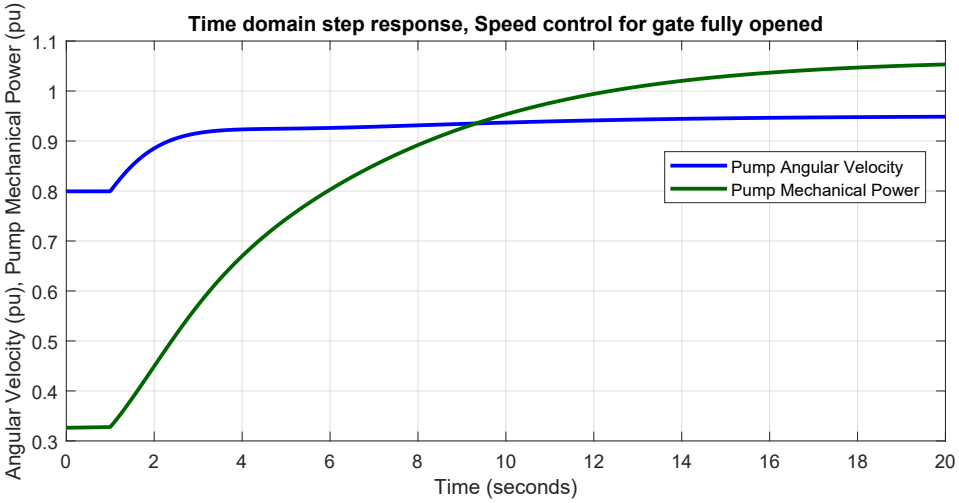

Figure 6.22: Step response of speed control with 2DOF-PI. PSCAD PHS model with opened wicket gates (G = 1)

.

6.2.6 Power Control

To design power control it is necessary to employ the transfer function (2.16) developed in Chapter 2 and rewritten below:

$$\Delta P_m = \frac{A(s\,T_w + 1)}{(s\,T_w - B)^2}\Delta\omega.$$

As previously discussed, this equation is linearized around a certain point (ω_0, Q_0). By observing the relationship between flow and speed shown in Figure 2.8 and considering that a pump speed standing approximately in the middle of the operating range is a good choice, the point chosen to design power control is $(\omega_0 = 0.9 \text{ pu}, Q_0 = 0.9 \text{ pu})$. The control loop can be represented as depicted in Figure 6.23.

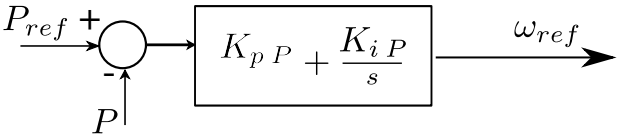

Figure 6.23: Power control loop representation

.

By using the *pidtune* options of Matlab and choosing a bandwidth of 0.5 rad/s, the PI is tuned in the following manner: $K_{pP} = 0.536$ and $K_{iP} = 0.111$ s^{-1}. To verify the performance of this design, a power order step of 70 MW is given to both the PSCAD and MATLAB PHS models. The 70 MW value represents the operational range of the PHS as developed throughout this work and shown in Chapter 2. The results of these reference steps are shown in Figure 6.24. In both programs the response follows the expected settling time for the chosen bandwidth. Also, the validity of the developed transfer function is confirmed, as both PSCAD and Matlab models behave in a similar manner.

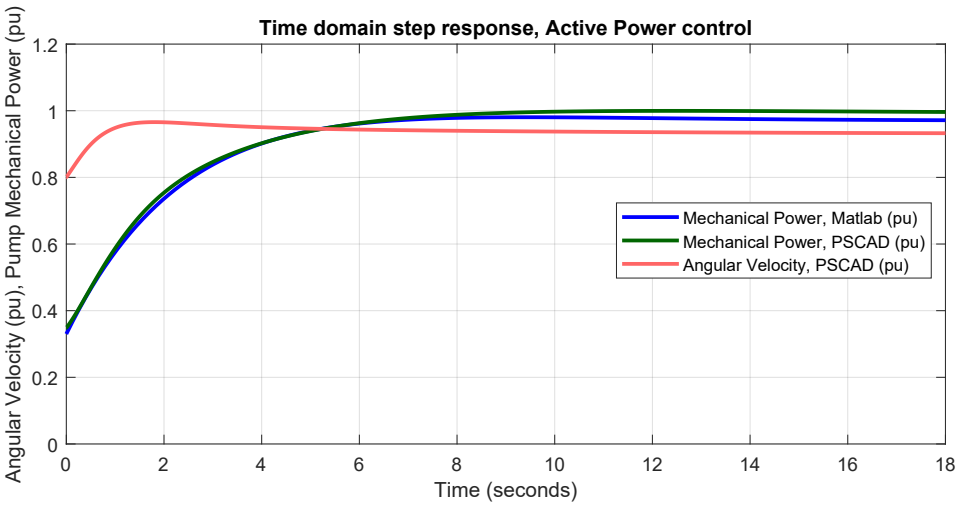

Figure 6.24: Response to a step reference change of 70 MW applied to the power control loop, both in PSCAD and Matlab environments.

In practice, no frequent step changes of that magnitude in power reference are expected, for such sudden torque variations can cause stresses to the synchronous machine's shaft and decrease its lifespan, so a rate limiter is added to any order step in the final model.

6.2.7 Circulating Current Suppression Control

As described in Chapter 3, it is usual to control the alternating circulating current values inside the MMC. More specifically, the second-harmonic circulating current is usually suppressed in HVdc applications. In the present work, as discussed in Chapter 3, circulating current control serves two purposes:

- To follow a reference for circulating currents, during the start-up procedure;
- To suppress the double frequency circulating currents, when under normal operation.

To fulfill these tasks, the control structure shown in Figure 6.25 is built and the reference variables ($i_{c\,d\,ref}$ and $i_{c\,q\,ref}$) are appropriately chosen:

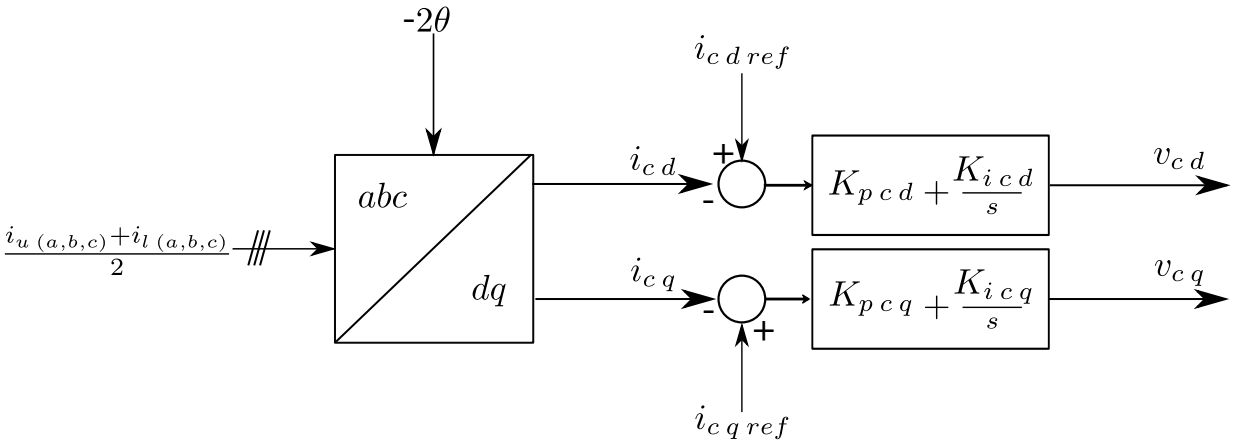

Figure 6.25: Circulating Current Supression Control structure.

The PI controllers shown in Figure 6.25 are designed as described by Tu et al. [142]. The relationship between the references for $v_{c\,d,q}$, both shown in Figure 6.25, and the circulating currents $i_{c\,d}$,$i_{c\,q}$ is given by:

$$\begin{aligned} v_{c\,d} &= L_{arm}\frac{di_{c\,d}}{dt} - 2\omega L_{arm} i_{c\,q} + R_{arm} i_{c\,d} \\ v_{c\,q} &= L_{arm}\frac{di_{c\,q}}{dt} + 2\omega L_{arm} i_{c\,d} + R_{arm} i_{c\,q}. \end{aligned} \tag{6.15}$$

Just as in the case of output current control, the second term on the right-hand side of (6.15) gives rise to a feed-forward, decoupling term, and the PI-controllers can be designed using (6.4) and (6.5). The bandwidth is 500 rad/s, the same chosen for the output current control. This yields $K_{p\,d,q} = 0.4$ and $K_{i\,d,q} = 3.1$ s^{-1}. Figure 6.26 shows the effect of the designed CCSC. The detailed model of the MMC studied in this work is operating with active power flow of 0.86 pu and, at the simulation time t = 0.5 s, the CCSC is disabled. Clearly the amount of circulating current in the chosen reference frame (double frequency, negative sequence) suddenly increases, demonstrating the effect of the designed CCSC.

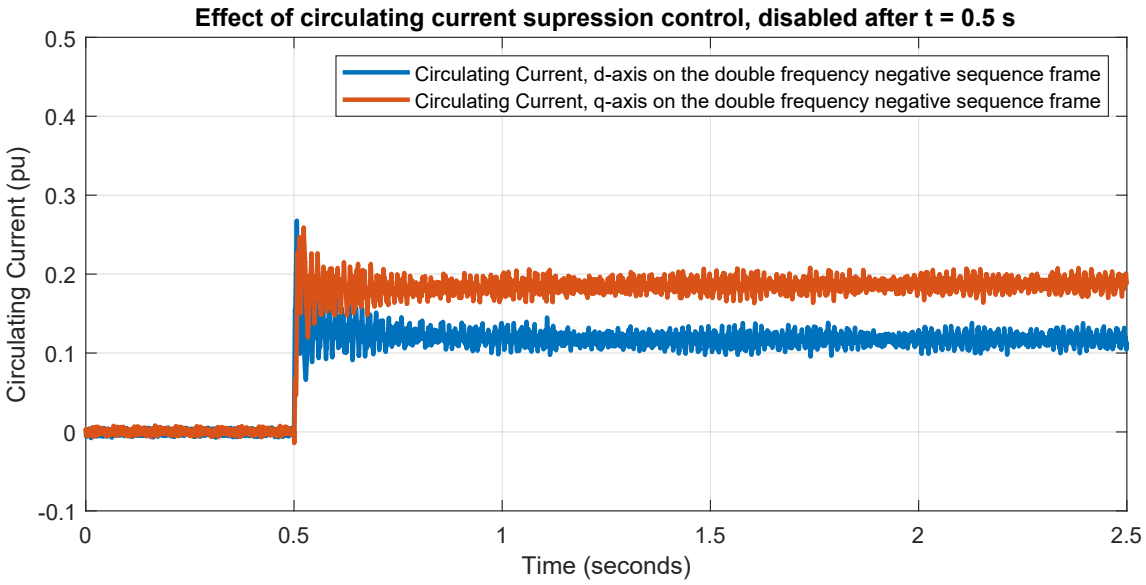

Figure 6.26: Effect of Circulating Current Supression Control shown by disabling it at t = 0.5 s.

6.3 Synthetic Inertial Response

It is possible to modify the power order given to the VS-PHS as function of network frequency deviations and, with that, allow the converter to provide some artificial inertial response to the power system [148]. The definition followed in this work is the one presented by Eriksson et al., that is: synthetic inertia implementation is fundamentally related to the ROCOF, and is based on the following relationship between active power and angular velocity variations, both in per-unit (e.g. [149]):

$$\Delta P_e = 2H\frac{d\omega}{dt}. \tag{6.16}$$

This response can be further complemented by a variation directly proportional to the deviation of the frequency in relation to its reference, what Eriksson defines as Fast Frequency Response (FFR). This leads to the general control structure shown in Figure 6.27:

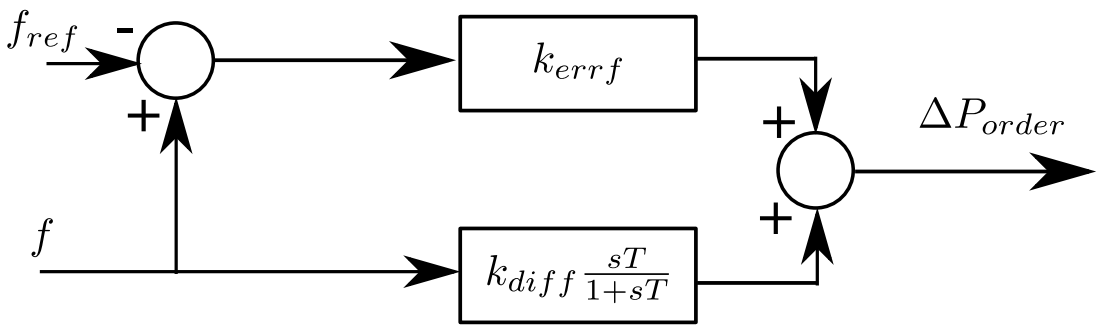

Figure 6.27: Synthetic Inertia Control Structure.

In the implementation done for this dissertation, the ΔP_{order} is given to both the machine-side converter and the grid-side converter.

6.4 Control of the Grid-Side Converter

The control of the grid-side converter can be considered, at least in its most basic form, to be simpler than the vector oriented control applied in the control of the synchronous machine. Figure 6.28 shows an overview of the control of the grid-side converter, considering only external variables.

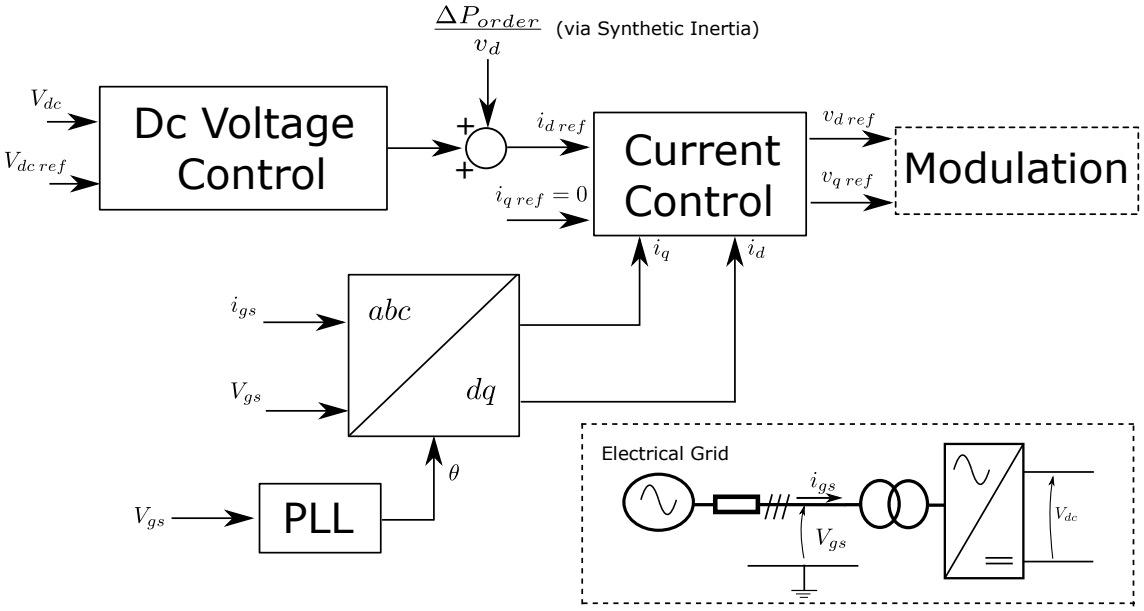

Figure 6.28: Power control loop representation

.

The control loops shown are well covered by the literature and a detailed description of them is beyond the focus of this dissertation. Some description and the control gain settings employed in the grid-side converter are presented in the Appendix B.

6.5 Chapter Conclusions

This chapter presents the design of the vector control of an electrically excited synchronous machine and how the possible different behaviors of this machine can affect the control design process. The general control structure contains cascaded control loops, requiring successively smaller bandwidths for the most external control loops. The speed control loop presented a superior performance with the use of

the 2-DOF PI controller, as proposed by Harnefors et al. [147]. In the direct-axis air-gap flux control, the superior performance of a feed-forward augmented disturbance rejection is presented. In terms of retrofitting feasibility, the possible limitation regarding the ceiling voltage of the synchronous machine exciter has also been reported and an initial investigation of this topic has been presented. This investigation will be complemented by the results presented in Chapter 7.

Chapter 7

Simulation Results

7.1 Start-up Procedure with Common-Mode Voltage Injection

As shown in detail in Chapter 3, the submodule voltage ripple of a modular multilevel converter tends to be unacceptably high when operation with low frequency is attempted and requires a special control strategy to properly work under such conditions. In this section, this strategy is tested via simulation with different common-mode voltage waveforms. The strategy is applied in such a way as to keep the SM voltages just below the maximum rated level of the employed IGCT. The start-up procedure follows the same structure of that applied in the operational experience with Grimsel 2 [53], as described in Chapter 4. The two common-mode voltage waveforms injected in each simulation are:

- Simulation a: smoothed square wave type, with A = 7.6 kV, ω_{cm} = 120 Hz and $\delta = 0.4$.
- Simulation b: Trapezoidal waveform, with same amplitude, frequency, and maximum dv/dt level of the smoothed square wave of Simulation a.

A third simulation, through which no low frequency control strategy is active is also performed and is henceforth referred to as Simulation c. Figure 7.1 shows the CMV waveforms related to Simulations a and b.

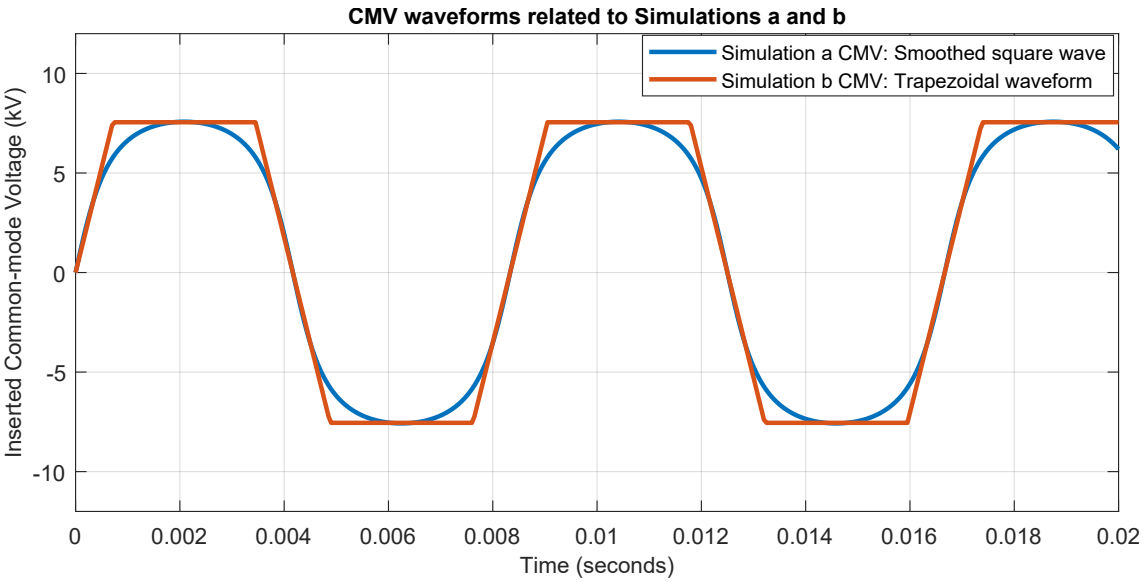

Figure 7.1: Common-mode voltage waveforms employed in Simulations a and b.

The results in this section is first presented with a focus on the period of machine acceleration, still with the wicket gate closed. This is the region in which the low-frequency control strategy is active and, therefore, focusing on it first allows to carefully observe and compare the MMC internal variables for different choices of CMV waveform. After that, results regarding the complete start-up procedure, that is, from standstill to fully opened wicket gates, is presented.

7.1.1 Results and Comparative Analysis

The first result presented is that of Simulation a. Figure 7.2 shows the capacitor voltage ripple of a single submodule of each arm of phase a of the MMC. This result was simulated by the author and published in [67]. It suffices to show a single SM per arm as the voltage of every SM is regulated to be the same by the sorting algorithm.

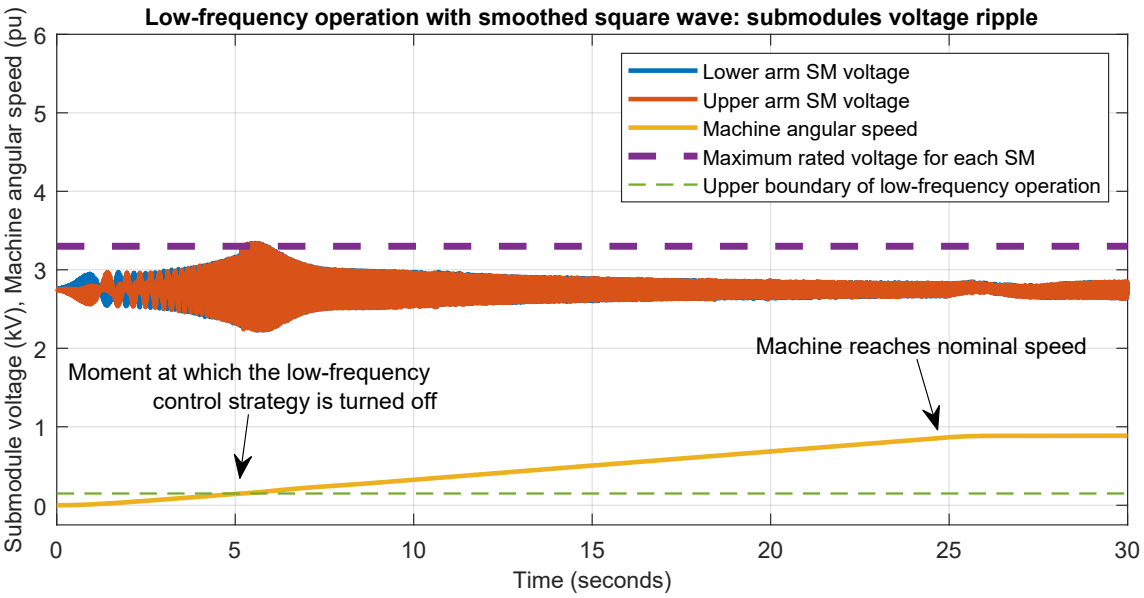

Figure 7.2: Capacitor ripple voltages for the case studied in Simulation a. ©2020 IEEE. Reproduced from [67].

Now, for comparison purposes, the results of start-up procedure without the low-frequency strategy (Simulation c) and those already presented (Simulation a) are superimposed in Figure 7.3.

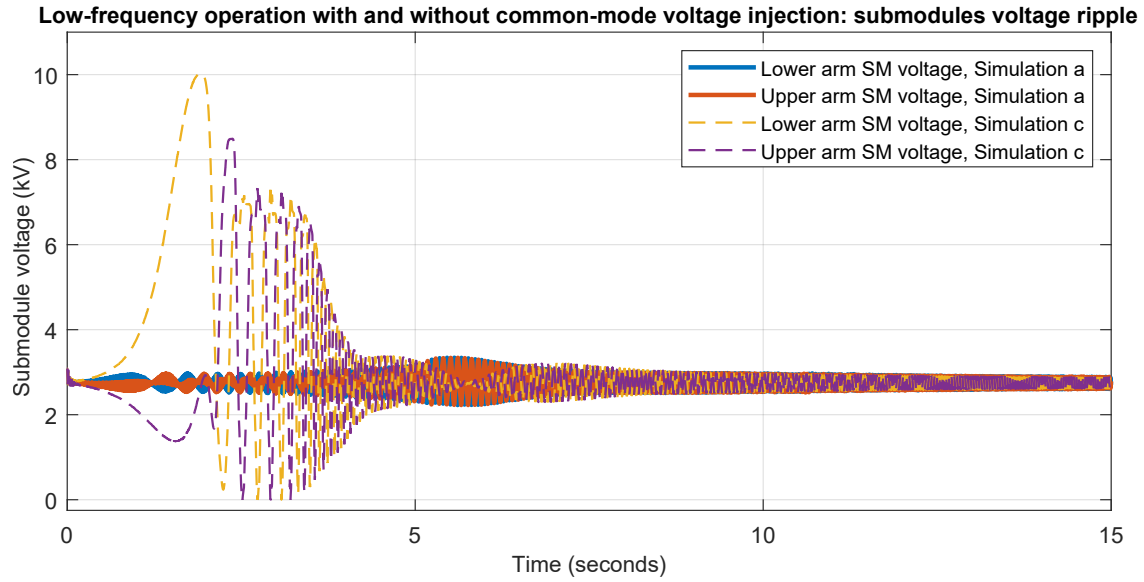

Figure 7.3: Capacitor ripple voltages for the case studied in Simulation a. ©2020 IEEE. Reproduced with modifications from [67].

The curves shown in Figures 7.2 and 7.3 lead to two immediate conclusions: it is necessary to employ the low-frequency strategy for the start-up procedure, without this scheme the MMC internal voltages become immediately unstable, reaching voltages of up to 10 kV. The second conclusion is that the proposed waveform as implemented is effective in the ripple suppression objective and compatible with the

strategy proposed by Jung et al. [103].

Now the comparison is done against Simulation b and shown in Figure 7.4. For better visibility, only the lower arm of phase a is shown.

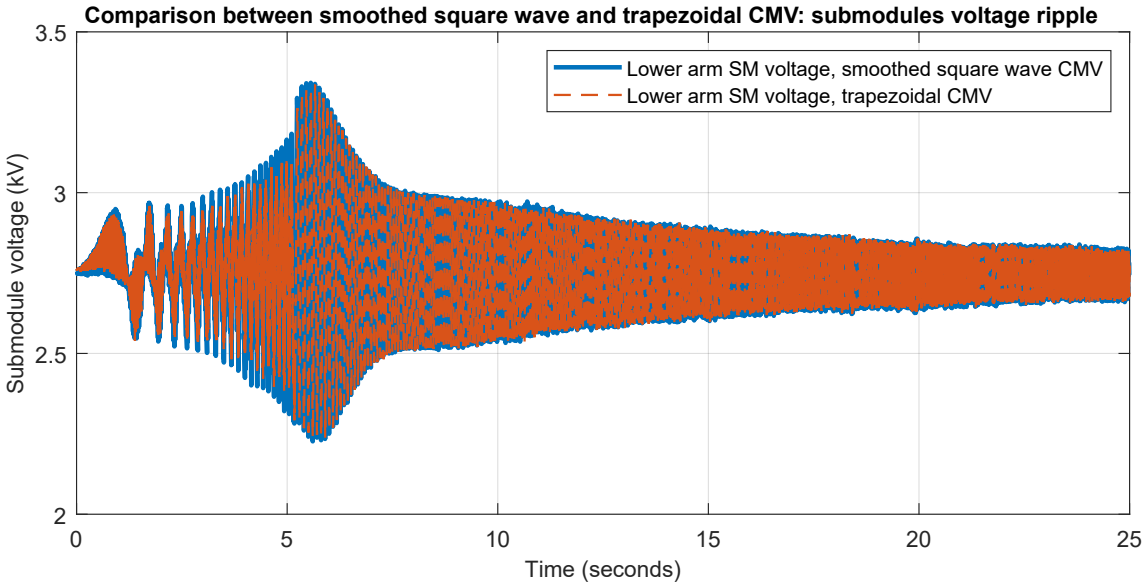

Figure 7.4: Comparison of capacitor voltage ripples for the cases studied in Simulations a and b. ©2020 IEEE. Reproduced from [67].

Figure 7.4 shows that the proposed smoothed square waveform application to the CMV, for this specific studied case, results in basically the same voltage ripple levels.

As previously discussed, sinusoidal waveforms as common-mode voltages are usually considered problematic due to their associated very high circulating currents, necessary to control the SM capacitor voltage ripple. It is important to observe the currents flowing through each arm during start-up in order to guarantee that these value are within the power semiconductor switches range of operation. Figure 7.5 depicts these results, it can be seen that every arm current stays within the IGCTs current ratings for Simulation a.

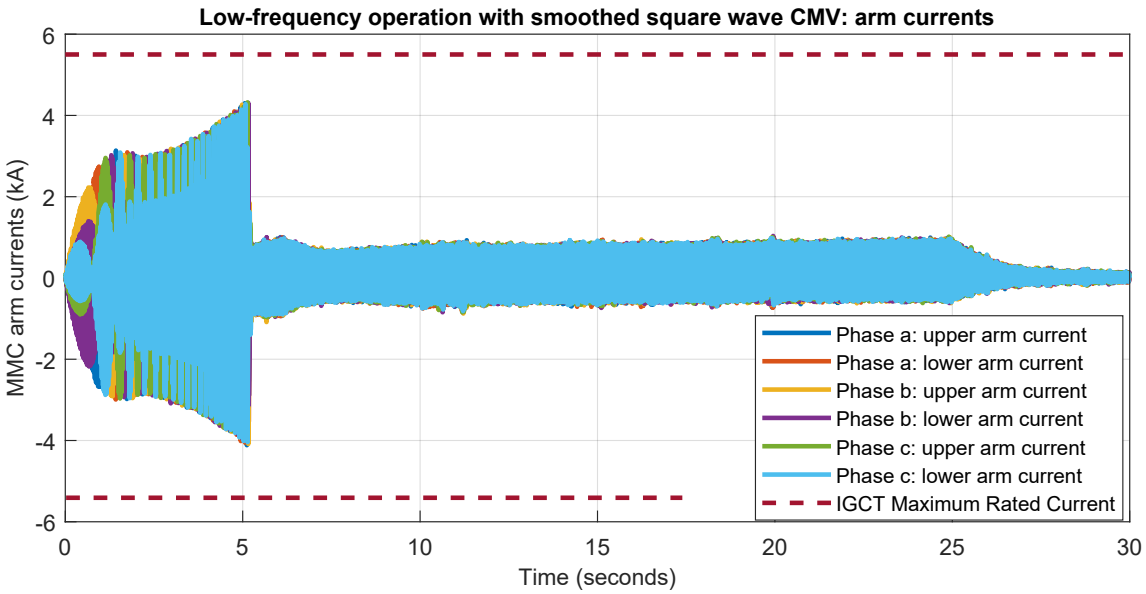

Figure 7.5: Arm currents during start-up procedure with smoothed square wave CMV injection. ©2020 IEEE. Reproduced from [67].

Now a comparison between Simulations a and b is presented in Figure 7.6, so the increase in circulating currents between trapezoidal and smoothed square CMVs is observed. Figure 7.5 has previously shown that, for a certain simulation, the current levels are the same between the MMC arms, so, to facilitate the comparison, only a single arm current (phase a: upper arm) is plotted for each simulation.

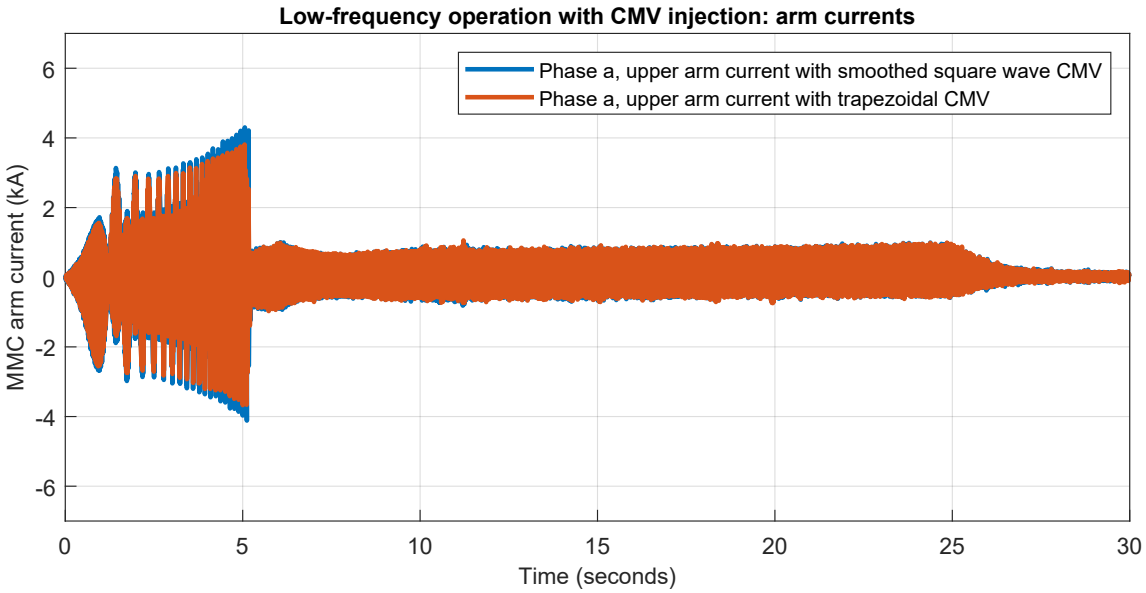

Figure 7.6: Comparison of MMC arm current level during start-up for trapezoidal and smoothed square-wave CMV. ©2020 IEEE. Reproduced from [67].

The graphs presented in Figure 7.6 show that the arm currents do indeed increase with the proposed waveform if compared with the trapezoidal waveform. This increase is of 11.25% in the studied case, and the current values are within the IGCT

rated values and, therefore, this increase probably causes no hindrances related to the reliability of the converter. Some level of increase was expected, as it is known that there is an inverse relationship between the employed waveform's RMS value and the amount of circulating currents during the application of the low-frequency operation strategy [150].

The MMC low-frequency operation strategy leads to extra harmonic frequencies into the dc-link [105]. Figure 7.7 shows the dc link voltage for both Simulation a and b, in both waveforms there is an increase in the dc-voltage ripple while the low-frequency control technique is active. Comparatively, though, there are only slight differences between the simulations employing the different waveforms.

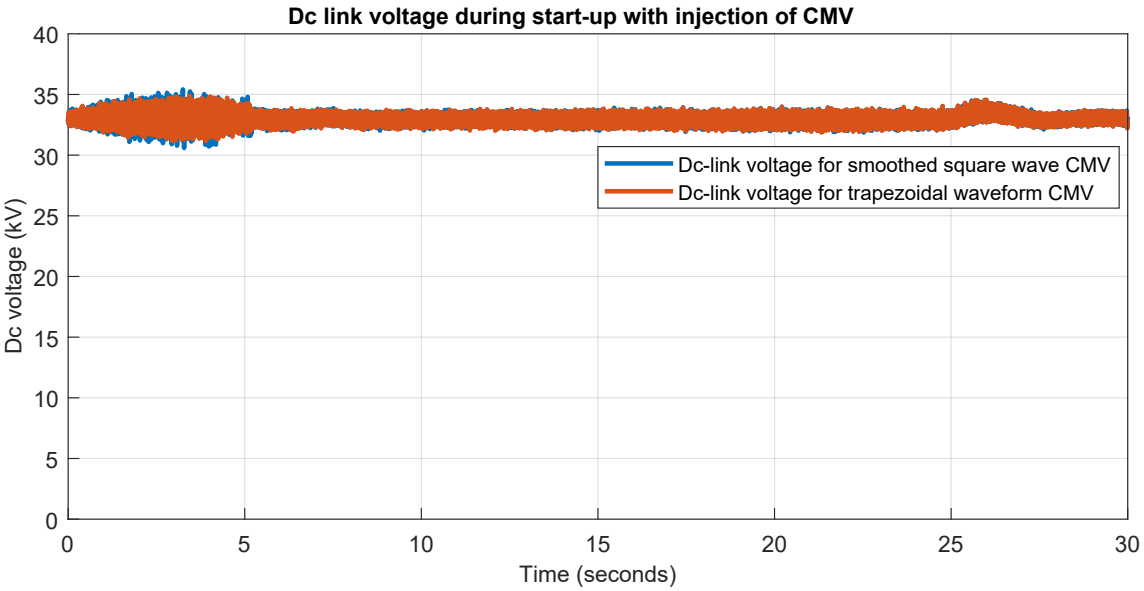

Figure 7.7: Comparison of MMC arm current level during the PHS start-up, for trapezoidal and smoothed square-wave CMV options. ©2020 IEEE. Reproduced from [67]

Figure 7.8 shows phase-neutral voltage of phase a during the start-up based on smoothed-square CMV. This figure confirms that the injected common-mode voltage does not appear in the external phase-neutral voltage of the converter. The phase-neutral voltage behaves exactly as expected during the start-up of the machine, slowly ramping up even though there is a common-mode voltage with peak voltage of approximately 7 kV being injected.

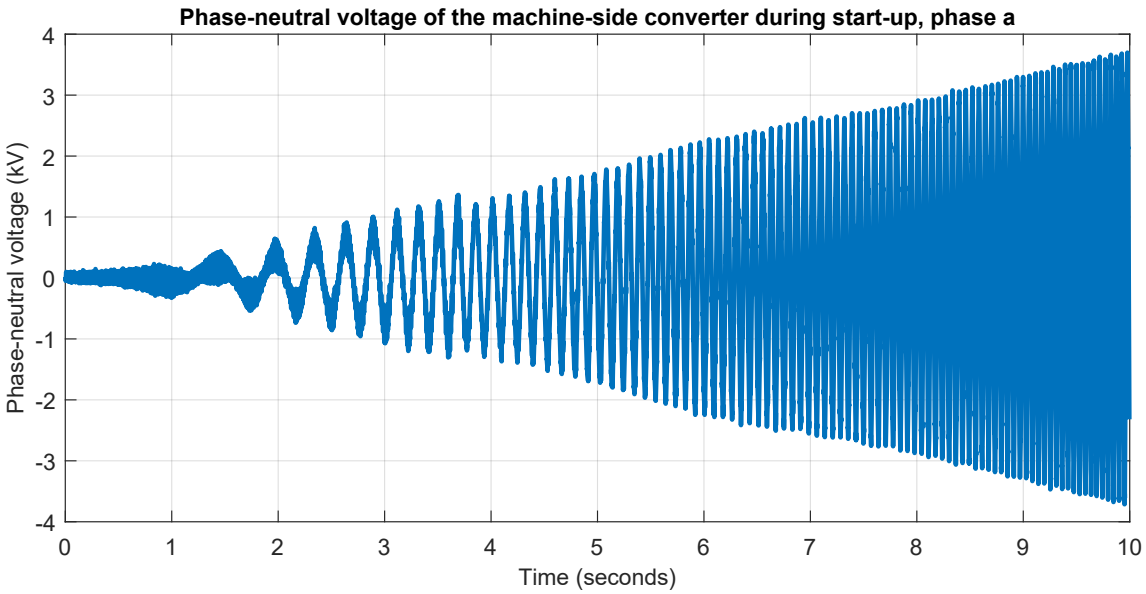

Figure 7.8: Phase neutral voltage of phase a during PHS start-up with CMV injection.

Figure 7.9 presents the variables behavior during the complete start-up procedure. Complete start-up procedure is here defined as beginning with the machine on standstill and ending with the machine in the nominal speed range and with fully opened wicket gates. The CMV applied is the smoothed square wave.

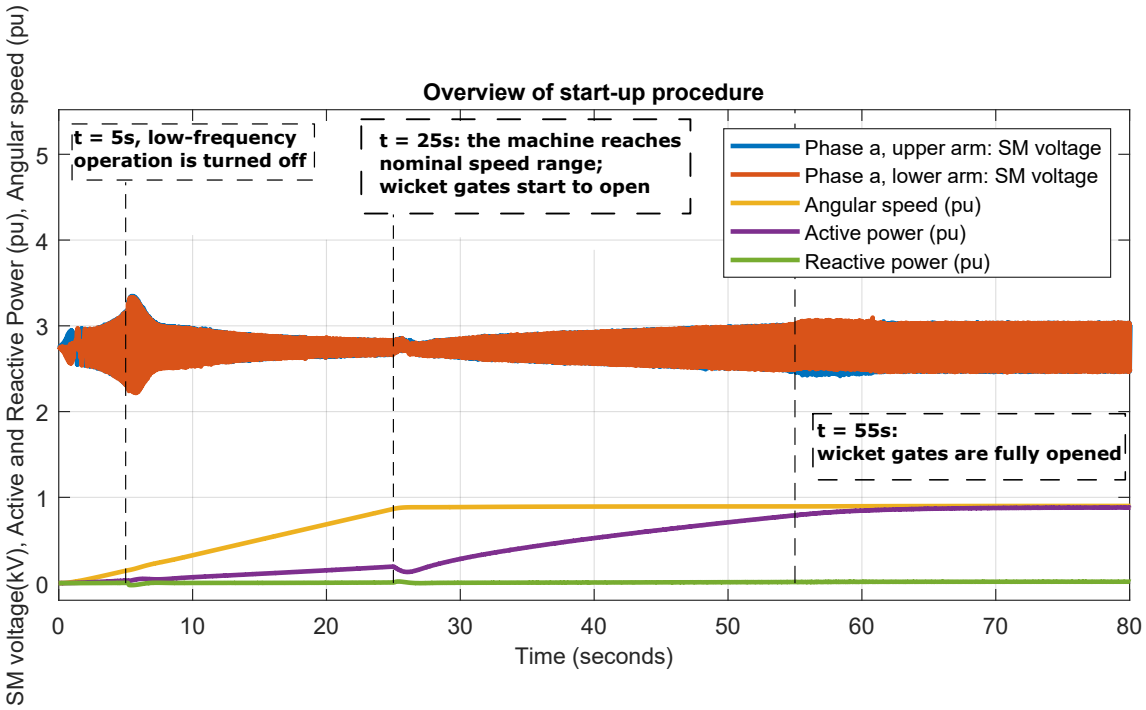

Figure 7.9: Overview of the complete start-up procedure. ©2020 IEEE. Reproduced from [67].

There are some points of special interest to be observed on Figure 7.9, one of them is that the voltage of the submodules' dc-capacitors, including the ripple, remain within the 3.3 kV range throughout the whole simulation. This remains true even by the end of the starting procedure, when an active power flow of almost 1.0 pu is already taking place. Also, the MTPA technique effectively maintains the power factor of the machine very close to unity, as the reactive power in practically null. Finally, the speed order is followed smoothly, without any sort of disturbances on the machine speed even while CMV is being injected.

7.2 Synthetic Inertia Response

As described in Chapter 4, the simulation performed to observe the synthetic inertia response during pumping mode consists in the loss of two out of three circuits of an intertie within the 11-bus test system. At steady-state, there are approximately 1800 MW flowing through this intertie. In this section the effect of synthetic inertia in the system as a whole is studied. Subsequently, the effects of synthetic inertia into the MMC internal variables are investigated and it is observed if, for that example case, any of the main-circuit rating limits are breached. Two simulations are performed, one at which the synthetic inertia is deactivated and the other where it is not.

Anderson and Fouad [89] define an inertial center and a mean frequency for a power system, this concept is going to be employed in this section as the way of quantifying the synthetic inertia's contribution to the power system's overall inertial response. This mean frequency is defined by:

$$\bar{\omega} = \frac{\sum \omega_d H_d}{\sum H_d}, \tag{7.1}$$

where d the index of a certain synchronous machine connected to a system. In the case studied here, $d = 1, 2, 3$.

The angular speeds of each of the three synchronous machines of the 11-bus test system, obtained for both the cases with and without synthetic inertia, and their respective inertia constants, are then applied to (7.1). The resulting mean frequency $\bar{\omega}$ comparison is shown in Figure 7.10.

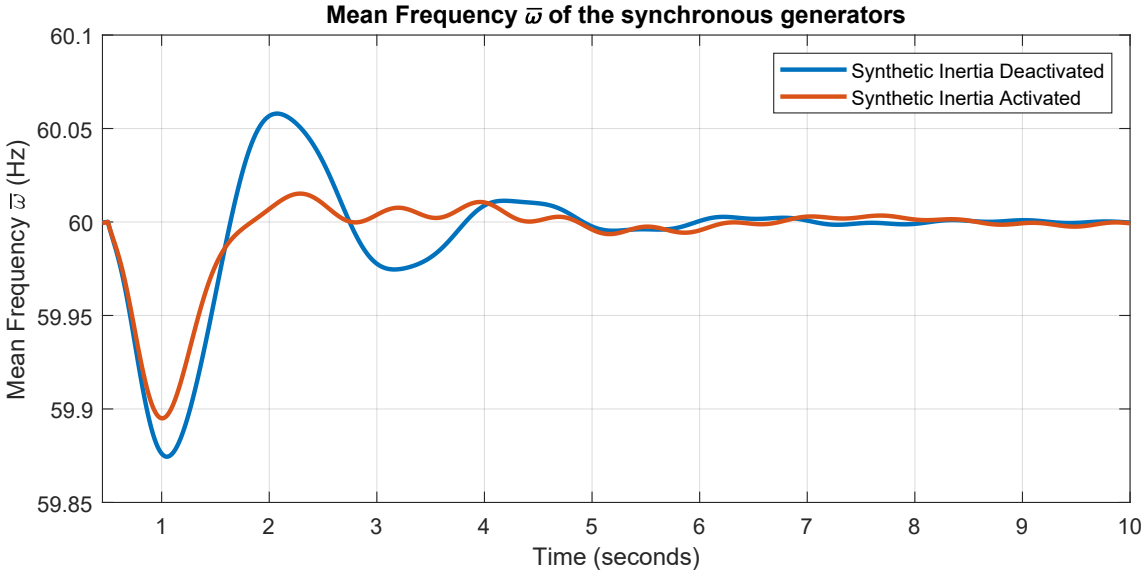

Figure 7.10: Frequency variation of the 11-bus system synchronous machines.

As expected, the frequency obtained through this criterion shows an improved inertial response for the simulation where VS-PHS has the synthetic inertia activated, with improved frequency dip and nadir. To quantify this improvement, the maximum absolute value of ROCOF for both curves shown in Figure 7.10 has been estimated and the results are shown in Table 7.1:

Table 7.1: Estimated rate of change of mean frequency for the cases with and without Synthetic Inertia.

Case	**Max. absolute rate of change of $\bar{\omega}$ (Hz/s)**
Synthetic Inertia Deactivated	0.343
Synthetic Inertia Activated	0.305

Therefore, the provision of synthetic inertia has caused a reduction of rate of

change of frequency of 11.08%. That is, activating synthetic inertia of an 800 MW large-scale energy storage improves the inertial response of this specific system, for this specific contingency, in approximately 10%.

Figure 7.11 shows how the synthetic inertia control makes the VS-PHS quickly modulate its power consumption, leading to a decrease of, approximately, 300 MW, in less than 1.0 second.

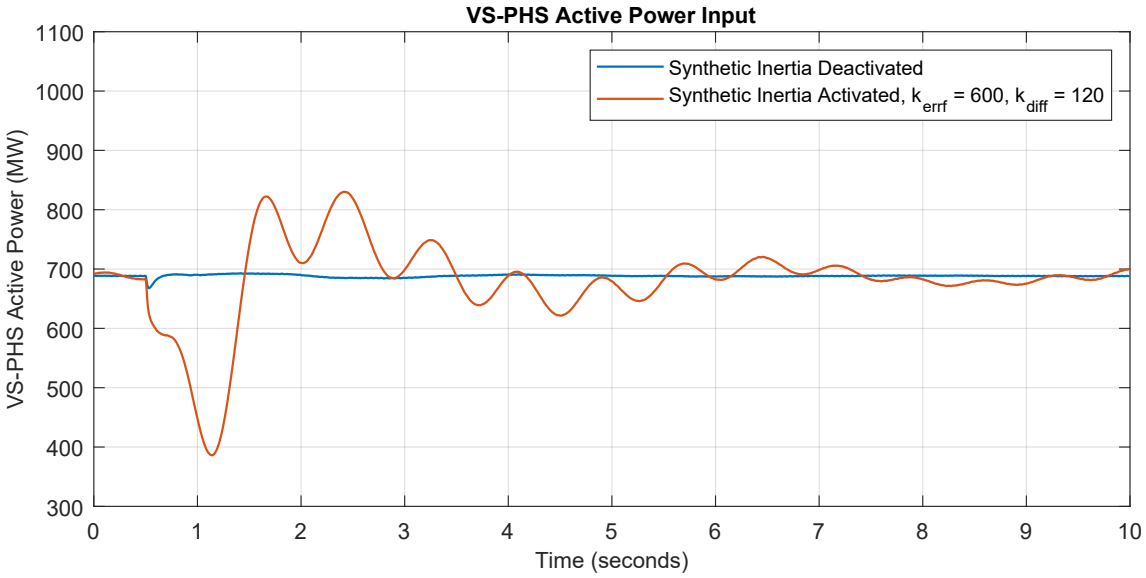

Figure 7.11: PHS active power output, with and without synthetic inertia.

Clearly there is an overshoot in terms of active power output, which dampens the frequency overshoot shown in the case without inertia. It is shown in the following Subsection 7.2.1, that this did not configure a problem to the current and voltage ratings of the converter components.

Figure 7.12 shows the variation in the power flowing through the intertie during the simulated contingency. There is an, approximately, 900 MW sudden power flow reduction and subsequent power oscillations, which are considerably damped in the case with provision of synthetic inertia and fast frequency response.

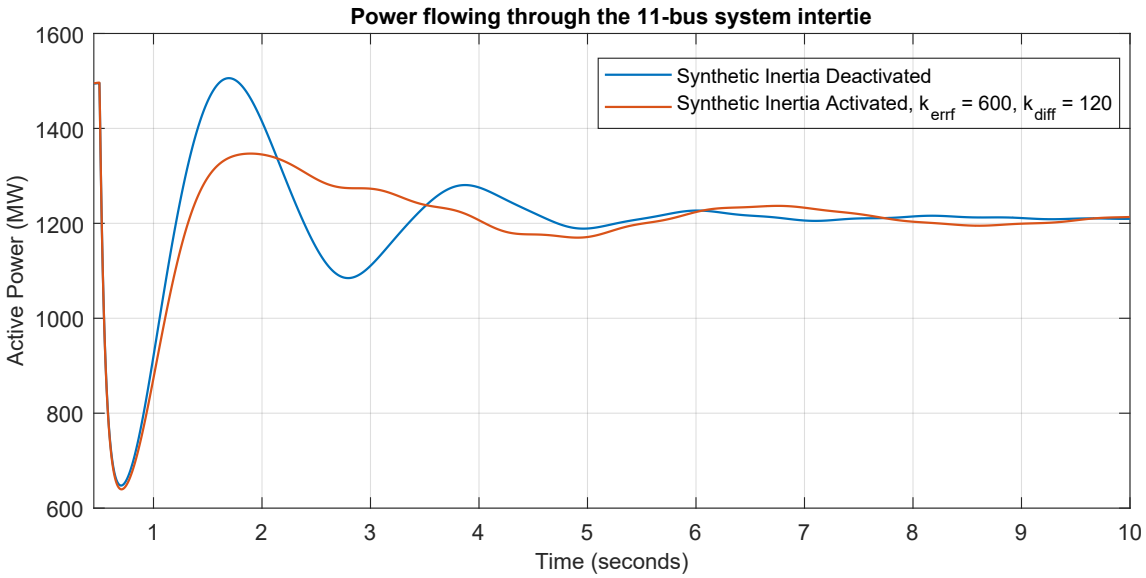

Figure 7.12: Power flowing through the intertie, during the contingency.

7.2.1 VS-PHS Internal Variables

It is important to investigate what are the effects of the synthetic inertial response of the converter, and the related active power flow variations, on the components of the VS-PHS unit. That includes the switching semiconductors of the MMC, the excitation system of the synchronous machine, the machine itself, and the hydraulic circuit.

Figure 7.13 shows the dc-voltage of a single, phase a, upper arm, MMC submodule, for both the grid-side and machine side converters. As shown, the submodule's dc-voltage oscillates but ultimately remains within the rated SM dc-link rated voltage. Discussion on the fundamental reason for these oscillations is presented further in the text.

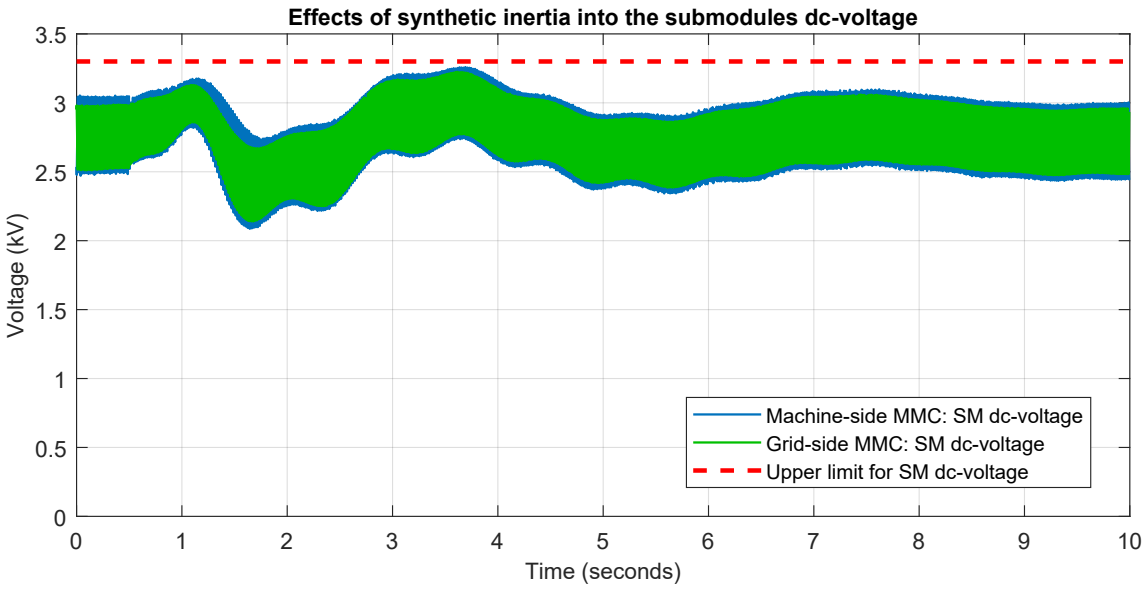

Figure 7.13: Submodules voltage at the machine-side and grid-side MMCs, during the active power variations triggered by the contingency and subsequent synthetic inertial response.

The current levels flowing through the power semiconductor switches during the contingency and their compatibility with the rated values are also verified. Figure 7.14 shows the current variations on the phase a, upper arm submodules of both the grid-side and machine-side converters. Clearly, in both cases the current remains well within the IGCT current rating until the variables return to steady-state conditions.

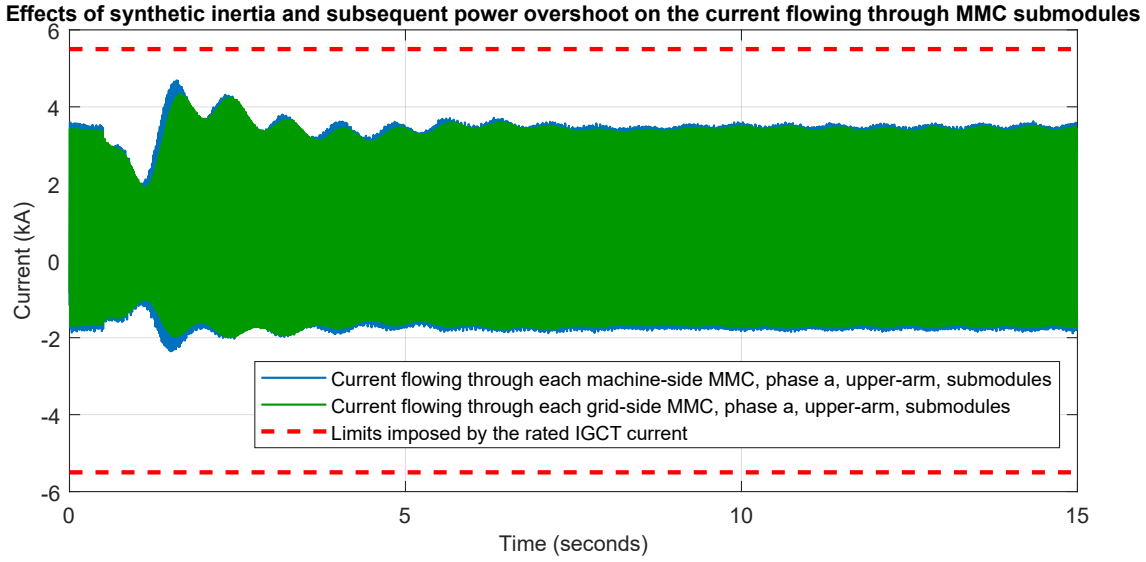

Figure 7.14: Currents flowing through the submodules of the machine-side and grid-side MMCs during the synthetic inertial response to the contingency.

Chapter 3 contains a discussion on the ceiling voltage of the excitation system of the VS-PHS synchronous machine. Figure 7.15 shows the behavior of the excitation

system voltage during the contingency, demonstrating that the initial rated value of 2.1 kV was not reached for this contingency and could be considerably reduced, this simulation presents strong evidence for the case of employing regular excitation systems in VS-PHS, without need for any increased ceiling voltage levels. This of course depends also on the desired performance of a given system for various contingencies.

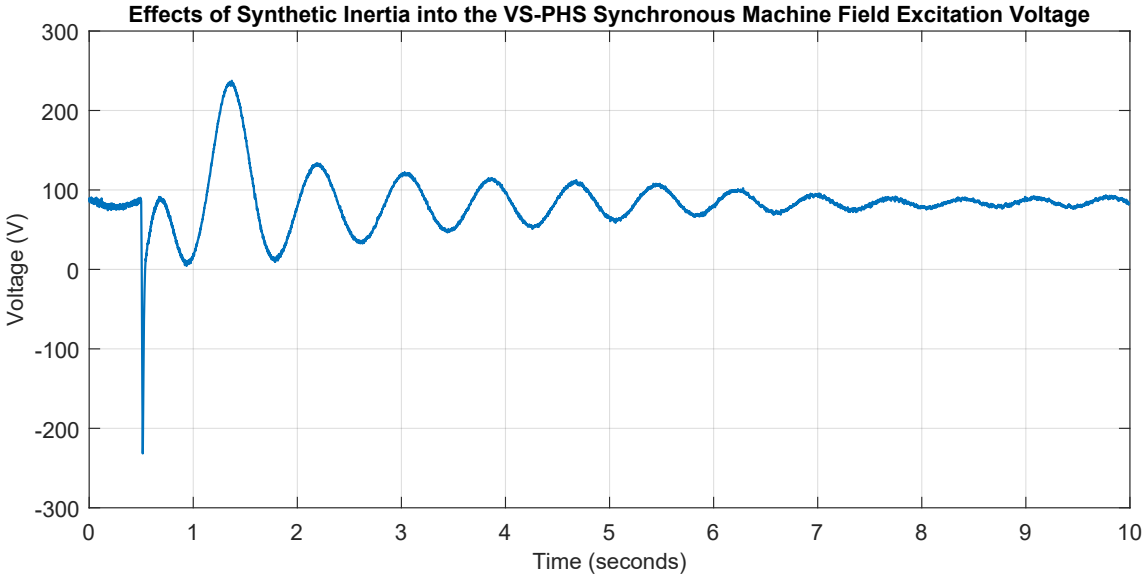

Figure 7.15: Voltage response of the VS-PHS synchronous machine excitation system.

The speed of the VS-PHS synchronous machines also goes through a transient. As shown in Figure 7.16 the speed sharply decreases, presents a small overshoot and then returns to its initial value.

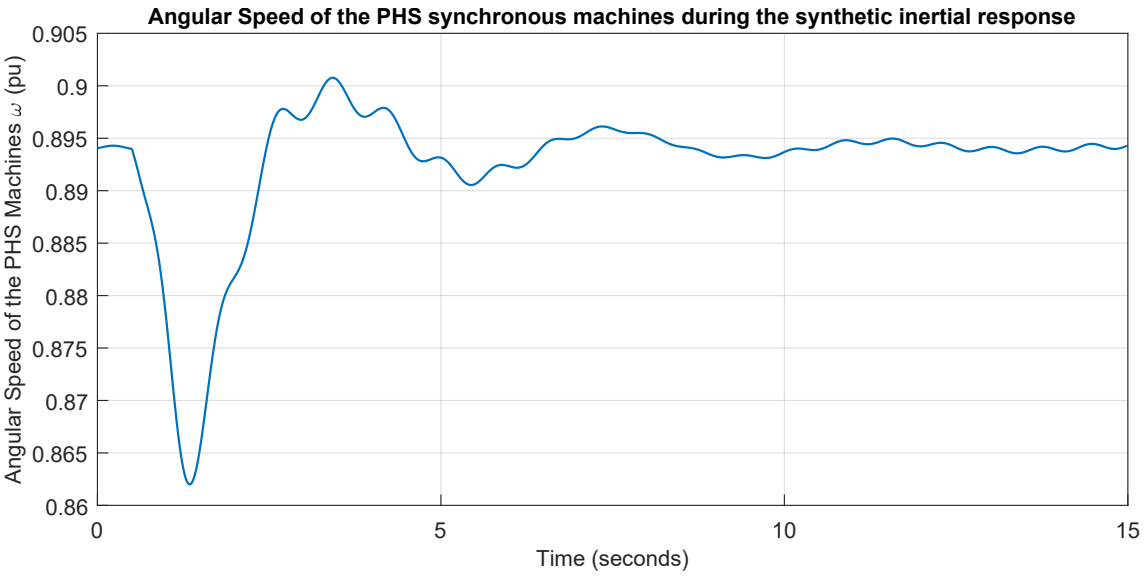

Figure 7.16: Angular speed of the VS-PHS synchronous machines during the contingency and subsequent synthetic inertial response.

Consequently, the flow of water passing through the water conduit follows a similar, but more damped behavior, due to the inertial response of the water, related to the water starting time. The behavior is shown in Figure 7.17.

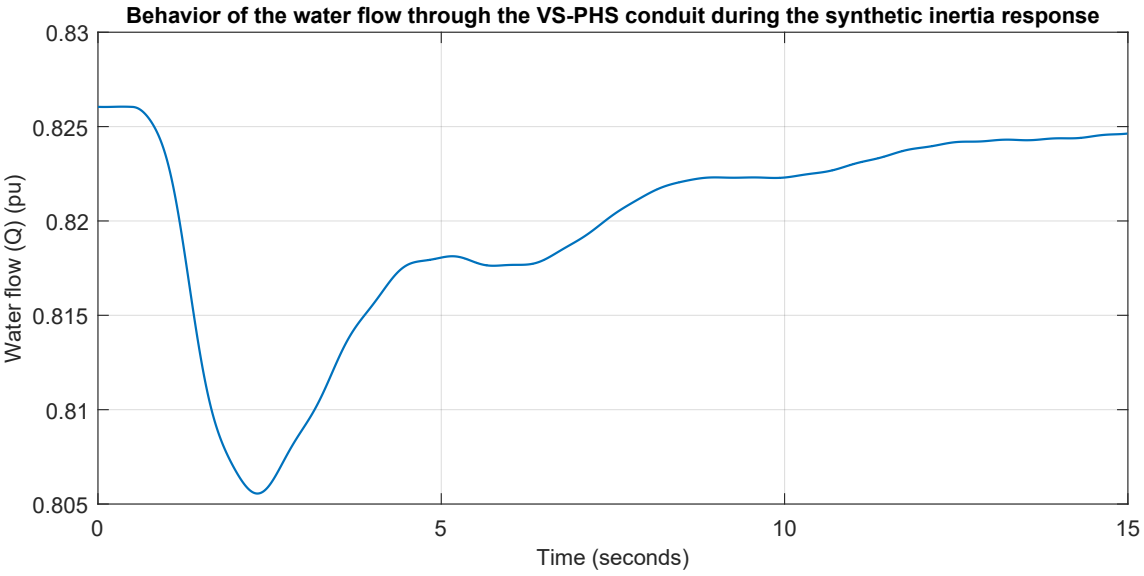

Figure 7.17: Water flow through the water conduit of the VS-PHS during the contingency and subsequent synthetic inertial response.

It is interesting to observe the flow of energy through the VS-PHS components throughout the simulation. The unit contains components capable of energy storage themselves, such as the machine and the converter, with their respective inertia constants and observing the mismatches between output and input power on certain portions of the PHS unit gives some information on the origin of the dynamics observed in, for example, Figure 7.13.

Figure 7.18 shows the comparison between the power being used in the pumping of water in a single unit, the active output power flow of each machine-side converter and the active power input of each grid-side converter.

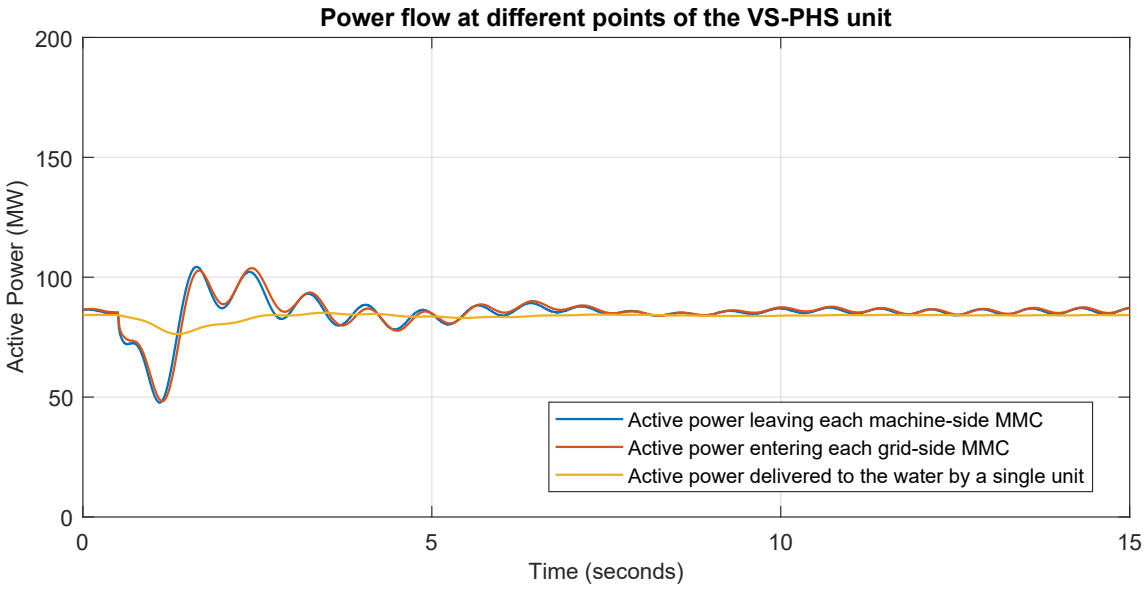

Figure 7.18: Comparison between power flow at different points of the VS-PHS.

It is expected that transient mismatches between these powers, disregarding the losses of course, leads to some energy accumulation in the converter submodules or in the synchronous machine's rotor. Figure 7.19 shows, specifically, the relationship between machine's speed and the power mismatches related to it.

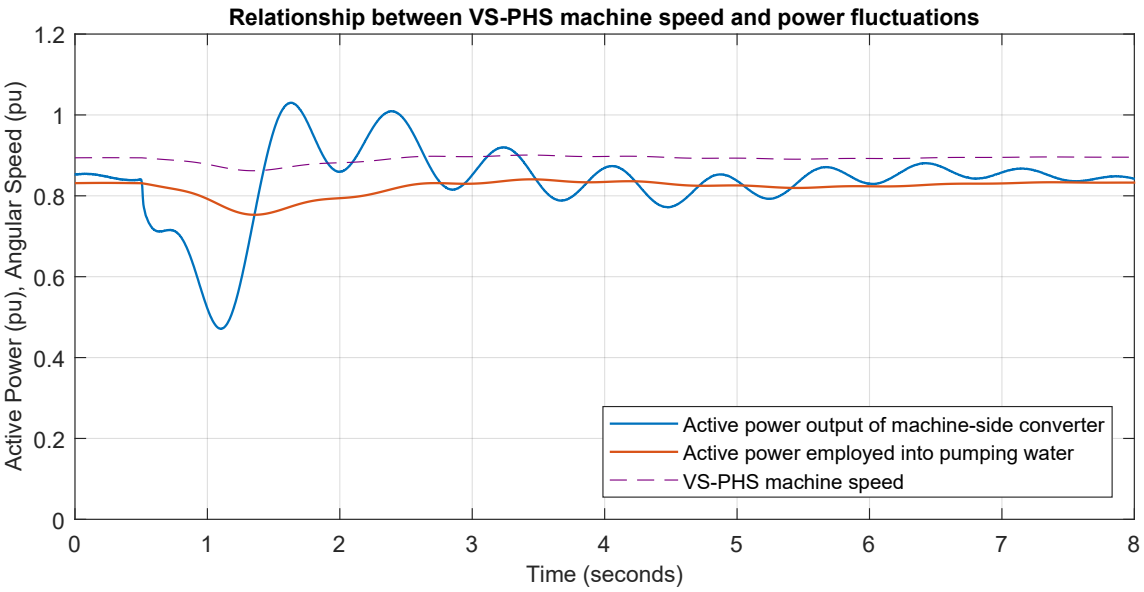

Figure 7.19: Comparison between power flow at different points of the VS-PHS and their comparison with the synchronous machine speed dynamics.

The power related to the water being pumped varies relatively slowly, as any water flow variation is related to the water starting time of the water conduit. Analyzing the figure it can be concluded that, in the immediate aftermath of the contingency, there is a sharp decrease in the power being delivered by the converter to the synchronous machine, and yet, the mechanical torque on its shaft, related to the power being stored in the form of water flow does not decrease as quickly, leading to a reduction of synchronous machine speed. This trend is eventually reversed and there is an active power overshoot being delivered to the machine, this surplus causes the machine's speed to also undergo an overshoot, as has been shown previously in Figure 7.16. Eventually the machine's speed reaches steady state again, after some seconds of oscillatory behavior.

Figure 7.20 shows the comparison between active power flow entering the grid-side converter and leaving the machine-side converter. As expected, the dynamics observed for the submodules dc-voltages are also related to a transient power mismatch. In this case, the power responses of the machine-side and of the grid-side converters present slight differences, These brief energy surplus, or deficit, periods end up causing the observed dc-voltage dynamics on the submodules. For example. Figure 7.20 shows that, after the power dip of the VS-PHS (around the 1.0 s mark), the machine-side MMC starts to give more power to the synchronous machine (in an attempt to recover from the synthetic inertial response) than the grid-side MMC is obtaining from the grid. Therefore, from the mark of 1.5 s up until, approximately, the 2.5 s mark, it is possible to observe a dip on the submodules voltage. This undervoltage trend is only reversed when the power dynamics is reversed due to the

grid-side converter's dc-voltage control and the submodules start to be charged up again.

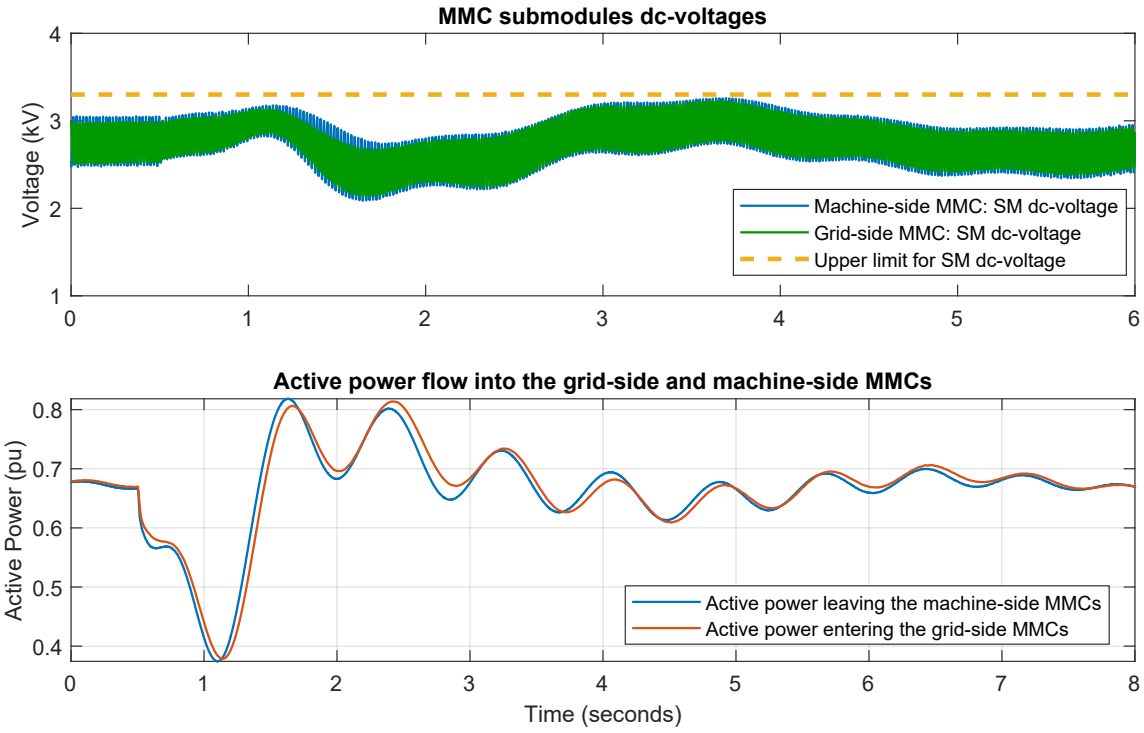

Figure 7.20: Comparison between power flow in different points of the VS-PHS and their relationship to the dc-link voltage of the MMCs submodules.

A possible future work regarding the discussion on synthetic inertia provision lies in the optimization of the coordinated control between converters in order to allow for an optimized synthetic inertia response for a given main-circuit design. For example, the application of an active power flow feed-forward term between machine-side and grid-side converters could yield improved results. It might also be possible to discuss optimized designs for the machine and water-starting time of the water-conduit.

For now, the results have shown that the synthetic inertia concept can be implemented on the pumping mode of the VS-PHS operation. This investigation based on simulations has shown no incompatibility between this control technique and the ratings of the VS-PHS components.

Chapter 8

Conclusion and Future Works

In this dissertation, a detailed time-domain simulation model of a VS-PHS based on the Modular Multilevel Converter has been built. The control design of the plant has been presented. Furthermore, the MMC main circuit and control design have been developed and reported in detail. This development has allowed the author to perform simulations and arrive at the following main conclusions:

In terms of the feasibility of retro-fitting existing units: the maximum possible active power order variations for this PHS have been simulated and, even in this extreme scenario, the required ceiling voltage levels for the excitation systems of synchronous machines stood within the 2 kV range. The synthetic inertia simulation has shown even smaller voltage ceiling requirements, within the range of hundreds of Volts. This leads the author to believe that. in some cases, it would be possible to maintain the same excitation system of existing plants, but more detailed studies regarding the dynamics of the unit in other systems are necessary. It has also been shown that it is possible to control a synchronous machine which has parameters similar to the ones usually found in existing hydro plants. As a future work, it will be important to verify the feasibility of sensorless vector control, which could be important to operate existing machines without rotor position sensors.

In terms of the main-circuit design: the findings, so far, lead the author to believe that the application of a single MMC with IGCTs for power levels of 100 MVA and above is unlikely. Possibly the paralleling of semiconductor switches, or entire converters [99], would be necessary. To the best of the author's knowledge, this would require the application of IGBTs or, alternatively, some sort of parallel association of submodules or arms, as discussed in Reference [125].

In terms of low-frequency operation: this dissertation has proposed a novel choice of waveform to be applied as common-mode voltage during the MMC low-

frequency operation and shown that the common-voltage injection based technique for low-frequency operation of MMC works as intended with this choice of waveform. For a better understanding of the advantages brought by this waveform, which contains a smaller amount of higher order harmonic frequencies, the author believes that alternative simulation models capable of estimating common-mode voltage impacts on the machine and converter are important and are left as a future work suggestion. It has also been shown that, with the application of special control techniques during low-frequency operation, an MMC with regular levels of internal energy storage can be employed in a VS-PHS, without violation of the maximum SM capacitor voltage ripple. Finally, the low-frequency operation strategy, with both the proposed waveform and the trapezoidal waveform, does not interfere with torque control and with the performance of the MTPA technique.

In terms of synthetic inertia during pumping mode: simulations have shown that it is possible to employ synthetic inertia strategies for a VS-PHS operating on pumping mode. The VS-PHS internal variables remained within their nominal values and, subsequently, resumed their previous operating point. The implemented control, therefore, works as intended. In terms of future works and possible power grid applications, the author believes that a complete set of cases for a specific network should be analyzed to guarantee the compatibility of the desired dynamical response with the employed converter and excitation systems. There are also multiple possibilities in terms of control design techniques taking into account main-circuit limitations and PLL dynamics.

Bibliography

[1] BEZERRA, B., BARROSO, L. A., BRITO, M., et al. "Measuring the hydroelectric regularization capacity of the Brazilian hydrothermal system". In: *IEEE PES General Meeting*, pp. 1–7. IEEE, 2010.

[2] *HYPERBOLE - Hydropower Stations Performance and Flexible Operation Towards Lean Integration of New Renewable Energies*. Final Report FP7-Energy, Grant agreement ID: 608532, Ecole Polytechnique Federale de Lausanne, Lausanne, Switzerland, 2017.

[3] AEMO OPERATIONAL ANALYSIS AND ENGINEERING. *Inertia Requirements Methodology - Inertia Requirements and Shortfalls*. In: Technical report, Australian Energy Market Operator (AEMO), 2018.

[4] MILLER, N., SHAO, M., VENKATARAMAN, S. *California ISO Frequency Response Study*. In: Technical report, GE Energy, 2011.

[5] GERMÁN CLAUDIO TARNOWSKI. *Coordinated frequency control of wind turbines in power systems with high wind power penetration*. Ph.d thesiss, Techincal University of Denmark, 2011.

[6] ØRUM, E., KUIVANIEMI, M., HAARLA, L., et al. "A Survey on Inertia Related Challenges and Mitigation Measures", .

[7] KROPOSKI, B., JOHNSON, B., ZHANG, Y., et al. "Achieving a 100% Renewable Grid", *IEEE Power and Energy Magazine*, v. 56, n. 65, pp. 61–73, 2017.

[8] HYDRO QUÉBEC TRANSENERGIE. "Transmission provider technical requirements for the connection of power plants to the Hydro-Québec Transmission System". Available at: <`http://www.hydroquebec.com/transenergie/fr/commerce/pdf/exigence_raccordement_fev_09_en.pdf`>.

[9] BEIRES, P. P., MOREIRA, C., LOPES, J. P., et al. "The Need of Synchronous Inertia in Autonomous Power Systems with Increasing Shares of Renewables", *Natural gas*, v. 54, pp. 14–6.

[10] URDAL, H., IERNA, R., ROSCOE, A. J. "Stability challenges & solutions for power systems operating close to 100% penetration of power electronic interfaced power sources: exchange of experience between hybrid and major power systems". In: *3rd International Hybrid Power Systems Workshop*, 2018.

[11] URDAL, H., IERNA, R., ZHU, J., et al. "System strength considerations in a converter dominated power system", *IET Renewable Power Generation*, v. 9, n. 1, pp. 10–17, 2014.

[12] ØRUM, E., KUIVANIEMI, M., LAASONEN, M., et al. *Future system inertia*. In: Technical report, European Network of Transmission System Operators for Electricity (ENTSO-E), 2015.

[13] ØRUM, E., HAARLA, L., KUIVANIEMI, M., et al. *Future system inertia 2*. In: Technical report, European Network of Transmission System Operators for Electricity (ENTSO-E), 2016.

[14] EIRGRID, SONI. *A proposal for Rate of Change of Frequency Remuneration Mechanism Consultation 2015*. In: Technical report, EIRGrid and SONI, 2015.

[15] HESSE, H. C., SCHIMPE, M., KUCEVIC, D., et al. "Lithium-ion battery storage for the grid—a review of stationary battery storage system design tailored for applications in modern power grids", *Energies*, v. 10, n. 12, pp. 2107, 2017.

[16] LUO, X., WANG, J., DOONER, M., et al. "Overview of current development in electrical energy storage technologies and the application potential in power system operation", *Applied energy*, v. 137, pp. 511–536, 2015.

[17] CHEN, H., CONG, T. N., YANG, W., et al. "Progress in electrical energy storage system: A critical review", *Progress in natural science*, v. 19, n. 3, pp. 291–312, 2009.

[18] SUUL, J. A. "Variable speed pumped storage hydropower plants for integration of wind power in isolated power systems". In: *Renewable Energy*, IntechOpen, 2009.

[19] MUNOZ-HERNANDEZ, G. A., MANSOOR, S. P., JONES, D. I. *Modelling and Controlling Hydropower Plants*. London, Springer-Verlag, 2013.

[20] HILDINGER, T., KODDING, L. "Modern design for variable speed motor-generators-asynchronous (DFIM) and synchronous (SMFI) electric machinery options for pumped storage powerplants", *Innsbruck, Hydro*, 2013.

[21] UNITED STATED DEPARTMENT OF ENERGY. "DOE Global Energy Storage Database". Available at: <`https://www.energystorageexchange.org/projects/data_visualization`>.

[22] NOURAI, A., SCHAFER, C. "Changing the Electricity Game", *IEEE Power and Energy Magazine*, v. 7, n. 4, pp. 42–47, 2009.

[23] SIVAKUMAR, N., DAS, D., PADHY, N. P. "Variable speed operation of reversible pump-turbines at Kadamparai pumped storage plant – A case study", *Energy Conversion and Management*, v. 78, n. 1, pp. 96–104, 2013. doi: {https://doi.org/10.1016/j.enconman.2013.10.048}.

[24] VALAVI, M. "Variable-Speed Operation of Hydropower Plants", *IEEE Industry Applications Magazine*, v. 42, n. 2, pp. 18–27, set. 2018.

[25] SÆTRE, A. L. *Variable Speed Pumped Storage Hydropower for Balancing Variable Power Production in Continental Europe: Electric-Hydraulic Interaction*. M.Sc dissertation, Norwegian University of Science and Technology, Trondheim, Norway, 2013.

[26] DEHGHANI-SANIJ, A., THARUMALINGAM, E., DUSSEAULT, M., et al. "Study of energy storage systems and environmental challenges of batteries", *Renewable and Sustainable Energy Reviews*, v. 104, pp. 192–208, 2019.

[27] MATHIS ROGNER AND NICHOLAS TROJA. *The world's water battery: Pumped hydropower storage and the clean energy transition*. In: Working paper, International Hydropower Association, London, United Kingdom, 2018.

[28] KATSAPRAKAKIS, D. A., DAKANALI, I., CONDAXAKIS, C., et al. "Comparing electricity storage technologies for small insular grids", *Applied Energy*, v. 251, pp. 113332, 2019.

[29] JAVED, M. S., ZHONG, D., MA, T., et al. "Hybrid pumped hydro and battery storage for renewable energy based power supply system", *Applied Energy*, v. 257, pp. 114026, 2020.

[30] KORITAROV, V., VESELKA, T., GASPER, J., et al. *Modeling and Analysis of Value of Advanced Pumped Storage Hydropower in the United States*. In: Report ANL/DIS-14/07, Argonne National Laboratory, Argonne, Illinois, USA, 2014.

[31] KELMAN, R., HARRISON, D. L. "Integrating Renewables with Pumped Hydro Storage in Brazil: a Case Study", working paper or preprint, jun. 2019. Available at: <https://hal.archives-ouvertes.fr/hal-02147740>.

[32] INTERNATIONAL HYDROPOWER ASSOCIATION. *2019 Hydropower Status Report*. In: Working paper, International Hydropower Association, London, United Kingdom, 2019.

[33] BAJAY, S., ADELAIDE, M. "Seminário Visitas Técnicas Portugal", Presentation given during the Seminar "Seminário Usinas Hidrelétricas Reversíveis - Experiências Internacionais", available at: http://www.projetouhr.com.br/assets/sem0320/VisitasTenicasPortugal.pdf, 2020.

[34] DESTRO, N., PÅS, M., SAUTERLEUTE, J. F. "Smoothing of offshore wind power variations with Norwegian pumped hydro: case study", 2016.

[35] EMPRESA DE PESQUISA ENERGÉTICA. *Estudo de Inventário de Usinas Reversíveis (UHR) - Metodologia e Resultados Preliminares para o Estado do Rio de Janeiro*. In: Report EPE-DEE-NT-006/2019-R0, Empresa de Pesquisa Energética, Rio de Janeiro, RJ, Brazil, 2019.

[36] BLAKERS, A., STOCKS, M., LU, B., et al. "An atlas of pumped hydro energy storage", *Australian National University, Australia*, 2017.

[37] HYDROFLEX. "HydroFlex (Increasing the value of Hydropower through increased Flexibility)". Available at: <https://www.h2020hydroflex.eu/about/>.

[38] GESEL-UFRJ. "Viabilidade das Usinas Reversíveis no Sistema Interligado Nacional". Available at: <http://www.projetouhr.com.br/apresentacao.php>.

[39] INTERNATIONAL HYDROPOWER ASSOCIATION. "Pumped Storage Tracking Tool". Available at: <https://www.hydropower.org/hydropower-pumped-storage-tool>.

[40] HUNT, J. D., BYERS, E., RIAHI, K., et al. "Comparison between seasonal pumped-storage and conventional reservoir dams from the water, energy

and land nexus perspective", *Energy conversion and management*, v. 166, pp. 385–401, 2018.

[41] HUNT, J. D., BYERS, E., WADA, Y., et al. "Global resource potential of seasonal pumped hydropower storage for energy and water storage", *Nature communications*, v. 11, n. 1, pp. 1–8, 2020.

[42] OBERMEYER, H. K., IAVORNIC, C. M., BAKER, G. Q. "Improved Reversible Pump-Turbine Installation". jun. 20 2019. US Patent App. 16/322,185.

[43] PICKARD, W. F. "The history, present state, and future prospects of underground pumped hydro for massive energy storage", *Proceedings of the IEEE*, v. 100, n. 2, pp. 473–483, 2011.

[44] STEIMER, P. K., AUBERT, S., LINDER, S. "Converter-Fed Synchronous Machine for Pumped Hydro Storage Plants", *IEEE Transactions on Energy Conversion*, v. 21, n. 1, pp. 4561–4567, 2014.

[45] BOTTERUD, A., LEVIN, T., KORITAROV, V. *Pumped Storage Hydropower: Benefits for Grid Reliability and Integration of Variable Renewable Energy*. In: Report ANL/DIS-14/10, Argonne National Laboratory, Argonne, Illinois, USA, 2014.

[46] VARGAS-SERRANO, A., HAMANN, A., HEDTKE, S., et al. "Economic benefit analysis of retrofitting a fixed-speed pumped storage hydropower plant with an adjustable-speed machine". In: *2017 IEEE Manchester PowerTech*, pp. 1–6. IEEE, 2017.

[47] ZHANG, Y., ZHUANG, W., SUN, M., et al. "A study on monitoring technology for multi-terminal±500kV VSC-HVDC power transmission system". In: *2017 IEEE 2nd Advanced Information Technology, Electronic and Automation Control Conference (IAEAC)*, pp. 1980–1984. IEEE, 2017.

[48] LI, Y., LIU, H., FAN, X., et al. "Engineering practices for the integration of large-scale renewable energy VSC-HVDC systems", *Global Energy Interconnection*, v. 3, n. 2, pp. 149–157, 2020.

[49] AUBER, S. "Power on tap from variable speed pumped water storage scheme", *Energize*, 2012.

[50] HOLZER, T., MUETZE, A. "Full-size converter operation of hydro power generators: a state-of-the-art review of motivations, solutions, and design

implications", *e & i Elektrotechnik und Informationstechnik*, v. 136, n. 2, pp. 209–215, 2019.

[51] NICOLET, C., BRAUN, O., RUCHONNET, N., et al. "Full Size Frequency Converter for Fast Francis Pump-Turbine Operating Mode Transition". In: *Proceedings of the 2016 HYDROVISION International 2016*, Minneapolis, MN, USA, 2016.

[52] TELLER, O. "Pumped Hydro Storage Plants". In: *Seminário Técnico sobre Usinas Hidrelétricas Reversíveis no Setor Elétrico Brasileiro*, Brasilia, 2014.

[53] SCHLUNEGGER, H., THÖNI, A. "100 MW full-size converter in the Grimsel 2 pumped-storage plant", *Proceedings of the 2013 HYDRO Conference*, 2013.

[54] BASIĆ, M., SILVA, P. C., DUJIĆ, D. "High Power Electronics Innovation Perspectives for Pumped Storage Power Plants". In: *Proceedings of the Hydro 2018*, pp. 237–253, Gdansk, 2018.

[55] HOLZER, T., MUETZE, A., TRAXLER-SAMEK, G., et al. "Generator Design Possibilities for Full-Size Converter Operation of Large Pumped Storage Power Plants", *IEEE Transactions on Industry Applications*, 2020.

[56] PÉREZ-DÍAZ, J., CAVAZZINI, G., BLÁZQUEZ, F., et al. *Technological developments for pumped-hydro energy storage.* In: Technical report, Mechanical Storage Subprogramme, Joint Programme on Energy Storage, European Energy Research Alliance, 2014.

[57] SHARIFABADI, K., HARNEFORS, L., NEE, H., et al. *Design, Control, and Application of Modular Multilevel Converters for HVDC Transmission Systems.* Chichester, John Wiley and Sons, 2016.

[58] ADAM, G. P., AHMED, K. H., FINNEY, S. J., et al. "Modular multilevel converter for medium-voltage applications". In: *2011 IEEE International Electric Machines Drives Conference (IEMDC)*, pp. 1013–1018, 2011.

[59] SCHLUNEGGER, H. "Pumping efficiency: A 100 MW converter for the Grimsel 2 pumped storage plant", *ABB Review*, , n. 2, pp. 42–47, 2014.

[60] DEBNATH, S., QIN, J., BAHRANI, B., et al. "Operation, control, and applications of the modular multilevel converter: A review", *IEEE transactions on power electronics*, v. 30, n. 1, pp. 37–53, 2014.

[61] KOLB, J., KAMMERER, F., GOMMERINGER, M., et al. "Cascaded control system of the modular multilevel converter for feeding variable-speed drives", *IEEE Transactions on Power Electronics*, v. 30, n. 1, pp. 349–357, 2014.

[62] LIANG, J., HARLEY, R. "Pumped Storage Hydro-Plant Models for System Transient and Long-Term Dynamic Studies", *IEEE PES General Meeting*, 2010.

[63] GNANARATHNA, U., GOLE, A. M., JAYASINGHE, R. P. "Efficient Modeling of Modular Multilevel HVDC Converters (MMC) on Electromagnetic Transient Simulation Programs", *IEEE Transactions on Power Electronics*, v. 26, n. 1, pp. 316–324, 2010.

[64] BORKOWSKI, D. "Analytical model of small hydropower plant working at variable speed", *IEEE Transactions on Energy Conversion*, v. 33, n. 4, pp. 1886–1894, 2018.

[65] GALLEFOSS, M. *Synthetic Inertia from a Converter-Fed Synchronous Machine in a Hydro-Electric Power Plant-Modeling, Control and Analysis*. Tese de Mestrado, NTNU, 2018.

[66] MAGAUER, P. "Overview on Pump Turbine Technology". In: *Seminário Técnico sobre Usinas Hidrelétricas Reversíveis no Setor Elétrico Brasileiro*, Brasilia, Brazil, 2014.

[67] SOARES, M., WATANABE, E. H. "MMC Applied to Pumped Hydro Storage using a Differentiable Approximation of a Square Wave as Common-Mode Voltage during Low-Frequency Operation". In: *2020 IEEE 21st Workshop on Control and Modeling for Power Electronics (COMPEL)*, pp. 1–8. IEEE, 2020.

[68] ANTAL, B. A. *Pumped Storage Hydropower: A Review*. M.Sc dissertation, University of Colorado Denver, Denver, 2014.

[69] SCHREIBER, G. P. *Usinas Hidrelétricas*. Rio de Janeiro, Edghard Blucher, 1977.

[70] TITZSCHKAU, M., HASMATUCHI, V., DECAIX, J., et al. "On-board measurements at a 100MW high-head Francis turbine", *Proceedings of the HydroVienna*, 2018.

[71] HASMATUCHI, V., DECAIX, J., TITZSCHKAU, M., et al. "A challenging puzzle to extend the runner lifetime of a 100 MW Francis turbine", *Proceedings of the Hydro*, 2018.

[72] CIOCAN, G. D., TELLER, O., CZERWINSKI, F. "Variable speed pump-turbines technology", *University Politehnica of Bucharest Scientific Bulletin, Series D: Mechanical Engineering*, v. 74, n. 1, pp. 33–42, 2012.

[73] SUNDFØR, E. H. *Design and operation of a Francis Turbine with Variable Speed Capabilities*. M.Sc dissertation, Norwegian University of Science and Technology, Trondheim, Norway, 2017.

[74] KUWABARA, T., SHIBUYA, A., FURUTA, H. "Design and Dynamic Response Characteristics of 400 MW Adjustable Speed Pumped Storage Unit for Ohkawachi Power Station", *IEEE Transactions on Energy Conversion*, v. 11, n. 2, pp. 376–384, 1996.

[75] ZULCY DE SOUZA, AFONSO H. M. SANTOS, EDSON DA C. BORTONI. *Centrais Hidrelétricas: Estudos para Implantação*. Rio de Janeiro, Centrais Elétricas Brasileiras S.A - ELETROBRÁS, 1999.

[76] KUNDUR, P. *Power System Stabiltiy and Control*. McGraw-Hill, 1994.

[77] KORITAROV, V., GUZOWSKI, L., FELTES, J., et al. *Modeling Adjustable Speed Pumped Storage Hydro Units Employing Doubly-Fed Induction Machines*. In: Report ANL/DIS-13/06, Argonne National Laboratory, Argonne, Illinois, USA, 2013.

[78] WU, B., LANG, Y., ZARGARI, N., et al. *Power Conversion and Control of Wind Energy Systems*. Hoboken, John Wiley and Sons, 2011.

[79] LUBOSNY, Z. *Wind Turbine Operation in Electric Power Systems*. Berlin, Springer-Verlag, 2003.

[80] NOVOTNY, D. W., LIPO, T. A. *Vector Control and Dynamics of AC Drives*. Oxford University Press, 1996.

[81] IEEE POWER ENGINEERING SOCIETY. "IEEE Guide for Synchronous Generator Modeling Practices and Applications in Power System Stability Analyses", 2003.

[82] KRAUSE, P. C., WASYNCZUK, O., SUDHOFF, S. D. *Analysis of Electric Machinery and Drive Systems*. John Wiley and Sons, 2002.

[83] PYRHÖNEN, J., HRABOVCOVA, V., SEMKEN, R. S. *Electrical Machine Drives Control: An Introduction*. Chichester, John Wiley and Sons, 2016.

[84] MANITOBA HYDRO INTERNATIONAL LTD. "More on the Mechanical Equations: Rotating Inertia (J) and the Inertia Constant (H)". Available at: <https://www.pscad.com/webhelp/Master_Library_Models/Machines/Wound_Rotor_Induction_Machine/More_on_the_Mechanical_Equations.htm>.

[85] VAS, P. *Sensorless Vector and Direct Torque Control*. Oxford University Press, 1998.

[86] YAZDANI, A., IRAVANI, R. *Voltage-Sourced Converters in Power Systems: Modeling, Control and Applications*. New Jersey, John Wiley and Sons, 2010.

[87] JOHANSSON, E. *Detailed description of synchronous machine models used in simpow*. M.Sc dissertation, Royal Institute of Technology, KTH, "Västeras, Sweden", 2002.

[88] MELLO, F. P. D. *Dinâmica das Máquinas Elétricas I, Volume 4*. Eletrobrás/UFSM, 1979.

[89] ANDERSON, P. M., FOUAD, A. A. *Power system control and stability*. John Wiley & Sons, 2008.

[90] KAUKONEN, J. *Salient pole synchronous machine modelling in an industrial direct torque controlled drive application*. Tese de Doutorado, Doctoral dissertation. Lappeenranta University of Technology, 1999.

[91] VOSTROV, K. *Synchoronous Machine Vector Control System Development and Implementation*. M.Sc dissertation, Lappeenranta University of Technology, Laappeenranta, 2016.

[92] SCHWESIG, G., BLASCHKE, F. "Device for the field-oriented operation of a converter-fed asynchronous machine". may 1984. US Patent 4,447,787.

[93] MARQUARDT, R. "Modular Multilevel Converters: State of the Art and Future Progress", *IEEE Power Electronics Magazine*, v. 5, n. 4, pp. 24–31, Dec 2018. ISSN: 2329-9215. doi: 10.1109/MPEL.2018.2873496.

[94] WORKING GROUP B4.67. *AC side harmonics and appropriate harmonic limits for VSC HVDC*. In: Brochure 754, CIGRE, 2019.

[95] DARUS, R., KONSTANTINOU, G., POU, J., et al. "Comparison of phase-shifted and level-shifted PWM in the modular multilevel converter". In: *2014 International Power Electronics Conference (IPEC-Hiroshima 2014-ECCE ASIA)*, pp. 3764–3770. IEEE, 2014.

[96] CHRISTE, A., DUJIC, D. "Modular multilevel converter control methods performance benchmark for medium voltage applications", *IEEE Transactions on Power Electronics*, v. 34, n. 5, pp. 4967–4980, 2018.

[97] LI, B., YANG, R., XU, D., et al. "Analysis of the phase-shifted carrier modulation for modular multilevel converters", *IEEE Transactions on Power Electronics*, v. 30, n. 1, pp. 297–310, 2014.

[98] SONG, Q., LIU, W., LI, X., et al. "A steady-state analysis method for a modular multilevel converter", *IEEE Transactions on Power electronics*, v. 28, n. 8, pp. 3702–3713, 2012.

[99] PARK, J., KIM, J., LEE, D., et al. "Development and Design of +-100 Mvar MMC STATCOM at NP Kunta substation in India". In: *2018 CIGRE Bienal - Sessions and Proceedings*, Paris, France.

[100] WORKING GROUP C6.31. *Medium voltage directcurrent (MVDC) gridfeasibility study.* In: Brochure 793, CIGRE, 2020.

[101] HAGIWARA, M., NISHIMURA, K., AKAGI, H. "A medium-voltage motor drive with a modular multilevel PWM inverter", *IEEE Transactions on Power Electronics*, v. 25, n. 7, pp. 1786–1799, 2010.

[102] KORN, A. J., WINKELNKEMPER, M., STEIMER, P. "Low output frequency operation of the modular multi-level converter". In: *2010 IEEE energy conversion congress and exposition*, pp. 3993–3997. IEEE, 2010.

[103] JUNG, J.-J., LEE, H.-J., SUL, S.-K. "Control strategy for improved dynamic performance of variable-speed drives with modular multilevel converter", *IEEE Journal of Emerging and Selected Topics in Power Electronics*, v. 3, n. 2, pp. 371–380, 2014.

[104] JUNG, J.-J., LEE, H.-J., SUL, S.-K. "Control of the modular multilevel converter for variable-speed drives". In: *2012 IEEE International Conference on Power Electronics, Drives and Energy Systems (PEDES)*, pp. 1–6. IEEE, 2012.

[105] LI, B., ZHOU, S., XU, D., et al. "Comparative study of the sinusoidal-wave and square-wave circulating current injection methods for low-frequency

operation of the modular multilevel converters". In: *2015 IEEE Energy Conversion Congress and Exposition (ECCE)*, pp. 4700–4705. IEEE, 2015.

[106] OGASAWARA, S., AKAGI, H. "Modeling and damping of high-frequency leakage currents in PWM inverter-fed AC motor drive systems", *IEEE Transactions on Industry Applications*, v. 32, n. 5, pp. 1105–1114, 1996.

[107] ASEFI, M., NAZARZADEH, J. "Survey on high-frequency models of PWM electric drives for shaft voltage and bearing current analysis", *IET Electrical Systems in Transportation*, v. 7, n. 3, pp. 179–189, 2017.

[108] MÜTZE, A., BINDER, A. "Don't lose your bearings", *ieee industry applications magazine*, v. 12, n. 4, pp. 22–31, 2006.

[109] MUETZE, A., BINDER, A. "Calculation of circulating bearing currents in machines of inverter-based drive systems", *IEEE Transactions on Industrial Electronics*, v. 54, n. 2, pp. 932–938, 2007.

[110] MÜETZE, A. *Bearing Currents in Inverter-Fed AC-Motors*. Ph.d thesis, Technical University of Darmstadt, Darmstadt, Germany, 2004.

[111] WANG, L., BOSWORTH, M., HAUER, J., et al. "Common-mode characterization of a modular multilevel converter in a megawatt-scale medium-voltage dc test bed". In: *2019 IEEE Electric Ship Technologies Symposium (ESTS)*, pp. 388–395. IEEE, 2019.

[112] HOLZER, T., MUETZE, A. "A comparative survey of power converter topologies for full-size converter operation of medium-voltage hydropower generators", *e & i Elektrotechnik und Informationstechnik*, v. 136, n. 6, pp. 263–270, 2019.

[113] BRUHA, M., PIETILÄINEN, K., RAUBER, A. "High Speed Electrical Drives–Perspective of VFD Manufacturer". In: *E3S Web of Conferences*, v. 178, p. 01006. EDP Sciences, 2020.

[114] DENG, Y., WANG, Y., TEO, K. H., et al. "Optimized control of the modular multilevel converter based on space vector modulation", *IEEE Transactions on Power Electronics*, v. 33, n. 7, pp. 5697–5711, 2017.

[115] SEO, I.-K., BELAYNEHN, N. B., PARK, C.-H., et al. "A Study of Common Mode Voltage Generation According to Modulation Methods and Reduction Strategies on MMC System". In: *2018 IEEE Energy Conversion Congress and Exposition (ECCE)*, pp. 3988–3995. IEEE, 2018.

[116] WANG, L., SHI, Y., BOSWORTH, M., et al. "Modular Multilevel Converter Switching Frequency Harmonics Analysis and Suppression Through Cell Voltage Control", *IEEE Open Journal of Power Electronics*, v. 1, pp. 149–160, 2020.

[117] WANG, J., LI, H., YANG, Z., et al. "Common-Mode Voltage Reduction of Modular Multilevel Converter Based on Chaotic Carrier Phase Shifted Sinusoidal Pulse Width Modulation". In: *2020 IEEE International Symposium on Electromagnetic Compatibility & Signal/Power Integrity (EMCSI)*, pp. 626–631. IEEE, 2020.

[118] LI, B., ZHOU, S., XU, D., et al. "A hybrid modular multilevel converter for medium-voltage variable-speed motor drives", *IEEE Transactions on Power Electronics*, v. 32, n. 6, pp. 4619–4630, 2016.

[119] DU, S., WU, B., ZARGARI, N. R., et al. "A flying-capacitor modular multilevel converter for medium-voltage motor drive", *IEEE Transactions on Power Electronics*, v. 32, n. 3, pp. 2081–2089, 2016.

[120] HUANG, X., WANG, Z., KONG, Z., et al. "Modular multilevel converter with three-port power channels for medium-voltage drives", *IEEE Journal of Emerging and Selected Topics in Power Electronics*, v. 6, n. 3, pp. 1495–1507, 2017.

[121] FERNÁNDEZ-GUASTI, M. "Squdel Function: Square Wave Approximation Without Ringing", *Circuits, Systems, and Signal Processing*, v. 38, n. 2, pp. 764–773, 2019.

[122] ASEA BROWN BOVERI (ABB). *Medium Voltage Power Converter Systems Portfolio PCS 6000 / 8000.* Relatório técnico, ABB, 2010.

[123] WITT, A., CHALISE, D. R., HADJERIOUA, B., et al. "Development and implications of a predictive cost methodology for modular pumped storage hydropower (m-PSH) projects in the United States", *ORNL/TM-2016/590, Oak Ridge National Laboratory, Oak Ridge, Tennessee*, 2016.

[124] ALMEIDA, L., LIRIO, F., GOMES, S., et al. "Sistema Benchmark no PSCAD e ATP contendo Elo de Corrente Contínua e Máquinas". In: *Proceedings of the XIII Symposium of Specialists in Electric Operational and Expansion Planning*, Foz do Iguaçu, PR, Brasil.

[125] MILOVANOVIC, S., DUJIC, D. "On Power Scalability of Modular Multilevel Converters: Increasing Current Ratings Through Branch Paralleling", *IEEE Power Electronics Magazine*, v. 7, n. 2, pp. 53–63, 2020.

[126] ZEND, R., ZHAO, B., WEI, T., et al. "Integrated Gate Commutated Thyristor-Based Modular Multilevel Converters: A Promising Solution for High-Voltage dc Applications", *IEEE Industrial Electronics Magazine*, 2019.

[127] DU, S., DEKKA, A., WU, B., et al. *Modular Multilevel Converters: Analysis, Control and Applications*. New Jersey, John Wiley and Sons, 2018.

[128] MODEER, T., NEE, H.-P., NORRGA, S. "Loss Comparison of Different Sub-Module Implementationsfor Modular Multilevel Converters in HVDC Applications", 2011.

[129] HIDALGO, S. A. *Characterisation of 3.3kV IGCTs for Medium Power Applications*. Ph.d thesis, Toulouse INP, Toulouse, France, 2005.

[130] VEMULAPATI, U., RAHIMO, M., ARNOLD, M., et al. "Recent Advancements in IGCT Technologies for High Power Electronics Applications", *Proceedings of the 2015 17th European Conference on Power Electronics and Applications (EPE'15 ECCE-Europe)*, 2015.

[131] WIKSTRÖM, T. "Introducing the 5.5kV, 5kA HPT IGCT", *Proceedings of the 2012 PCIM Europe)*, 2012.

[132] ASEA BROWN BOVERI (ABB). *Asymmetric Integrated Gate-Commutated Thyristor 5SHY 55L4500*. In: Application Note 5SYA1243-06, institution =, .

[133] ASEA BROWN BOVERI (ABB). "Insulated gate bipolar transistor (IGBT) and diode modules with SPT and SPT+ chips". . Available at: <`https://new.abb.com/semiconductors/igbt-and-diode-modules`>.

[134] DORN, J., BEUERMANN, M., ERMISCH, R., et al. "Parallel connection of IGBT devices in VSC for HVDC", *CIGRE SC B4 International Colloquium*, 2019.

[135] ASEA BROWN BOVERI (). *Applying IGCTs*. In: Report 5SYA 2032-04, ABB Switzerland Ltd Semiconductors, Lenzburg, Switzerland, 2016.

[136] ZYGMANOWSKI, M., GRZESIK, B., NALEPA, R. "Capacitance and Inductance Selection of the Modular Multilevel Converter", *Proceedings of the 2013 15th European Conference on Power Electronics and Applications (EPE)*, v. 21, n. 1, pp. 4561–4567, 2014.

[137] ASEA BROWN BOVERI (ABB). "Integrated gate-commutated thyristors (IGCT)". . Available at: <https://new.abb.com/semiconductors/integrated-gate-commutated-thyristors-(igct)>.

[138] MERLIN, M. M. C., GREEN, T. C. "Cell capacitor sizing in multilevel converters: cases of the modular multilevel converter and alternate arm converter", *IET Power Electronics*, v. 8, n. 3, pp. 350–360, 2015.

[139] CHINCHILLA, M., ARNALTES, S., BURGOS, J. C. "Control of Permanent-Magnet Generators Applied to Variable-Speed Wind-Energy Systems Connected to the Grid", *IEEE Transactions on Energy Conversion*, v. 21, n. 1, pp. 130–135, 2006.

[140] TRICARICO, T., GONTIJO, G., NEVES, M., et al. "Control Design, Stability Analysis and Experimental Validation of New Application of an Interleaved Converter Operating as a Power Interface in Hybrid Microgrids", *Energies*, v. 12, n. 437, 2019.

[141] GAO, Z. "Scaling and Bandwidth-Parameterization Based Controller Tuning". In: *Proceedings of the 2003 American Control Conference*, Denver, Colorado, USA, 2003.

[142] TU, Q., XU, Z., ZHANG, J. "Circulating current suppressing controller in modular multilevel converter". In: *IECON 2010 - 36th Annual Conference on IEEE Industrial Electronics Society*, pp. 3198–3202, Nov 2010. doi: 10.1109/IECON.2010.5675048.

[143] NØLAND, J. K., NUZZO, S., TESSAROLO, A., et al. "Excitation System Technologies for Wound-Field Synchronous Machines: Survey of Solutions and Evolving Trends", *IEEE Access*, v. 21, n. 1, pp. 130–135, 2019.

[144] MURDOCH, A., SANDERSON, H., LAWSON, R. "Excitation systems-performance specification to meet interconnection requirements". In: *2000 IEEE Power Engineering Society Winter Meeting. Conference Proceedings (Cat. No. 00CH37077)*, v. 1, pp. 597–602. IEEE, 2000.

[145] FOGARTY, J. "Connections between generator specifications and fundamental design principles". In: *IEMDC 2001. IEEE International Electric Machines and Drives Conference (Cat. No. 01EX485)*, pp. 51–56. IEEE, 2001.

[146] JONAS KRISTIANSEN NØLAND. *Fast-response rotating brushless exciters for improved stability of synchronous generators*. Licenciate thesis, Uppsala University, 2016.

[147] HARNEFORS, L., SAARAKKALA, S. E., HINKKANEN, M. "Speed Control of Electrical Drives Using Classical Control Methods", *IEEE Transactions on Industry Applications*, v. 49, n. 2, pp. 889–898, 2013.

[148] GONZALEZ-LONGATT, F., CHIKUNI, E., RASHAYI, E. "Effects of the synthetic inertia from wind power on the total system inertia after a frequency disturbance". In: *2013 IEEE International Conference on Industrial Technology (ICIT)*, pp. 826–832. IEEE, 2013.

[149] ERIKSSON, R., MODIG, N., ELKINGTON, K. "Synthetic inertia versus fast frequency response: a definition", *IET Renewable Power Generation*, v. 12, n. 5, pp. 507–514, 2017.

[150] HAGIWARA, M., HASEGAWA, I., AKAGI, H. "Start-up and low-speed operation of an electric motor driven by a modular multilevel cascade inverter", *IEEE Transactions on Industry Applications*, v. 49, n. 4, pp. 1556–1565, 2013.

Appendix A

Characteristics of the Network Elements of the 11-bus System

Table A.1: Data regarding the Transmission Lines of the 11-bus system.

Characteristic	**Value**
Nominal Voltage	500 kV
Positive Sequence Resistance per km	0.0227 Ω
Positive Sequence Inductance per km	0.333 Ω
Positive Sequence Shunt Capacitive Reactance per km	0.203 MΩ
Negative Sequence Resistance per km	0.198 Ω
Negative Sequence Inductance per km	0.159 Ω
Negative Sequence Shunt Capacitive Reactance per km	0.401 MΩ

Table A.2: Data regarding the synchronous machines of the 11-bus system.

Circuit Variable	**Nominal Value**
Synchronous Reactance X_d	1.8 pu
Transient Reactance X'_d	0.3 pu
Sub Transient Reactance X''_d	0.25 pu
Synchronous Reactance X_q	1.7 pu
Transient Reactance X'_q	0.550 pu
Sub-Transient Reactance X''_q	0.25 pu
Transient Time T'_{do}	8 s
Sub-Transient Time T''_{do}	0.03 s
Transient Time T'_{qo}	0.4 s
Sub-Transient Time T''_{qo}	0.25 s
Leakage Reactance X_l	0.2 pu
Nominal Voltage (rms)	20 kV
Apparent Power	900 MVA
Inertia Constant (H)	3.75 s

Table A.3: Data regarding the Transformers of the 11-bus system.

Characteristic	**Value**
Nominal Voltage	500/20 kV
Positive Sequence Leakage Reactance	0.1 pu

Table A.4: Load-flow condition of the 11-bus system.

Bus Number	**RMS Voltage (pu)**	**Angle (Degrees)**
1	1.025	11.0
2	1.045	1.0
3	1.049	6.9
4	1.023	-1.4
5	1.04	-1.9
6	1.014	6.4
7	0.998	-4.9
8	0.993	-12.7
9	0.989	-18
10	1.0	-2.9
11	1.0	0.0

Appendix B

Control Settings

B.1 PLL

The PLL implemented is a Synchronous-Reference Frame PLL, with the constants shown in Table B.1

Table B.1: Constants of the PLL's PI controller.

Constant	Value
K_p	2
K_i	70 s^{-1}

B.2 Dc-Voltage Control

Table B.2: Constants of the dc voltage control's PI controller.

Constant	Value
K_p	0.135
K_i	1.13 s^{-1}

B.3 GSC's Output Current Control

Table B.3: Constants of the current control's PI controller.

Constant	Value
K_p	0.2
K_i	0.4 s^{-1}